# Reconfigurable antennas and circuits based on controllable artificial materials

David René-Loxq

COLLEGE MATHS, TELECOMS
DOCTORAL INFORMATIQUE, SIGNAL
BRETAGNE SYSTEMES, ELECTRONIQUE

Université de Rennes

# THÈSE DE DOCTORAT DE

L'UNIVERSITÉ DE RENNES

ÉCOLE DOCTORALE N° 601
*Mathématiques, Télécommunications, Informatique, Signal, Systèmes, Électronique*
Spécialité : *Télécommunication*

Par
**David RENÉ--LOXQ**

## Reconfigurable antennas and circuits based on controllable artificial materials

**Thèse présentée et soutenue à l'Université de Rennes, le 10 Juillet 2023**
**Unité de recherche : Institut d'Electronique et de Technologies du numéRique, UMR CNRS 6164**

### Rapporteurs avant soutenance :

Philippe LE THUC — Professeur, Université Côte d'Azur
Zouheir RIAH — Enseignant Chercheur HDR, ESIGELEC

### Composition du Jury :

| | | |
|---|---|---|
| Président : | Langis ROY | OntarioTech University |
| Examinateurs : | Philippe LE THUC | Professeur, Université Côte d'Azur |
| | Zouheir RIAH | Enseignant Chercheur HDR, ESIGELEC |
| | Nicolas DELHOTE | Maître de Conférences, Université de Limoges |
| | Divitha SEETHARAMDOO | Chargée de Recherche, IFSTTAR, Université Gustave Eiffel |
| Dir. de thèse : | Olivier LAFOND | Professeur, Université de Rennes |
| Co-dir. de thèse : | Mohamed HIMDI | Professeur, Université de Rennes |

# Remerciements

Je tiens à exprimer ma profonde gratitude envers toutes les personnes qui ont contribué de près ou de loin à la réalisation de ce travail de thèse. Ces 3 années de thèses qui m'ont mené jusqu'à ma soutenance ont été enrichissantes, stimulantes, parfois ardues, et je n'aurais pas pu les mener à bien sans le soutien de nombreuses personnes.

Je tiens tout d'abord à remercier grandement mes directeurs de thèse Olivier Lafond et Mohamed Himdi, pour leurs conseils, leurs expertises et leurs encouragements tout au long de ces années.

Je voudrais aussi remercier les membres de mon jury de thèse, Langis Roy, Philippe Le Thuc, Zouheir Riah, Nicolas Delhote et Divitha Seetharmdoo, pour l'intérêt qu'ils ont porté à mes travaux.

Je tiens finalement à remercier ma famille, mes amis et mes collègues pour leurs soutiens et leurs encouragements.

# Table of Contents

# RÉSUMÉ EN FRANÇAIS

Cette thèse s'inscrit dans le cadre d'un projet international ANR/NSERC sur le sujet : "Reconfigurable Wireless Componesnts using Field Programmable Microwave Substrate". Ce projet a débuté en 2019 mais du fait de la crise Covid a été prolongé jusqu'àla fin juin 2023. Ce projet a permis de faire collaborer des laboratoires de recherche français et canadiens ainsi qu'une entreprise canadienne. Du côté Français, les laboratoires concernés sont l'IETR et XLIM et du côté Canadien sont concernés Ontario Tech University, Carlton University et Orbcom (entreprise). Ce projet a été divisé en plusieurs workpackages avec notamment comme objectifs principaux, l'étude, la conception et la fabrication de circuits et antennes reconfigurables basés sur le "Field Programmable Microwave Studio". Le Field Programmable Microwave Substrate (FPMS) est une technologie développée au Canada en 2016 [1] qui permet la programmation de multiples fonctions micro-onde avec donc un très haut degré de reconfigurabilité. Le FPMS est constitué de petites Cellule Unitaire (UC) dont la permittivité relative peut être contrôlée. Cette permittivité peut ainsi, à une fréquence donnée, variée d'une valeur positive à une valeur négative. Ainsi, en associant des cellules à la permittivité positive et des cellules à la permittivité négative, des guides peuvent être créés amis également de nombreuses autres fonctions microondes. Il est également possible théoriquement de changer la valeur positive de la permittivité diélectrique, entre autres pour réaliser des concepts nécessitant des lois d'indice de réfraction inhomogènes. Mon travail de thèse concerne l'amélioration de la technologie FPMS notamment pour effectuer une montée en fréquence du concept de base et de l'utiliser pour diverses applications tels que des circuits et antennes reconfigurables.

Après une introduction générale sur mon travail de thèse, dans le premier chapitre, un état de l'art est réalisé. Celui-ci est centré sur les applications recherchées pour le FPMS. Notamment, dans la première partie, différents circuits reconfigurables seront présentés : filtres, coupleurs, diviseurs, déphaseurs. Les concepts présentés sont le plus souvent reconfigurables via l'utilisation de composants électroniques contrôlables tels que des diodes PIN ou Varactor. Ce qui ressort de cette première partie est que la reconfigurabilté concerne majoritairement une fonction unique. Ainsi, par exemple, un filtre reconfigurable peut voir sa fréquence, sa bande passante, ou son ordre être reconfiguré,

mais il ne pourra pas être reprogrammé pour devenir un coupleur ou un déphaseur. C'est pourquoi la technologie FPMS est intéressante, car celle-ci doit permettre de réaliser des fonctions multiples et de les reprogrammer à volonté, avec un haut degré de reconfigurabilité. Il pourrait même être envisagé d'utiliser un FPMS doté de nombreuses cellules pour obtenir en parallèle des circuits et antennes reconfigurables. Dans la seconde partie du chapitre, des antennes reconfigurables (antennes à balayage de faisceau, multifaisceaux, ...) sont étudiées. Nous donnons et commentons différents systèmes : Matrice de Butler, lentille de Rotman, réseaux phasés ou réflecteurs, antennes à onde fuite, et en particulier les lentilles inhomogènes. En effet, le contrôle des paramètres diélectriques (permittivité) offert par la technologie FPMS peut permettre la réalisation de lentilles inhomogènes reconfigurables de type Luneburg, Maxwell-Fish Eye ou bien encore Mikaelian. Concernant les lentilles inhomogènes, il ressort de cette étude bibliographique, que la grande majorité des systèmes reconfigurables est basée sur des lentilles associées à plusieurs sources élementaires (sources primaires) commutables entre elles ou qui excitent simultanément la lentille. Très peu de concepts sont basés sur une modification électronique de la loi pour assurer la reconfigurabilité, ce que doit permettre l'utilisation de la technologie FPMS.

Le second chapitre concerne la création d'un nouveau FPMS en bande X. La première version du FPMS présenté dans [1] fonctionnait entre 1 et 3 GHz, nous voulions créer une version qui fonctionne entre 10 et 15 GHz. Pour ce faire, dans un premier temps, le comportement général d'une cellule unitaire est étudié, ainsi que la méthode d'extraction des paramètres diélectriques. Afin de créer un FPMS capable de synthétiser des guides d'onde, il faut que les cellules unitaires soient capables à une fréquence donnée, de passer d'une constante diélectrique positive à une constante diélectrique négative. Le composant clef permettant d'arriver à cette reconfigurabilité est une diode varactor. Suivant la tension appliquée, la capacitance interne de la diode varactor va varier. Cette valeur de capacitance affecte directement la fréquence de résonance de la cellule et suivant la fréquence de travail par rapport à cette fréquence de résonance, la cellule produira soit une permittivité positive ou négative. Une étude paramétrique est proposée afin de trouver la cellule qui propose le meilleur compromis entre les performances de la cellule lorsqu'elle est dans l'état négatif et lorsqu'elle est dans son état positif. Pour la version finale de la cellule unitaire, la fréquence de résonance de celle-ci peut varier de 10.5 GHz à 22.75 GHz. Avec cette cellule, un FPMS de $16 \times 16$ cellules est créé. Pour obtenir une reconfigurabilité maximale, chaque cellule possède une alimentation indépendante. Pour démontrer que le design proposé est fonctionnel, un certain de nombre de configurations simples sont tes-

tées, ces configurations permettent notamment de réaliser plusieurs fonctions différentes : routage, filtrage, déphaseurs et diviseurs. Afin de simplifier les études futures et notamment le développement de nouvelles fonctions et leurs optimisations, un modèle équivalent de la cellule unitaire du FPMS est aussi présenté dans ce chapitre. Il est important de noter que ce modèle équivalent développé durant ma thèse et présenté dans ce chapitre a été transférer au laboratoire XLIM afin qu'une doctorante l'utilise en lien avec un algorithme d'optimisation pour notamment la conception de filtres reconfigurables utilisant la technologie FPMS. Cette nouvelle cellule en bande X a également permis la conception d'un nouveau FPMS qui a été développé pour être utilisé par tous les partenaires du projets. Ce prototype a été mis en oeuvre par les partenaires et la société Voltakap. Il est important de noter que ce développement a pris beaucoup de temps pour l'implémentation et est à ce jour toujours en cours de fabrication.

Le troisième chapitre aborde de manière simple l'utilisation de la technologie FPMS dans la conception d'une antenne reconfigurable. Nous combinons ici la technologie FPMS avec une antenne à onde de fuite réalisée en utilisant la technologie guide d'ondes intégré au substrat en demi-mode (HMSIW). Les antennes à onde de fuite sont connues pour offrir naturellement un balayage du faisceau principal avec la fréquence. Le premier objectif du design présenté dans ce chapitre est de développer une antenne permettant un balayage électronique du faisceau à une fréquence fixe. Trois prototypes différents sont présentés et réalisés dans ce chapitre. Le premier est une version passive de l'antenne permettant de présenter les performances de celle-ci et notamment sa capacité de dépointage en fonction de la fréquence. L'antenne présentée est basée sur la technologie "HMSIW" qui correspond à un demi-guide d'onde SIW (Substrate Integrated Waveguide). Ce type de structure a pour propriété intéressante de produire un rayonnement lorsqu'elle est utilisée aux alentours de la fréquence de coupure du guide d'onde. Le deuxième prototype est une version modifiée de la première antenne, ici le mur de vias qui constitue un des côté du guide d'onde est remplacé par une ligne de cellules unitaire FPMS. En contrôlant la tension appliquée à la diode varactor de chaque cellule, la direction du faisceau principal peut être contrôlée. En changeant la tension entre 0 V et 13 V la direction du faisceau principal varie dans le plan-H, à 8 GHz, de 18° à 45°. Le gain mesuré quant à lui varie entre 5.95 dBi et 7.55 dBi. Pour le troisième prototype, l'antenne HSMIW FPMS est associée à un cornet, pour modifier l'ouverture et la direction du faisceau principal dans le plan-E. Ce second prototype garde le même comportement dans le plan-H : dépointage électronique à fréquence fixe. Un autre objectif était également d'obtenir un diagramme de rayonnement

fixe (direction angulaire) sur une large plage de fréquences. L'utilisation du FPMS avec les diodes varactor contrôlables permet d'assurer cette fonction ce qui est un résultant innovant démontré dans ce chapitre pour une antenne de type Leaky-Wave.

Dans le dernier chapitre, nous étudions à nouveau le design d'une antenne basée sur la technologie FPMS, mais cette fois nous utilisons son plein potentiel. L'antenne proposée dans cette section est une antenne basée sur une lentille inhomogène. De façon générale, une lentille inhomogène voit l'indice de réfraction varier en fonction de la position dans la lentille. Parmi les lentilles inhomogènes, nous pouvons citer la lentille de Luneburg, celle de Maxwell-Fish Eye ou bien encore la lentille de Mikaelian. Chaque type possède une loi d'indice de réfraction différente. Pour réaliser ces lentilles, plusieurs techniques existent comme l'imbrication de coquilles ou couronnes avec des constantes diélectriques différentes, l'utilisation d'un matériau unique associé à des trous d'air spatialement répartis ou bien encore des métamatériaux. Cependant, avec ces technologies, la loi d'indice de réfraction est fixe et ne peut donc pas être reconfigurée. Dans ce chapitre, l'objectif est la conception de lentilles inhomogènes pour lesquelles la synthèse de la loi de réfraction est effectuée par le contrôle des cellules élémentaires du FPMS. En effet, le FPMS permet de contrôler localement la permittivité et la permeabiltié du materiau. Dans ce chapitre nous étudions particulièrement une lentille de Mikaelian. Ce type de lentille, contrairement à la lentille de Luneburg qui est sphérique, est une lentille cylindrique où l'indice de réfraction dépend de la distance radiale. Pour des facilités de fabrication et d'intégration nous considérons ici une version plate de la lentille. Premièrement, différents prototypes passifs sont proposés et mesurés afin d'étudier les capacités de dépointage de la lentille de Mikealian en fonction de la position de la source. Ici, la technologie FPMS n'est pas utilisée mais les lentilles et leur loi d'indice de réfraction sont fabriquées grâce à l'utilisation d'un processus technologique simple et innovant basé sur une mousse pressée. Cette mousse est un matériau composite alliant un polymère de base dans lequel est injecté des bulles d'air. En expulsant toute ou partie de ces bulles d'air, il devient ainsi possible de contrôler l'indice de réfraction et de concevoir des lentilles inhomogènes. Les différents prototypes permettent un dépointage du faisceau principal de $\pm 35°$ tout en conservant un gain acceptable pour les différentes angles de dépointage. Plusieurs sources élémentaires optimisées associées à ce type de lentille permet ensuite la mise en oeuvre de systèmes rayonnants reconfigurables comme démontré dans ce chapitre avec un bon recouvrement des différentes faisceaux (un par source élémentaire). Dans une seconde partie nous étudions la combinaison de la technologie FPMS et de la lentille de Mikaelian. L'objectif

est ici de proposer un dépointage électronique avec une position de la source fixe ce qui est un concept original et peu étudié jusqu'alors. Dans un premier temps, nous étudions une cellule unitaire capable de produire une variation suffisante de l'indice de réfraction pour synthétiser la loi de réfraction d'une lentille de Mikaelian. La cellule retenue pour cette partie fonctionne entre 25 GHz et 30 GHz. Avec cette cellule une lentille FPMS de $16 \times 16$ cellules unitaires est proposée. Cette lentille électronique est ensuite étudiée afin de démontrer ses capacités de dépointage. L'idée pour obtenir le dépointage voulu est de "déplacer" le centre de la loi de réfraction de la lentille ; plus la loi est excentrée plus le dépointage est important. Les simulations montrent une capacité de dépointage allant jusqu'à $\pm 40°$. Différentes étapes de simulation sont ensuite présentées permettant la prise en compte de parties additionnelles telles qu'un transition en entrée permettant l'excitation de la lentille, l'ajout d'une structure métallique en sortie pour optimiser le rayonnement de la structure ou bien encore la partie d'alimentation DC des cellules en colonnes. L'ajout de toutes ces parties additionnelles vient perturber le rayonnement global mais la reconfigurabilité en diagramme de rayonnement est toujours assurée. La version finale de cette lentille avec toutes les parties nécessaires à son fonctionnement a permis la réalisation d'un prototype assurée par la société Lithos pour la réalisation du FPMS (circuit multicouches) et la société Voltakap pour le report des diodes varactor et des inductances (alimentation DC).

Ce manuscrit se termine par une conclusion et des perspectives concernant les travaux présentés et la technologie FPMS.

# INTRODUCTION

In recent years, the development of 5G and beyond technologies has been a major focus of research and development in the field of wireless communications. These technologies promise to deliver faster data rates, lower latency, and greater capacity, enabling a wide range of new applications and services. This development comes with the need for high-frequency reconfigurable components where their performance can be dynamically modified. Usually, in the microwave domain, one reconfigurable device will have only one associated function that can be controlled.

In 2016 has been developed the Field Programmable Microwave Substrate (FPMS)[1] which can perform multiple microwave functions using a single device. The FPMS consists of small unit cells that can be individually reconfigured to a range of positive dielectric constants or negative ones. Programming positive materials sandwiched between two negative materials results in a slab waveguide that behaves like a substrate-integrated waveguide. With this technology in mind, an international ANR/NSERC project began on March 2019 on the subject of "Reconfigurable Wireless Components using Field Programmable Microwave Substrate". The partners of this project are the IETR and XLIM for the French side, and Ontario Tech University, Carlton University and Orbcom for the Canadian side. This project has three main objectives:

- Optimization and development of an analytical model of the actual unit cell of the FPMS
- Extend the working of the unit cell up to the millimeter wave and development of a new FPMS board
- Design and implementation of reconfigurable circuits and antennas up to millimeter wave using the FPMS

My thesis is based on this project and focuses mostly on two parts. Firstly, the study and development of a new unit cell and a new FPMS board in X band for circuit application and secondly the use of FPMS technology in order to design reconfigurable antennas and circuits. As this thesis work is done in a ANR/NSERC project, some parts of my research, especially reconfigurable circuit with FPMS could be re-used for others partners, it is the case for example for the new FMPS concept in X band.

To design some reconfigurable antennas, we will use the most important characteristic of the FPMS technology: the ability to control locally the dielectric constant. This property will be used to develop leaky-wave antennas but most importantly reconfigurable inhomogeneous lens antennas.

Due to the fact that this ANR/NSERC project took place for the most part during the Covid crisis, difficulties were encountered in particular in the creation of prototypes and their measurements.

# Organization of the manuscript

In the first chapter concerning the state-of-art, we first focus on reconfigurable radio frequency systems. The chapter is separated between reconfigurable circuit applications and reconfigurable antenna applications. For the antenna applications, an overview of different techniques to achieve beam scanning properties is done, with an emphasis on electronic reconfigurable systems. In the end, a focus on inhomogeneous lenses is done.

The second chapter deals with the design and realization of FPMS circuit in the X-band. The first part of this chapter is the study of the key element of the FPMS technology: the Unit-Cell (UC). The UC will develop in order to work in the X-band. In the second part of this chapter, an implementation of the FPMS board is presented. This FPMS is made of a combination of $16 \times 16$ UC. For this part, a new prototype with FPMS technology has been developed and its manufacturing is in progress by the Voltakap company. This prototype based on my work about the new unit cell will be used by all the project partners and especially by XLIM to validate their optimization algorithm concerning reconfigurable filters and others microwave circuits.

In the third chapter, a leaky-wave antenna using FPMS technology is designed, manufactured and measured. The leaky-wave antenna presented thanks to the control of the unit cell achieved beam-steering at a fixed frequency. This work has been done in collaboration with OntarioTech in Canada.

In the last chapter, the capability of the FPMS to control the dielectric constant is used in order to realise an inhomogeneous lens antenna. The chosen type of lens is a plate Mikealian lens. In the first part of this chapter, a study of the capability of the beam-steering of a passive Mikeallian lens is done. In the second part, an implementation of a fully reconfigurable Mikealian lens antenna is presented using FPMS technology. A multilayer PCB prototype based on FPMS concept has been manufactured by Lithos and

Voltakap companies.

At the end of this manuscript, conclusions are given alongside some prospects for future work.

Chapter 1

# State of the art

## 1.1 Introduction

The main objective of this thesis research work is to implement some Field Programmable Microwave substrates (FPMS), as explained in the introduction, in order to design reconfigurable circuit functions (filters, waveguides, dividers, phase shifters) and reconfigurable antennas (beam scanning antennas, beam shaping antennas...). Before designing such reconfigurable systems, a state-of-the-art of reconfigurable circuits and antennas has been carried out and is presented in this first chapter. The first section will concern active and reconfigurable microwave basics circuits with discrete semi-conductors components but also with metamaterials. The second section will deal with the design and manufacturing of reconfigurable antennas: Butler matrix, Rotman lens, reflect and transmit arrays but also reconfigurable dielectric lenses and especially inhomogeneous lenses, as it is one of the objectives of the research of this thesis. This state-of-the-art is not exhaustive but gives several examples of circuits or reconfigurable antennas.

## 1.2 Reconfigurable Circuit

Reconfigurable microwave circuits are a type of electronic circuit that can be easily reprogrammed in order to perform different individual functions, such as reconfigurable frequency filters, reconfigurable power dividers, or phase shifters. Classically, one circuit can provide a single microwave function, and this is the main difference with the FPMS, whose objective is to be a reconfigurable system that can be switched from one function to another with the same artificial substrate. In this state-of-the-art, we focus on reconfigurable circuits mainly manufactured thanks to the use of classical PCB technology, as it will be done during our thesis work with designs based on FPMS implementation.

### 1.2.1 Reconfigurable Filter

Radiofrequency (RF) filters are essential components in wireless communication systems that are used to separate and isolate different frequency bands. RF filters can be classified into four main types: low-pass filters, high-pass filters, band-pass filters, and stop-band filters.

Low-pass filters allow frequencies below a specific cut-off frequency to pass through the filter while attenuating higher frequencies. On the other hand, high-pass filters allow frequencies above a specific cut-off frequency to pass through the filter while attenuating lower frequencies. Band-pass filters allow a specific frequency band to pass through the filter while attenuating frequencies outside of that band. Stop-band filters, also known as band-reject filters, attenuate a specific frequency band while allowing frequencies outside of that band to pass through the filter.

The ultimate Reconfigurable filter would be one that can be tuned for all its parameters, center frequency, bandwidth, and order.

In [2], the authors present a stop-band filter. In this design, the frequency and bandwidth of the filter can be controlled by using distributed coupling half-wavelength resonators and multimode resonators (MMRs). Varactor diodes are associated with these resonators to obtain fully reconfigurable bandstop filters between 3 and 11 GHz. The frequencies, bandwidths, and the number of stop bands are controlled thanks to the bias voltages of the different diodes. An example of manufacturing of such a design is given in Figure 1.1 for single band and dual bandstop filters using three pairs of varactor loaded MMRs.

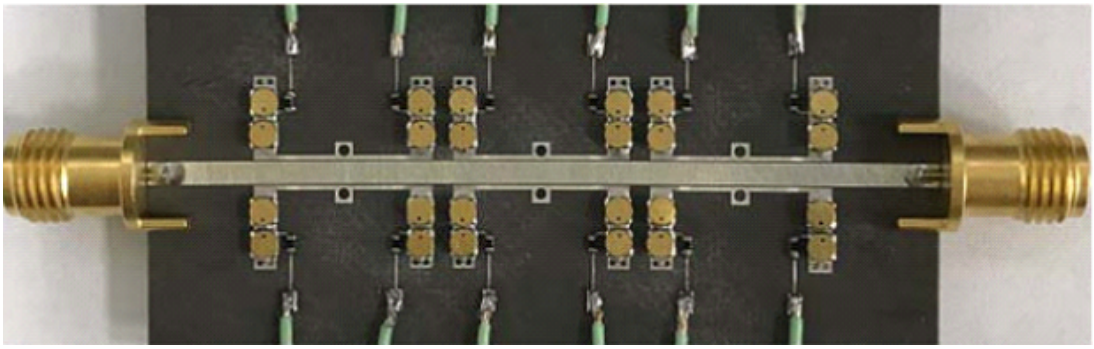

Figure 1.1 – Photograph of single-band and dual-band BSF using three pairs of varactor-loaded MMRs with a uniform size [2]

In [3] is presented a miniaturized low-pass filter (LPF) with a wide tuning range and

extended stop-band. This filter is composed of two fixed low-pass cells and a tunable bandstop cell using two pairs of varactor diodes, allowing the reconfigurability of the complete design. The wide stop-band is extended up to 10 GHz, and the overall dimension is small. Figure 1.2 shows an example of design with also experimental results.

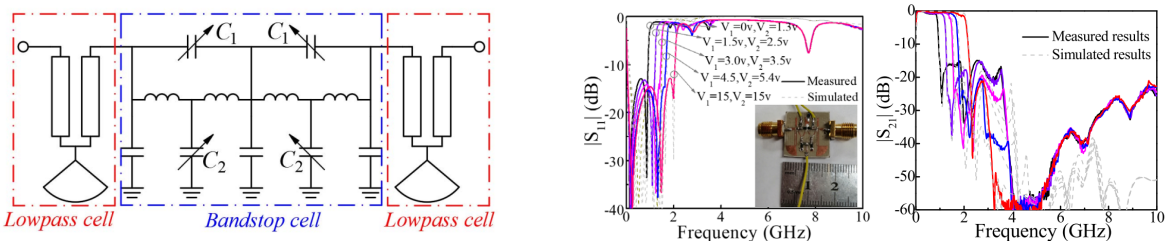


(a) (b)

Figure 1.2 – Design of reconfigurable filter and experimental results [3]

In [4], the authors present a compact reconfigurable band-pass filter in the L band based on a C-shaped resonator coupled to the source and load through varactor diodes as shown in Figure 1.3. The variation of the bias voltage of the varactor diodes and so the equivalent capacitance allows for a change in the width of the bandwidth of the filter.

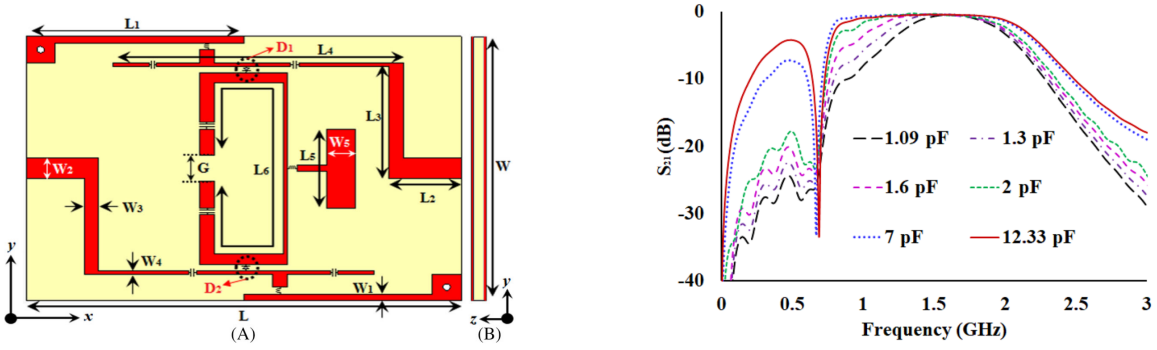


(a) (b)

Figure 1.3 – Design of band-pass reconfigurable filter and $S_{21}$ magnitude result versus capacitance value [4]

Instead of using discrete components as presented above to reconfigure the filters, agile materials can also be used. For example, in [5], the authors present a reconfigurable band-pass filter for X-band applications composed of coupled $\lambda/2$ microstrip resonators. The filter's center frequency is shifted thanks to using an RF switch based on a phase change chalcogenide compound. The switch consists of a single GeTe layer connecting

two RF terminals laterally. By switching between ON and OFF states, the authors show that it is possible to change the center frequency between 7.5 and 8.1 GHz with acceptable insertion loss (close to 2 dB).

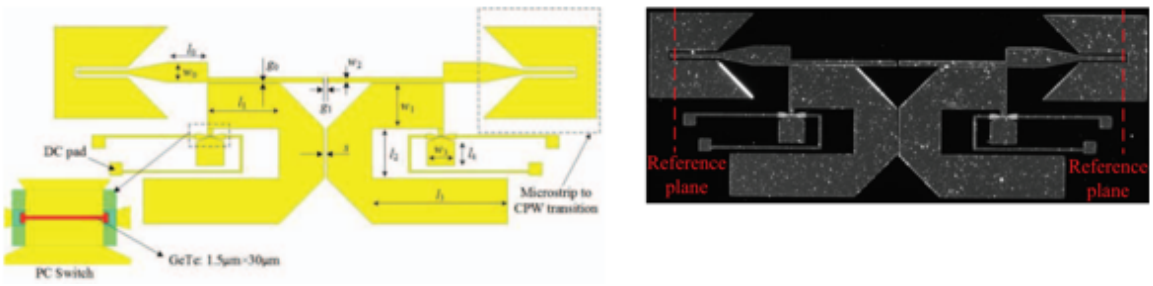


Figure 1.4 – Photograph of single-band and dual-band BSF using three pairs of varactor-loaded MMRs with a uniform size [5]

In [6] is presented the first tunable band-pass filter combining split ring resonators (SRRs) and Vanadium Dioxide ($VO_2$) based microwave switches. The electrical characteristics of the SRRs are modified through the different states of the $VO_2$: semi-conductor to metal transition. The authors demonstrate that it is possible to achieve a 10% tenability of the center frequency around 10 GHz (Figure 1.5).

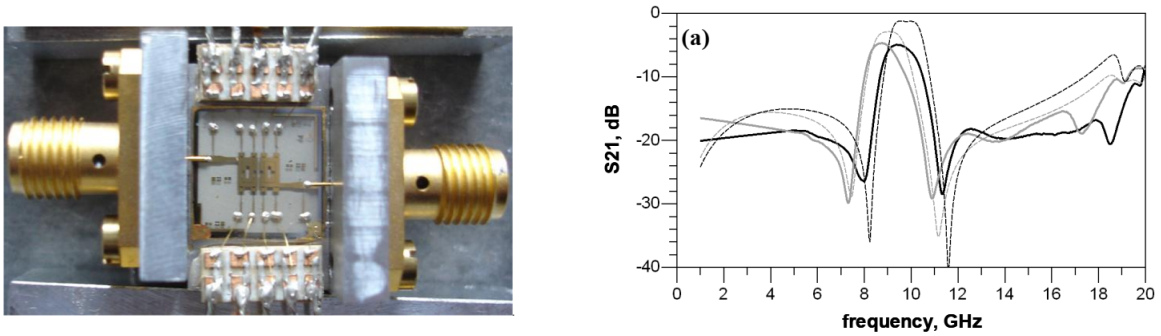


(a) (b)

Figure 1.5 – Manufacturing and results of the reconfigurable filter based on SRRs and $VO_2$ [6]

In [7], $VO_2$ switch is also used to design a reconfigurable filter. The filter is fully printed on a flexible Kapton substrate, and the $VO_2$ switch is printed through a custom ink. The authors indicate that the ON-OFF state of this switch allows changing the center frequency between 3.8 and 4 GHz (Figure 1.6).

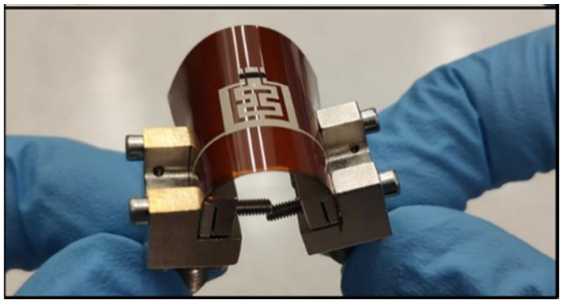

(a)

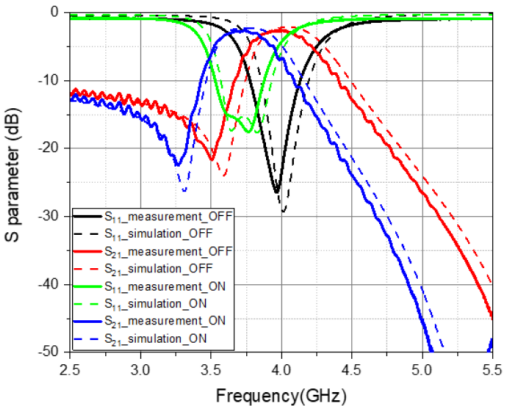


(b)

Figure 1.6 – Manufacturing and results of the reconfigurable filter on flexible Kapton substrate and $VO_2$ switch[7]

For Terahertz applications, 2D materials have also been investigated to implement reconfigurable filters, as explained in [8]. In this paper, the authors say that they can change the filter's response by using 2D materials consisting of five squares based on graphene or black phosphorus. Unfortunately, only simulations are shown.

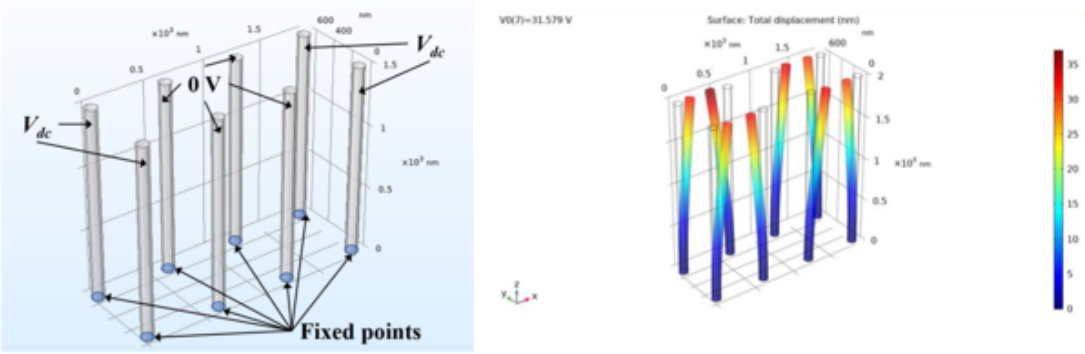


Figure 1.7 – Vertically aligned carbon nanotubes [9]

Carbon Nanotubes (CNTs) have been studied to design reconfigurable filters [9]. The authors present a novel concept of tunable and miniaturized filters with reconfigurable variable capacitors (voltage control) based on vertically aligned carbon nanotubes as represented in Figure 1.7. The authors study how the single nanotube moves depending on the DC bias voltage applied in a $2 \times 4$ CNT matrix (Figure 1.7). Depending on the applied voltage and height of nanotubes, the theoretical ratio between $c_{max}$ and $c_{min}$ can be important, as represented in Figure 1.8 (simulations). Different miniaturized filters

(low-pas0s, high-pass and band-pass) are designed with a matrix of CNTs surrounding an IDC (Figure 1.9). Experimentally, the frequency reconfigurability of filters depending on the applied voltage is limited, but the voltage range is also limited (0 or 4/8 V). It is also shown that the insertion loss is significant(10 dB).

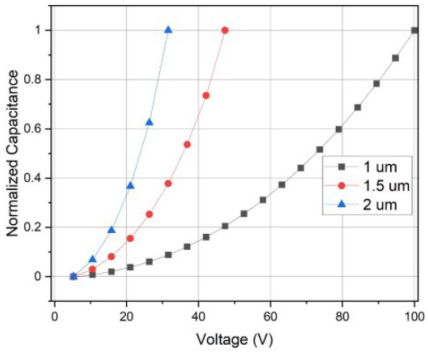


Figure 1.8 – capacitance variation versus applied voltage and height of CNTs [9]

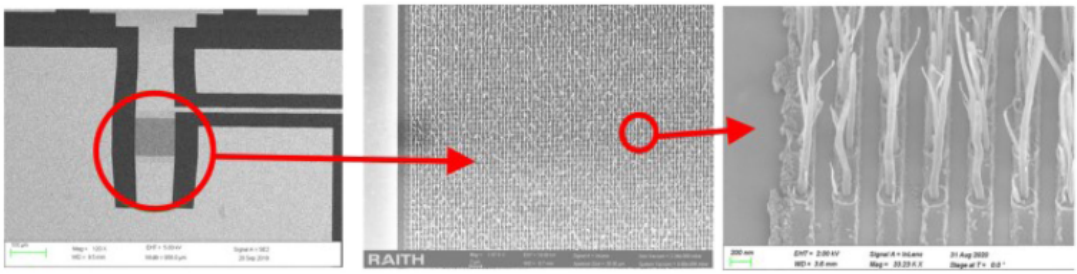


Figure 1.9 – IDC and VACNTs [9]

### 1.2.2 Reconfigurable power dividers

Power dividers are often used in communications or radar systems to divide the input power between two or more outputs. Interesting works have already demonstrated the design and characterization of reconfigurable power dividers. The first example is detailed in [10] with a reconfigurable $1 \times 4$ power divider at 2.45 GHz. Depending on the states of SPDT switches, the authors show that it is possible to route the input power to one of the four outputs. The insertion loss is acceptable, whatever the chosen output, between 1.2 to 1.9 dB. The isolation is also good, between 25 and 30 dB. In [11], a tunable Wilkinson power divider is proposed based on one unit cell (Figure 1.10) with a varactor diode associated with a transmission line with particular characteristic impedance and length.

Other varactor diodes are associated with tuning the frequency. The authors demonstrate that their design with two unit cells (1 and 2) allows for a change of the working frequency from 0.96 to 1.73 GHz.

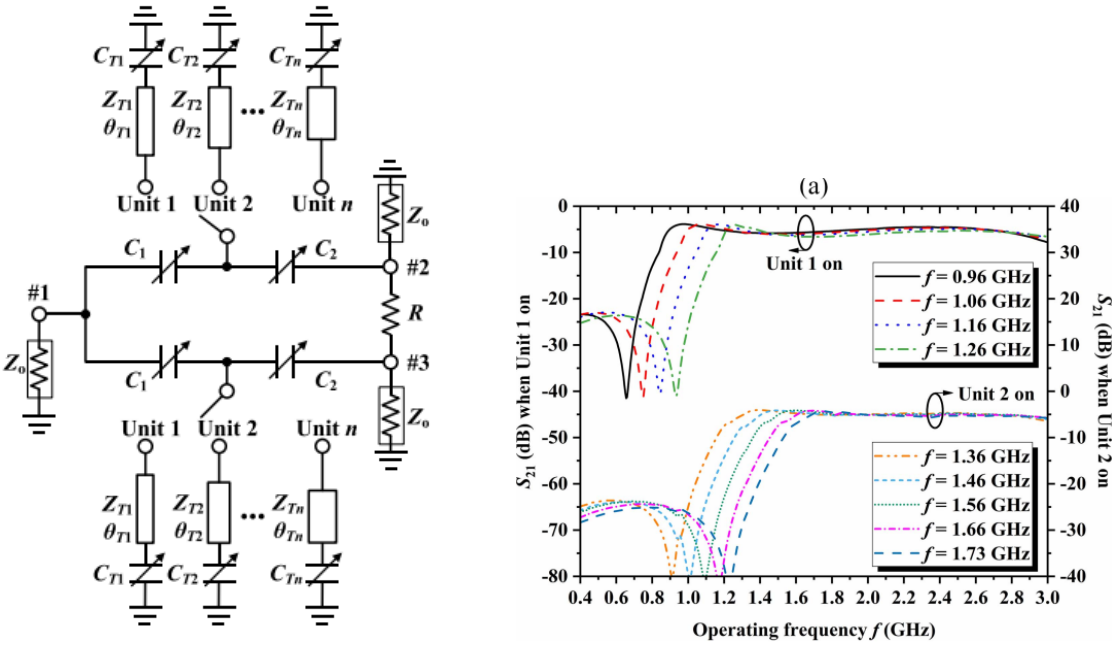


Figure 1.10 – Reconfigurable Wilkinson power divider and results of tunability [11]

In [12], the authors present a reconfigurable power divider using a hybrid matrix and impedance tuners based on controlled varactor diodes. As a result, they can obtain variable power-dividing ratios at one frequency (Fig 1.11). This design can also give the opportunity to change the frequency for a classical 3 dB power division.

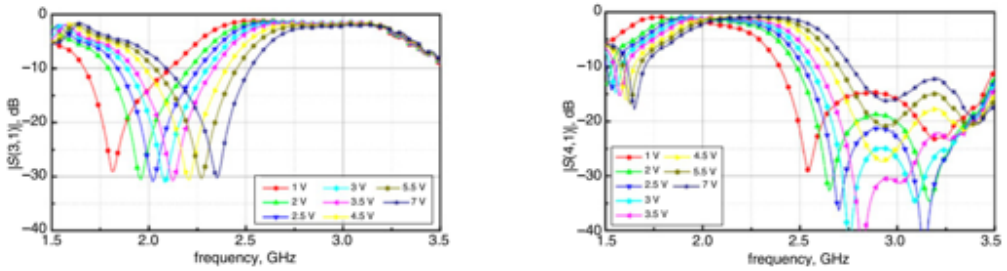


Figure 1.11 – Reconfigurable divider with variable power dividing ratios [12]

In [13] is presented a five ports power divider with variable power routing. This design

presented in Figure 1.12 allows working with different modes: direction transmission to one output, equal power division between two output ports, and division between the four output ports. Eleven states with only 6 varactor diodes give this high degree of reconfigurability. An experimental prototype at 3 GHz validates the results.

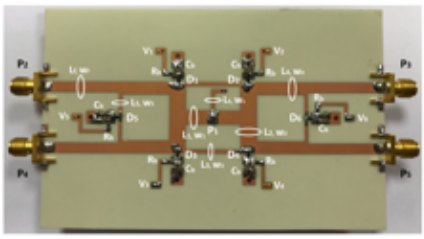

| Transmission state | Insertion loss (dB) |
|---|---|
| Direct to $P_2$ | 1.3 |
| 2-way division ($P_2$ & $P_4$) | 4.3 |
| 2-way division ($P_2$ & $P_3$) | 3.9 |
| 2-way division ($P_2$ & $P_5$) | 4.3 |
| 4-way division | 6.5 |

Figure 1.12 – Reconfigurable power divider with high degree of reconfigurability [13]

The authors in [14] present a wideband reconfigurable power divider (PD) /combiner (PC) for 5G millimeter-wave applications (28-38 GHz band). After detailing a passive device design realized in 40-nm CMOS technology, they implement an active reconfigurable divider based on a classical Wilkinson PD/PC using the SPDT switch function (Figure 1.13). This device allows the distribution of the signal to each channel for the beamforming transmitter or to combine the incoming signal for the receiver part.

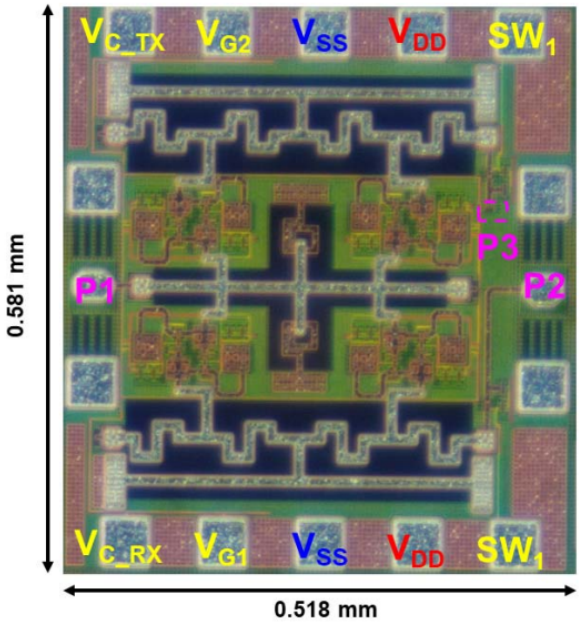


Figure 1.13 – Reconfigurable PD/PC for 5G millimeter applications [14]

### 1.2.3 Reconfigurable phase shifters

Many designs and different types of phase shifters exist, especially for beam steering phased array antenna designs from microwave to millimeter-wave range. The phase shifters can be digital with a particular number of bits and a corresponding phase increment or can be analogical with a continuous variation of phase, for example, depending on the Bias voltage of varactor diodes. This state-of-the-art concerning phase shifters is not exhaustive but gives only some examples of phase shifters configurations. The first example is given by [15], where the authors design a miniaturized compact reconfigurable Half-Mode SIW (HM-SIW) phase shifter with PIN diodes between 4.5 and 7 GHz. The concept is based on a HM-SIW (Figure 1.14) where PIN diodes are connected on the opposite side of the wall of vias. Depending on the bias control of the PIN diodes, this design allows changing the phase of the transmit signal ($S_{21}$) with a stable phase shift on a relatively wideband.

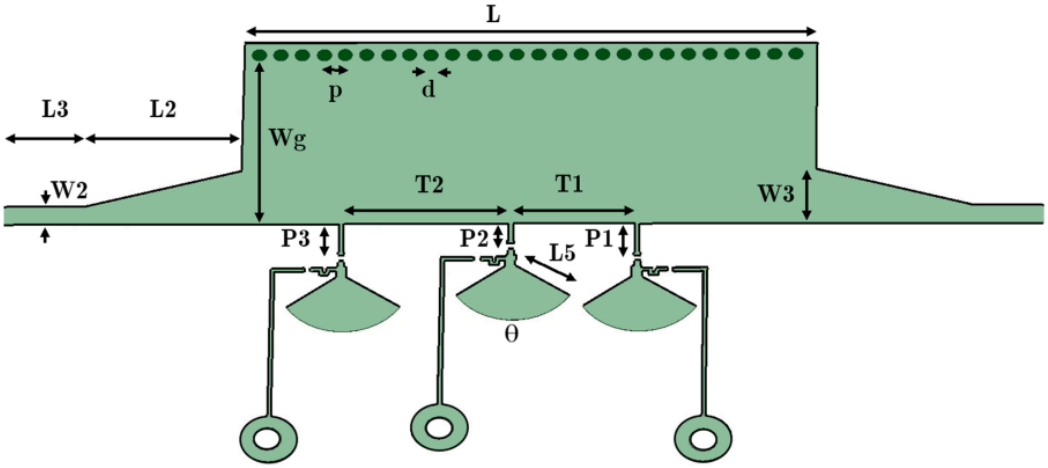


Figure 1.14 – Reconfigurable HM-SIW phase-shifter with PIN diodes [14]

In [16], the authors design simple phase shifters with two-phase shifts depending on the bias control of two PIN diodes. They obtain a wide operating bandwidth and compact size for this phase shifter. A good phase deviation of 5° has been realized for a wide band frequency.

Many phase shifter designs are based on hybrid couplers with reflective microstrip terminations to obtain a continuous phase variation. The first example is given in [17], where the authors optimized a 360° phase shifter in Ku and Ka-band. The Hybrid coupler (two outputs) is loaded by a particular load (composed of varactor diodes and microstrip

lines) shown in Figure 1.15.

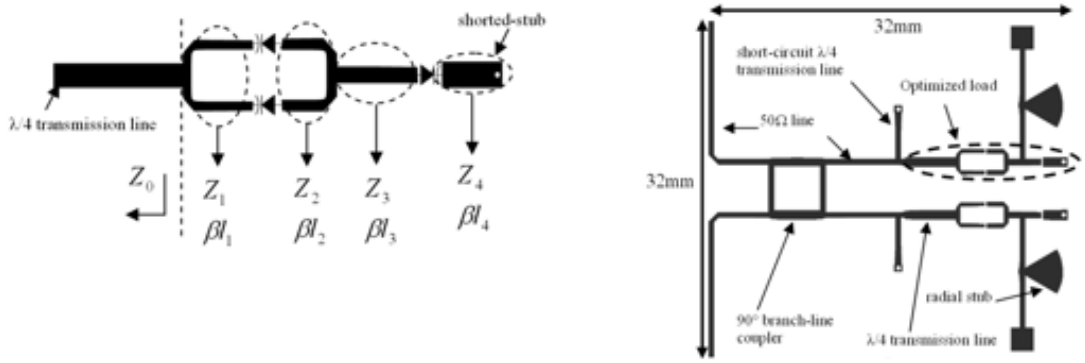


Figure 1.15 – Continuous phase shifter in Ku-band [17]

The authors obtain a maximum of 360° phase shift around 12 GHz and with insertion loos close to 3 dB mainly due to the input resistor of the varactor diode. The same design has also been implemented in Ka-band for SATCOM applications, and the insertion loss increases up to 4.5 GHz. Such a design can after be associated with microstrip patches to design an active phased array antenna in order to create a beam steering antenna [18].

In [19], the authors present quite the same design but with another kind of load associated with the hybrid coupler. As a result, they obtain more than 360° maximum phase shift with limited insertion loss between 1 and 3 dB.

In [20], the authors also implement a phase shifter based on a hybrid coupler loaded with microstrip line terminations. The electrical length of the lines is modified to change the phase shift thanks to using a selectively metalized plate placed inside a microfluidic channel (Figure 1.16). The last mechanical part is placed in close proximity to the lines, and their electrical length is changed through a capacitive RF short mechanism. The insertion loss varies from 0.5 to 0.85 dB at 9.5 GHz. The only disadvantage of this solution is the time actuation with 1.95 s to cover the 360° phase shift.

All the designs of reconfigurable active circuits, whether they are phase shifters, power dividers, or filters, do not allow to modify the function of the elementary design. Our objective in this thesis work is to implement a reconfigurable microwave substrate to change its behavior between different functions to pass, for example, from a filter to a phase shifter or a power divider. The field Programmable Microwave Substrate should make it possible to achieve this very high degree of reconfigurability as it is explained in [1], [21] for the design of reconfigurable waveguides and filters.

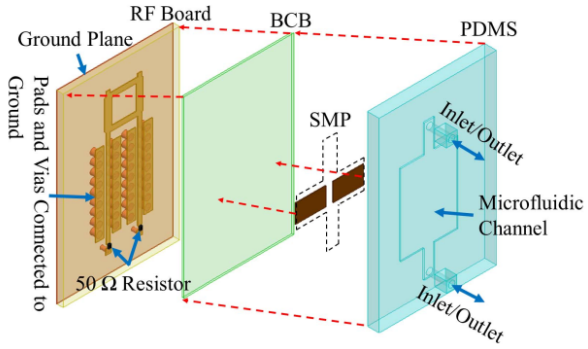


Figure 1.16 – Microfluidically reconfigurable reflection phase shifter [20]

## 1.3 Reconfigurable antennas

This section aims to understand what a reconfigurable antenna is, especially concerning radiation pattern agility with beam steering or multi-beam antennas. A non-exhaustive state of the art is done for such antennas.

In this section, we present different techniques that allow the realization of beam steerable antennae or multi-beam antennas with a focus on lens antennas, which are an important part of the thesis work. Different technologies are also through this state of the art to design and manufacture such reconfigurable antennas.

### 1.3.1 Phased arrays

A phased array is a type of antenna that uses a combination of multiple individual antenna elements that are controlled with phase shifters/amplifiers/switches in order to change the excitation (amplitude and phase) of the different elements of the array. Phased arrays have different advantages: the combination of the individual elements leads to an overall increase of directivity. Also, changing the phase shift between the array's elements makes it possible to scan the array's beam tilt angle electronically. Nevertheless, the phased arrays suffer from high loss due to phase shifter insertion loss. The first example of such an antenna is given in [18] for the design of a KA-band phased array antenna for high data rate satcom. Each multilayer patch antenna of the array is controlled thru a continuous phase shifter and gives the ability to scan electronically the beam between $-30°$ and $30°$ but with a reduced gain due to phase shifter loss (4 dB).

An example of a phased array antenna with digital phase shifters based on MEMS

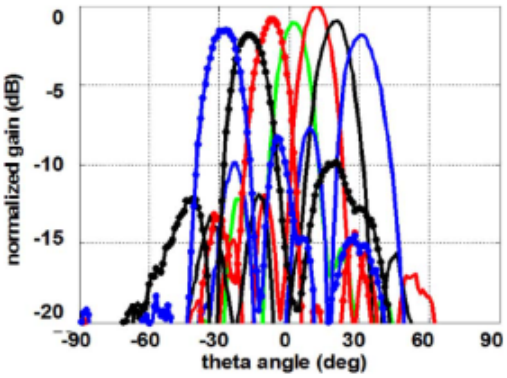


Figure 1.17 – Measured radiation pattern of the array at 30 GHz [18]

technology is presented in [22]. This design allows scanning the beam at 0° and 30° at 60 GHz depending on the state of phase shifters thru the MEMS switches. .

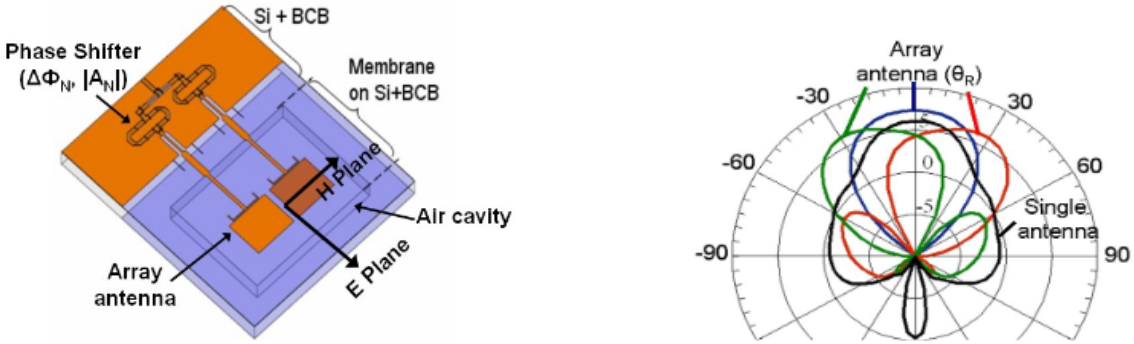


(a) (b)

Figure 1.18 – Schematic and result of the phased array antenna[22]

Another example is given in [23] where a Ka-band Passive phased array antenna is designed. This antenna is considered as a passive phased array thanks to the use of a phase-shifting mechanism based on perturbing the electric field of the slotted SIW line by adding a high dielectric slab over the slot of SIW. The authors developed a prototype working at 30 GHz and with a steerable angle between −20° and 20°.

All the last examples concern phase arrays with microwave phase shifters associated with the radiating elements. However, another solution is to implement digital beam-forming phased arrays with one RF chain for each antenna, like for SIMO and MIMO configurations. The advantage is to avoid implementing microwave phase shifters with high loss in order to improve antenna efficiency. But in this case, post-processing is needed

to achieve beam scanning capability. A first example is given in [24] where a metamaterial-based linear phased array antenna is designed around 5 GHz. Periodic metal strips are added to the metamaterial patches to improve the bandwidth and to obtain a wide scanning angle. For both E and H planes, the authors indicate that this design allows scanning of the beam between $-70°$ and $70°$ with a limited gain variation of 3 dB under a wide bandwidth. The main disadvantage of digital beamforming concerns the number of TX/RX modules (one by antenna element) that can increase the cost of such a solution, especially in high frequencies (millimeter waves). Some works have been investigated to reduce this number of channels, for example, by using sparse arrays. One example is given in [25] for a passive imaging system in the X-band. The authors have optimized the number and placement of the array element to obtain quite the same radiation pattern as for a full antenna array. Furthermore, by the use of active switches Sub-matrix, they use only two RX channels. Figure 1.19 gives an example of system integration.


(a) (b) (c)

Figure 1.19 – Concept and prototype of the phased array antenna[25]

## 1.3.2 Multi-beam antennas and beam formers

### 1.3.2.1 Butler Matrix

A butler matrix can be used to feed an antenna array. The Butler matrix is most of the time composed of N inputs and N outputs. The goal of the butler matrix is that each input of the system provides a precise phase shift between all the output (antenna elements). Meaning that associating the matrix to an antenna array creates a multi-beam antenna with different directions of beams depending on the exciting input port. The butler matrix is composed of 3 main elements: 3 dB/90° hybrid couplers, passive phase

shifters, and crossover. The schematic of a standard $4 \times 4$ Butler Matrix is presented in Figure 1.20a. The Figure 1.20b show a possible implementation at 60 GHz using SIW technology [26]. Now as mentioned previously, a Butler matrix is not an antenna but a beamformer. It needs to be associated with an antenna array. An actual implementation is presented in Figure 1.21[27], associating the SIW Butler matrix with an array of slots antenna. As expected, the antenna can produce 4 distinguish beams at respectively 41°, 15°, −15° and −41°. The maximum measured gain is at 17.5 dBi at 60 GHz.

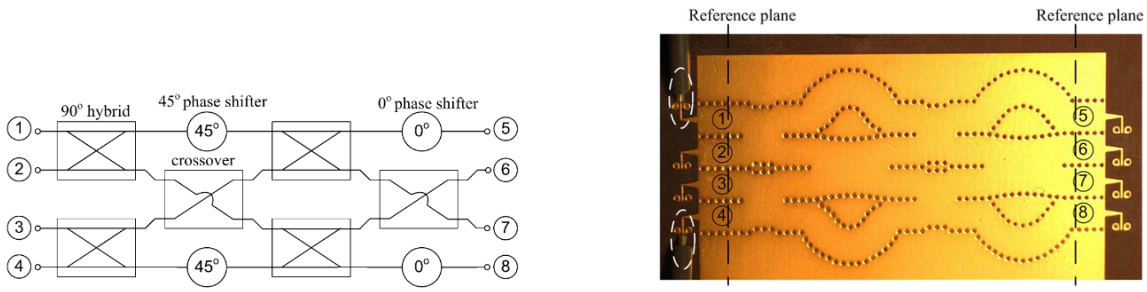


(a) (b)

Figure 1.20 – $4 \times 4$ Butler Matrix[26]: (a) Schematic, (b) SIW implementation at 60 GHz

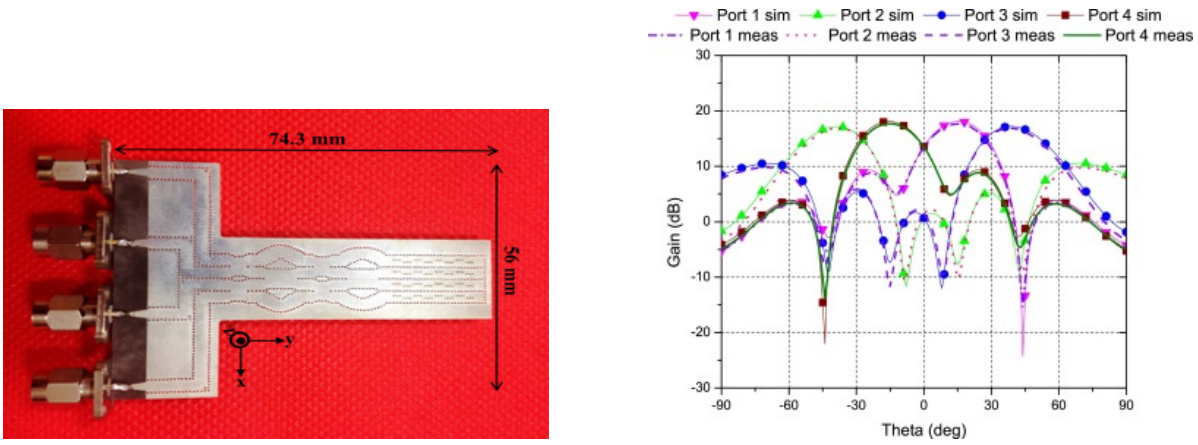


(a) (b)

Figure 1.21 – Antenna prototype and results of a $4 \times 4$ Butler Matrix associated with a slot antenna array[27]

The complexity of the Butler matrix increases with the number of input and output ports of the matrix. For example, the standard $4 \times 4$ Butler matrix uses four 3 dB/90° hybrid couplers, 4 phase shifters, and 2 crossovers. Now a standard $16 \times 16$ Butler matrix

would need 32 3 dB/90° hybrid couplers, 24 phase shifters, and 60 crossovers. It makes this type of structure challenging to fabricate and with very high loss due to the different components of the matrix. However, reducing the number of elements used to create the Butler matrix is possible. An example is given in Figure 1.22a for a four-by-four Butler Matrix [28]. This design aims to combine phase shifters and hybrid couplers into the same elements. It allows to reduce the complexity with only four complex couplers and one crossover. The created beams can be observed in Figure 1.22b with a reasonable accuracy between simulations and measurement for beams direction between −45° and 45° at 6 GHz.

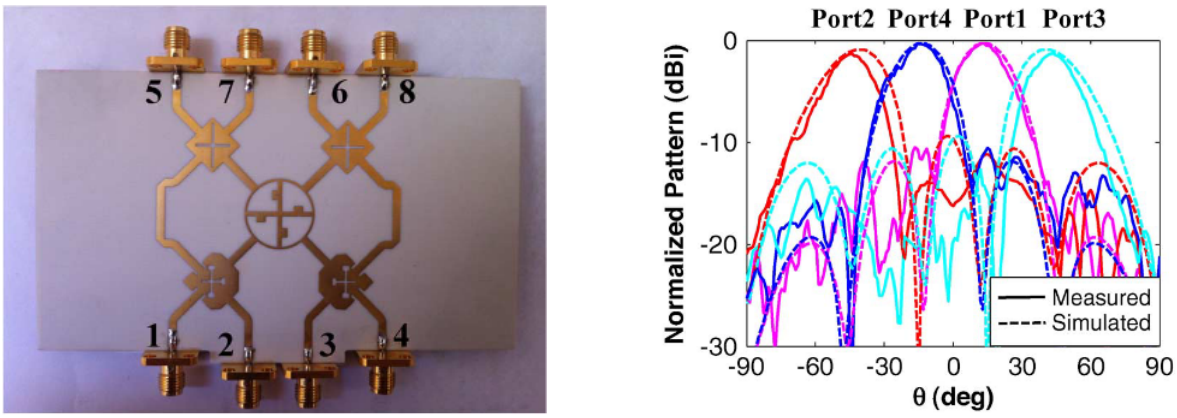


(a) (b)

Figure 1.22 – 44 Butler Matrix[28]: (a) Photo, (b) Normalised gain

In [29], a 16 by 16 Butler Matrix is designed. The complexity of the design has been reduced by the authors using eight ports hybrid coupler and innovative access to the board (inputs and outputs). The final design is presented in Figure 1.23, with the created beams when the matrix is combined with a linear array at 10 GHz.

#### 1.3.2.2 Rotman lens

Rotman lens, like Butler Matrix, is a beamformer. It was first described in [30]. It follows the same objective as the Butler matrix: for each input of the lens, it allows obtaining a specific phase shift between the outputs and so a particular beam direction.

Similar to the Butler matrix technology, a lot of work has been done in order to reduce the size of the Rotman lens and increase the bandwidth and the scanning angle range. In most cases, Rotman lenses are limited to ±30° of beam scanning angle. However, in [31],

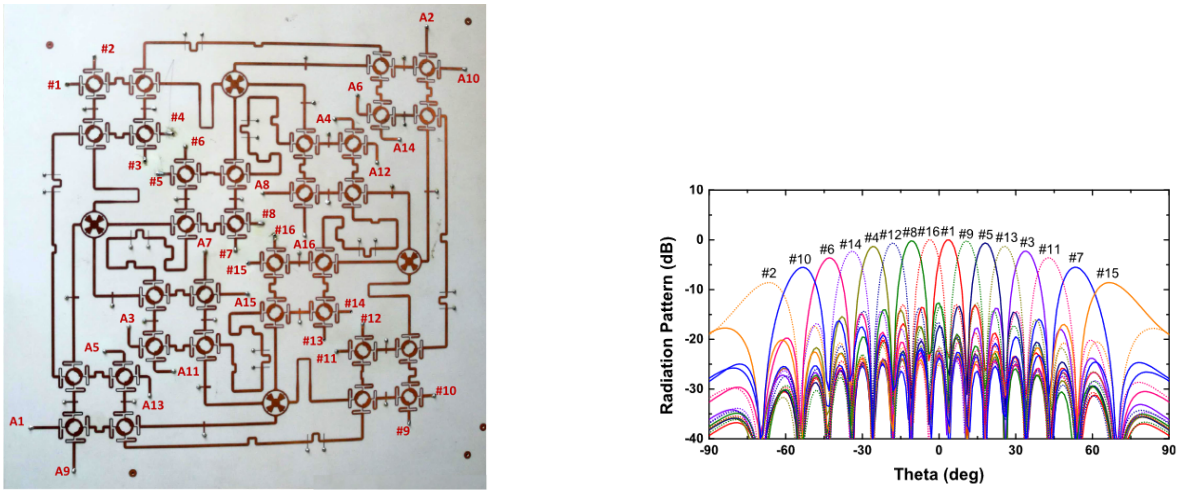


(a) (b)

Figure 1.23 – 16 by 16 Butler Matrix[29]: (a) Photo, (b) Radiation patterns at 10 GHz

the authors present a Rotman lens that achieves ±48° beam scan, at 24 GHz (Figure 1.24). The lens is made in SIW technology, and the delay line is realized with Ridged Waveguide Technology.

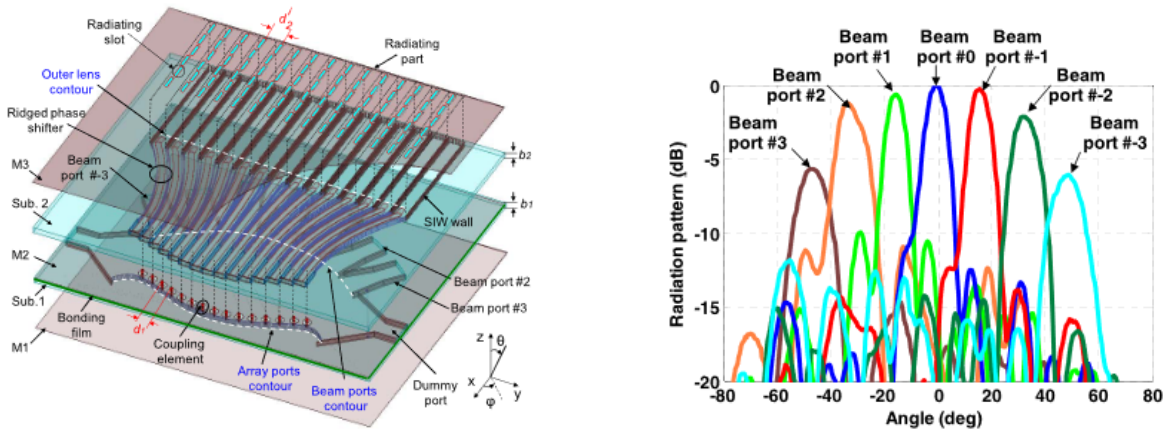


(a) (b)

Figure 1.24 – Rotman lens[31]: (a) schematic, (b) Measured normalized radiation patterns at 24 GHz

In [32], a standard Rotman lens that has a ±30° scanning angle has been associated with precise delay lines and tunable phase shifters. Using a pin diode, the phase shift can be switched between 0° and 180°. Depending on the state of the phase shifter, the configuration allows the antenna to tilt the beam between −60° and 0° or 0° and 30°.

### 1.3.3 Reflect arrays and transmit arrays

Reflect arrays and transmit arrays are a class of directive antennas that work almost the same way. A reflect array is composed of multiple radiating elements that are mounted on a flat surface. The surface is made in order to reflect a spherical incident wave into a plane wave in some given directions. Each element that composes the array is created to control the phase of the reflection. The same idea is used for the transmit array, but this time the incident wave goes through the array. The phase is also controlled by the elements that compose the array. For both structures, the plate surface is illuminated by a primary focal source, which prevents the use of a feeding network and reduces the loss of transmission lines.

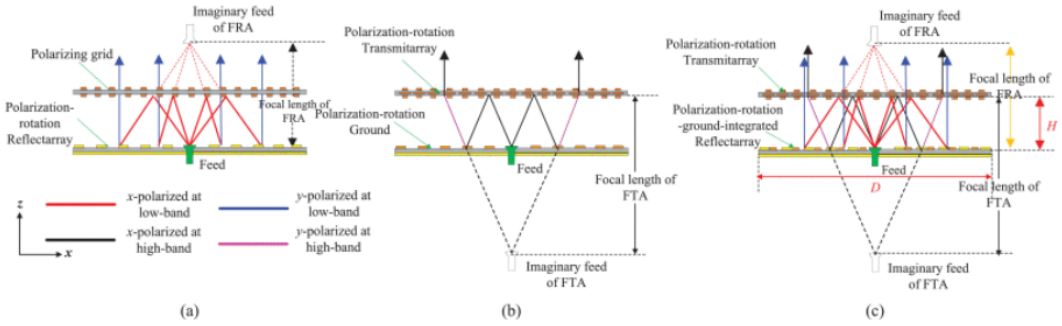


Figure 1.25 – Configurations and principles of three different antennas. (a) Folded reflectarray. (b) Folded transmit array. (c) Folded reflectarray and folded transmit array hybridized design [33]

One drawback of the reflect/transmit arrays is the long distance needed between the focal feed and the radiating surface. To reduce the global size of such concepts, folded versions of the reflect array and transmit array have been developed. The idea is to add a polarizing grid to the antenna. Depending on the polarization of an incident wave, the polarizing grid will transmit or reflect it. This added layer allows to reduce the distance between the feed and the flat array. In [33], the authors combine a Folded reflect array and folded transmit array in order to create a dual-band antenna. Depending on the band, the antenna will act as either a reflect array or a transmit array. Figure 1.25 explain the concept behind folded transmit array, folded reflect array, and the hybrid version.

Combining reflect and transmit arrays into the same design can be interesting. In [34], the authors present a reconfigurable antenna that can be switched between a reflectarray and a transmit array. To achieve a reconfigurable system, they use a FSS (Frequency

Selective Surface) that can be controlled by using a pin diode. Depending on the state of the diode, the FSS will act as a band-pass or a stop band for the incident wave. When the FSS acts as a band-pass, the antenna will behave as a transmit array, and vice versa. The proposed antenna achieves 18.2 dBi gain in reflecting configuration and 20.9 dBi gain in the transmitting configuration at 11 GHz. In [35], a combination of both configurations is also achieved; this time, the antenna's behavior depends on the primary source's polarization.

To achieve electronic beam steering antennas with a reflect array, the idea is to add tunable components into the reflect array. For example, in [36], PIN-diode is integrated into the microstrip patch that is the basic element of the reflectarray. Thanks to the PIN-diode, each patch has two possible phase states: 0° and 180° phase. This allows the creation of a 1-bit reconfigurable reflectarray. The advantage of this approach is to have a relatively simple bias circuit but at the cost of reducing antenna efficiency and increasing side lobe level due to the large phase quantization [37]. Using the same technique, a bigger version: 40 × 40 1-bit reconfigurable array is presented in [38].

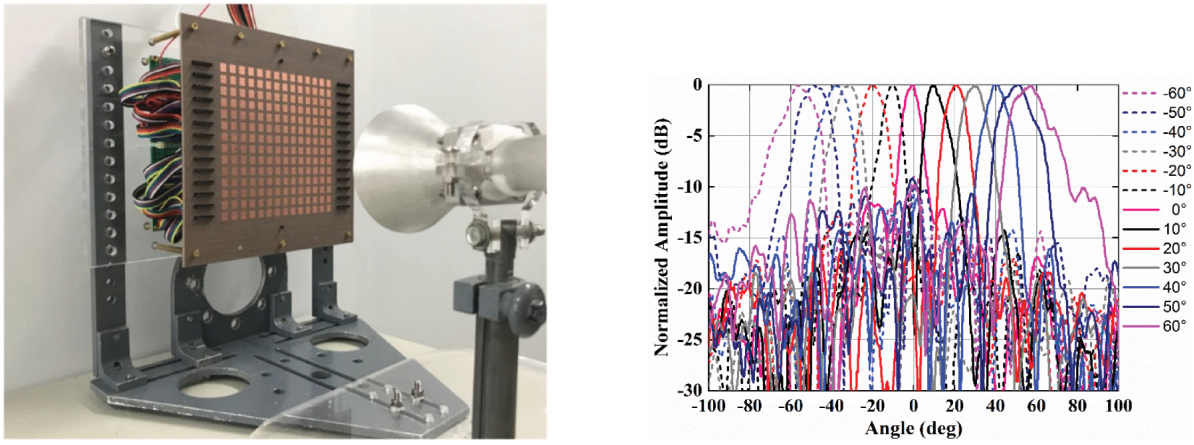


(a) (b)

Figure 1.26 – 14 × 14 1-bit reflectarray in X band [36]: (a) Antenna prototype, (b) Measured radiation pattern in the YOZ plane at 11.5 GHz

Using varactor diodes, it is possible to achieve continuous phase shifting. An example of this approach is given in [39]. Associating a varactor diode to an FSS, the author could control the phase of each element of the reflectarray up to 270° with a continuous phase tunability. In order to reduce the complexity of the system, only a 1-D reflectarray has been realized. The final prototype achieves ±55° beam scanning coverage (Figure 1.27).

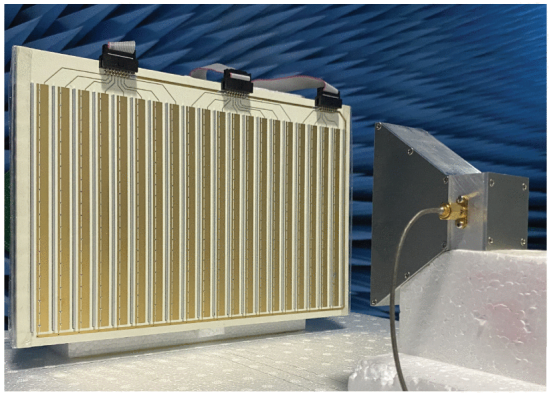

(a)

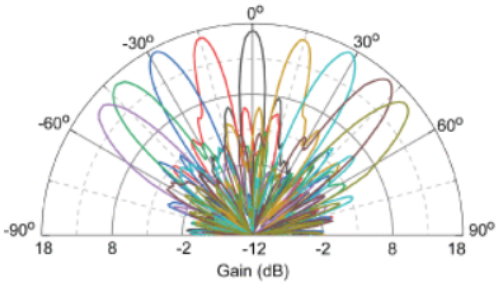


(b)

Figure 1.27 – 1-D reflectarray with an active second-order band-pass FSS [39]: (a) Antenna prototype, (b) Measured radiation pattern at 7.65 GHz

### 1.3.4 Leaky wave antennas

As it will be demonstrated in this work thesis, another way to achieve beam steering capability is to use Leaky wave antennas (LWAs). The main specificity of Leaky wave antennas is that the radiated beam is steered with frequency [40]. For some applications, such antennas can be a low-cost alternative to phased arrays or reflect/transmit arrays. A broad overview of LWAs operating principles, including the incorporation of active circuits, is given in [41]. LWAs are a type of traveling wave antenna. As such, one approach to their implementation is via modified waveguides [42].

Now if we look for the design of Leaky wave antennas using printed technology, it is possible to use the same approach thanks to the Substrate Integrated Waveguide (SIW) technology [43]. An example of a slotted SIW LWA is presented in Figure 1.28, where the beam-steering with the frequency can be observed.

The HMSIW (Half Mode Substrate Integrated Waveguide) employs only one-half of the SIW structure yet provides the same performance for frequencies above the cut-off frequency of the waveguide. Moreover, as the HMSIW is opened on one side, it can be designed to radiate close to the cut-off frequency, as demonstrated in [45] for a millimeter-wave application.

If beam steering capability according to the frequency can be useful for imaging or radar system (FMCW radars), it is not the case for communication applications. As such, a lot of research works have been done in order to cancel or control the beam steering with the frequency. As it is well known, the beam direction of a LWA varies with signal

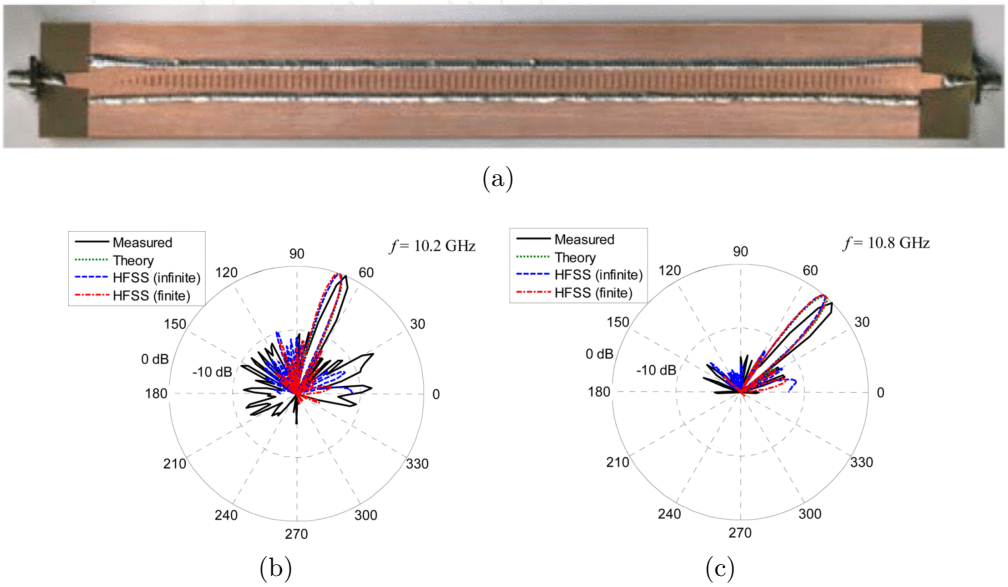


(a)

(b) (c)

Figure 1.28 – Sloted SIW LWA: (a) prototype, (b) radiation pattern at 10.2 GHz, and (c) radiation pattern at 10.8 GHz[44]

frequency. For a LWA, the main beam direction $\theta_m$ is given by [42]:

$$\theta_m = sin^{-1}\frac{\beta}{k_0} \tag{1.1}$$

Where $k_0$ is the free space wave number, and $\beta$ is the phase constant. As $\beta/k_0$ changes with frequency, the direction of the main beam also varies. To overcome this dependency on frequency, some solutions have been proposed to obtain a main beam in the broadside direction regardless of frequency, as in [46]. Such a solution provides wideband performance of the LWA with a fixed beam direction. This may be useful in certain wireless applications, but the main advantage of a LWA is its ability to scan the beam. Thus, it is desirable to preserve LWA beam steering while operating at only one frequency. To achieve this capability, the phase constant $\beta$ needs to be controlled by other means than changing the frequency. In [47], it has been shown that by loading the free edge of HMSIW with lumped capacitors, the phase constant can be adjusted in a defined manner, thereby providing control of the direction of maximum radiation.More recently, in [48] (Figure 1.29), by loading the free radiating edge with patches and by opening/shorting the patch to the ground with a PIN diode switch, the LWA design achieves beam steering at a single frequency. The work of [48] was furthered in [49], where the HMSIW structure is excited on each port, yielding a wider angular scan range

at the center frequency.

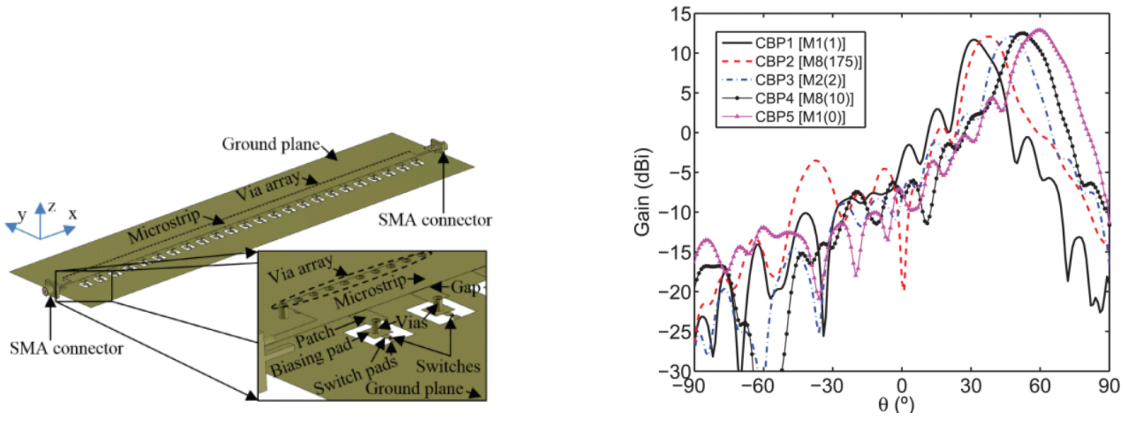


(a) (b)

Figure 1.29 – Reconfigurable HMSIW LWA: (a) design, (b) measurement at 6 GHz for a set of configuration [48]

In [50], the effective width of the waveguide is used to steer the antenna beam at a fixed center frequency. To be able to control the effective width, the authors used two rows of via holes on each side of the waveguide. One row is directly connected to the ground, and the other row (the inner row) is connected to the ground through PIN diodes. Thus, by controlling the on and off states of the diode, the authors have shown control of the effective width of the SIW structure (Figure 1.30).

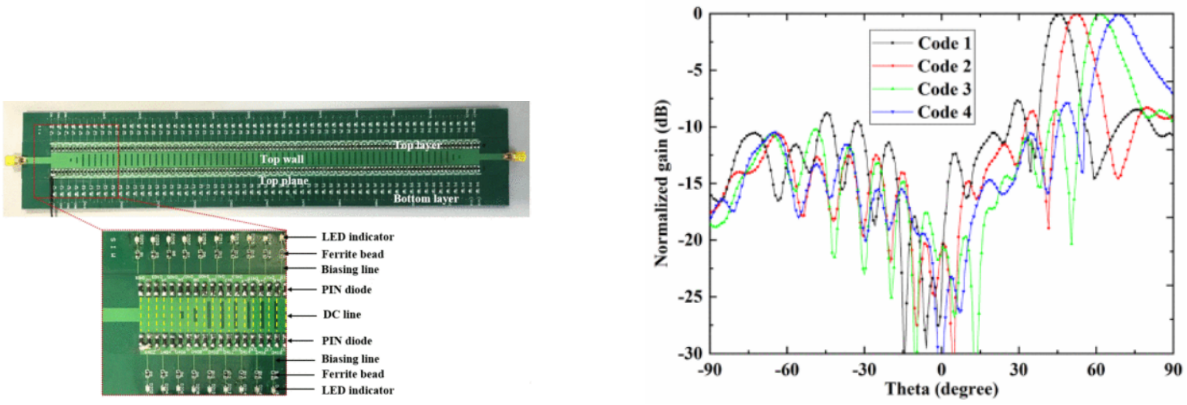


(a) (b)

Figure 1.30 – Design and measurement at 5.2 GHz of a reconfigurable SIW LWA [50]

### 1.3.5 Lens antennas

A solution to achieve reconfigurable or steerable beams can be to use lens antennas. Basically, such lenses are fed by one radiating element (primary source) and allow to focus the energy to obtain directive radiation patterns. Different beams can be obtained with beam steering or beam shaping capability if multiple sources are put behind the lens and are excited sequentially or simultaneously. Basically, a lens is a focusing device that transforms a spherical wave into a plane wave. The behavior of a lens in high frequencies is similar to that in optics; as such, lens antennas are often seen as quasi-optical systems. The focus is achieved through the modification of the wave velocity. Depending on the lens type, this modification can be achieved by changing the shape of the lens (homogeneous lenses) or by modifying the index inside it (inhomogeneous lenses). We focus here on our state of the art on inhomogeneous lenses as it is one of the objectives of this thesis work.

#### 1.3.5.1 Inhomogeneous lenses

For inhomogeneous lenses, a specific gradient index law is used to control the phase passing through the lens. Therefore for antenna applications, the objective is to get a plane wave at the output of the lens and so a focused beam. Numerous types of inhomogeneous lenses exist [51], such as Luneburg, Maxwell Fish-Eye, Eaton, and Gutman.

The most used is the Luneburg lens. This lens has an infinity of focal points. Its gradient index law is given in the formula 1.2. The relative permittivity varies from 2 in the center to 1 at the periphery.

$$n(r) = \sqrt{2 - (\frac{r}{R}^2)},\ 0 \leq r \leq R \tag{1.2}$$

This lens can be considered for 3D or 2D configurations. In a 3D configuration, the lens allows focusing of the beam in the two principal planes (H and E planes). Also, the polarization of the antenna will depend on the sources used. One problem with 3D lenses is the large dimension of such concepts. Other research works have concerned 2D configuration or plate inhomogeneous lenses. A plate Luneburg lens with a metallic covering will focus the beam in only one plane; the other plane will present a wider radiation pattern that will mostly depend on the thickness of the lens at the output. An example of a plate Luneburg lens is presented in [52] (Figure 1.31), with 9 different sources, the antenna achieved ±40° of beam steering.

The Maxwell fish-eye lens is defined by the refractive index law given by the equation

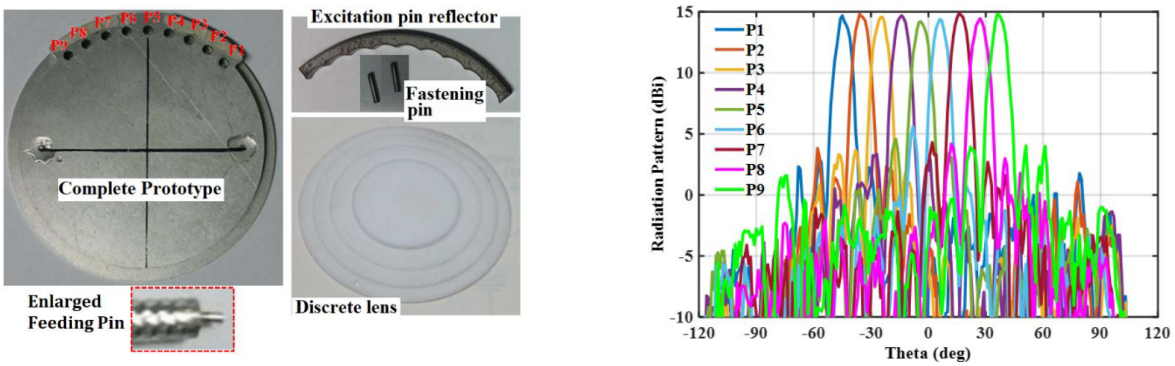


(a) (b)

Figure 1.31 – Paralle plate Luneburg lens [52]: (a) prototype, (b) Measured radiation pattern at 38 GHz

1.3. For this lens, only a half lens (Half Maxwell Fish-Eye lens) can be considered to obtain a plane wave at the output [53]. Indeed, this lens has two opposite focal points for a complete spherical design.

$$n(r) = \frac{2}{1 + \frac{r}{R}}, \ 0 \leq r \leq R \tag{1.3}$$

The Gutman lens is similar to the Luneburg lens, but the focal points are distributed on a sphere inside the lens. The refractive index of the Gutman lens is given by the equation 1.4, where f is the radius at which the focal point is located. Of course, if the focal points are placed at the periphery of the lens (f=R), it corresponds to a Luneburg lens.

$$n(r) = \sqrt{\frac{1 + (f/R)^2 - (r/R)^2}{(f/R)^2}}, \ 0 \leq r \leq R0 \leq f \leq R \tag{1.4}$$

Finally, we can also introduce the Mikaelian lens [54]. The refraction index of the Mikealian lens varies with the radial distance $r$ as defined by the following equation 1.5:

$$n(r) = \frac{n(0)}{cosh(\frac{\pi}{2T}r)}, \ 0 \leq r \leq R \tag{1.5}$$

For such a lens, the refractive index decreases from the center to the periphery of the lens, so the ray path inside the lens would have the same length. This means it has the same propagation velocity throughout the modes, similar to how an optical fiber works.

The previous example of inhomogeneous lenses all shares a common point: the focal

points are present at the periphery (or inside, in the case of the Gutman lens) of the lens. Some inhomogeneous lenses can have focal points at a particular distance from the lens (focal distance). In this case, the global system (lens + source) is less compact but can have interesting properties, especially regarding loss for high frequencies. Such an example is the Fresnel lens that can be made from different materials to obtain a plane wave [55].

#### 1.3.5.2 Manufacturing techniques

The main concern in inhomogeneous lenses is the manufacturing process and how to realize the refractive index inside the lens.

One of the first and most straightforward ways is using several different dielectric materials. In this case, the global lens is composed of different shells with different radii and values of relative permittivity [56] One drawback is that the true dielectric material with the exact dielectric parameters needs to be available. Also, the assembly of the different dielectric shells needs to be perfect in order to avoid air gaps and reduce the efficiency of the system.

Another solution can be to use only one dielectric material (Teflon, for example) and to synthesize the index law from the drilling of air holes inside it as explained in [57] (Figure 1.32). Also, with the advent of the 3D printing process [58], this solution has become less and less expensive. Moreover, it allows the realization of more complex hole patterns, increasing the accuracy of the dielectric constant control. Of course, combining the drilling process and the use of different materials can lead to a better range of possible dielectric constant values, as presented in [59].

Figure 1.32 – Luneburg lens realized by hole drilling method [57]

Another technique to synthesize the refractive index law of a lens is the use of metamaterials. The idea is to control the refractive index of a unit cell by changing its size, shape... An exemple of metamaterials based luneburg lens is prenseted in [60]. Figure 1.33 presents the size variation of the unit cell and the associated refractive index variation that allows the realization of a Luneburg lens.

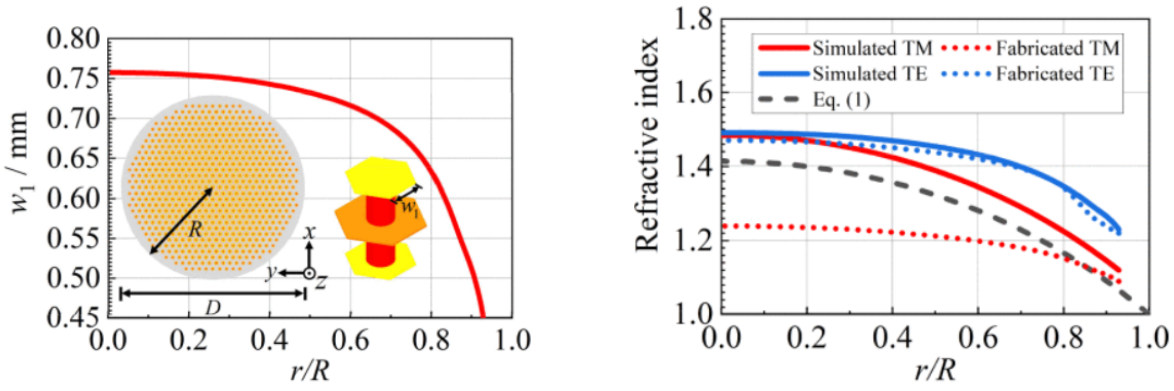


(a) (b)

Figure 1.33 – Metamaterial Luneburg lens [60]: (a) Luneburg lens model and the relationship between $w_1$ and normalized radius $(r/R)$ of the lens, (b) Refractive index distribution at 27 GHz

An innovative technological process is shown in [61]. This process allows to synthesize many dielectric constant values from one unique foam material. The principle is very simple and based on the fact that the foam material is composite of a basic material injected with air bubbles. This foam material has a basic low dielectric constant close to 1. Expelling the air bubbles makes it possible to manufacture the wanted dielectric constant values needed for the design of inhomogeneous lenses as given in [62]. One example of Luneburg lens manufacturing is given in Figure 1.34 at 60 GHz.

Inhomogeneous lenses can also be manufactured with a fully metallic process, as shown in [63]. The main advantage of this technology is the improvement of efficiency because it does not need any dielectric material. But this process needs a high drilling accuracy, especially for high-frequency concepts.

### 1.3.6 Reconfigurable lens antenna

When it needs to design a reconfigurable radiation pattern antenna based on lenses and especially inhomogeneous lenses, two main possibilities exist: by mechanically moving


(a) (b) (c)

Figure 1.34 – Plate lunburg lens [62]: (a) before pressing, (b) after pressing, and (c) Measured radiation pattern for different frequency

the primary source under the lens (mechanical beam steering) or by associating different sources behind the lens and switching between them to control the direction or the shape of the beam.

We begin this part of state-of-the-art with mechanical beam steering by moving one unique source under lenses. The first example is given in [64] where a Half Maxwell Fish-Eye lens antenna is designed at 77 GHz. The lens comprises three dielectric shells to follow the desired index law. An open-ended waveguide is then associated with this lens and moved under it to scan the beam between 0° and 50° experimentally. The results of beam steering angles are presented in Figure 1.35.

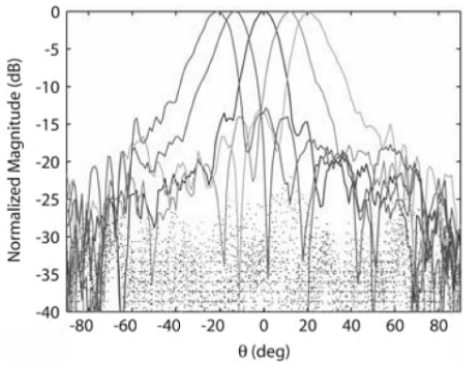


Figure 1.35 – Normalized measured [co-pol (—) and cross-pol (...)] far-field patterns at 77 GHz for the on-axis and 4 off-axis configurations [64]

A second example is given in [65]. In this paper, the authors design an LTCC-based dielectric flat lens antenna, and they obtain beam steering capability at 60 GHz by moving

the source (WR15 open-ended waveguide) under the lens. They obtain a beam steering angle from −45° to 45° with a gain variation close to 4 dB (Figure 1.36).

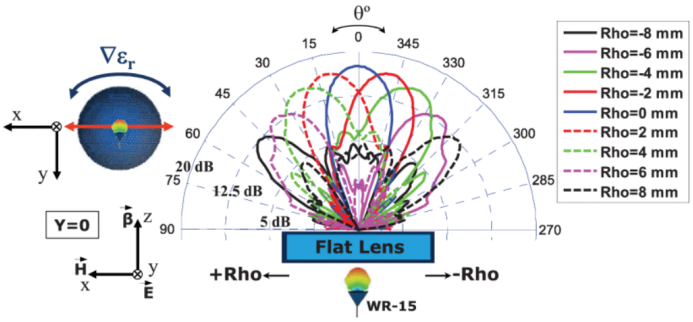


Figure 1.36 – Measured radiation patterns at 60 GHz for different feed positions [65]

Another possibility is to put several sources under the lens as it is explained in [66] where printed patches feed the Luneburg lens. A full 2-D beam-steering becomes possible, with a very wide steering range of ±60° in one plane and a smaller steering range of ±15° in the orthogonal plane at 10GHz. Even if, in this paper, several sources feed the lens, we cannot consider this prototype as an active reconfigurable lens antenna because the different combinations of feeding sources are not electronically controlled. A straightforward way to create a beam-steering lens antenna is to add an electronic switchable feeding system to the lens. An example can be found in [67]. The antenna in this paper is a Lunberg lens fed by several open-ended-ridged waveguides. Each waveguide is controlled thru an MMIC amplifier to switch electronically between the beams. The antenna achieved ±170° of beam steering with 11 dBi of gain at 60 GHz (figure 1.37). The beam width in

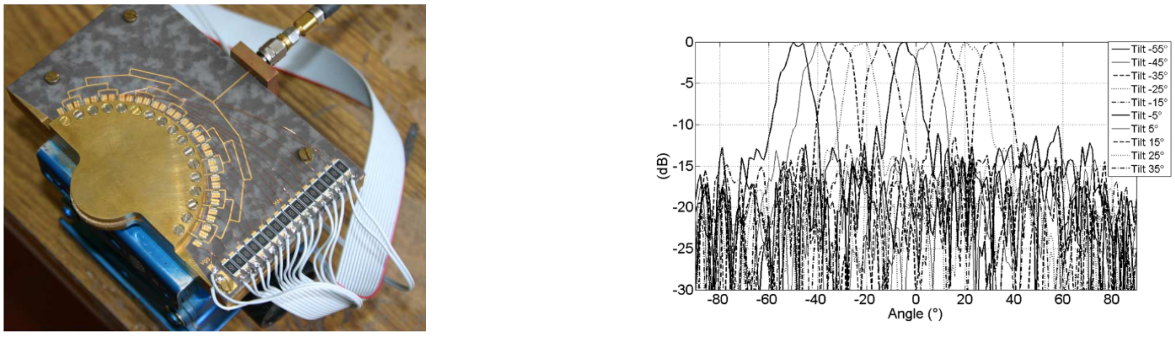


(a) (b)

Figure 1.37 – Reconfigurable lunberg lens at 60 GHz [67]: (a) Antenna prototype, (b) Measured radiation pattern for 10 different beams

the focus plane (H plane) is 10°, but it can be modified if several open-ended waveguides feed the Luneburg lens simultaneously. In this case, it becomes possible to steer the beam or shape it to obtain a quasi-sectorial radiation pattern.

We can also look at techniques that allow us to make a lens reconfigurable. The idea is to control the refraction index of the lens electronically. One example is presented in [68], where a reconfigurable Fresnel lens is built. In this design, the lens is built with reconfigurable FSS. For each unit cell of the FSS, the phase of the transmission parameter can be controlled thanks to the use of a Varactors diode. Each cell allows 180° phase tunability. This means that a plate Fresnel lens law can be realized, and more importantly, the center of the lens can be moved. This allows the antenna to achieve 2D beam steering (Figure 1.38).

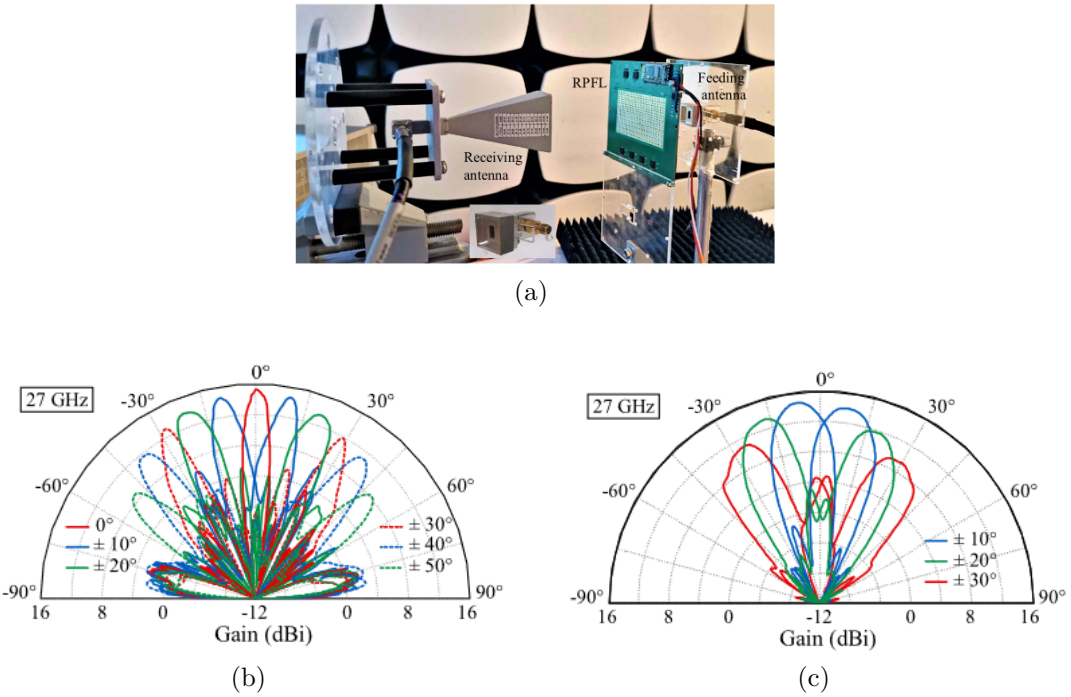


Figure 1.38 – Reconfigurable Fresnel lens at 27 GHz [68]: (a) Antenna prototype, (b) Measured radiation on H-plane, and (c) Measured radiation on E-plane

The FPMS technology (Field Programmable Microwave Substrate) that will be studied during this thesis work will allow to control of the refractive index of a lens, so this technology could be a good candidate for creating a reconfigurable lens antenna.

## 1.4 Summary and perspective

In this chapter, a non-exhaustive state-of-the-art has been done concerning reconfigurable microwave circuits and antennas. The examples mainly concern systems (circuits or antennas) with the integration of electronic devices (diodes, ..) to achieve reconfigurability. As we mentioned at the end of state-of-the-art concerning reconfigurable circuits, each example concerns one function (phase shifter, power divider, filter) that can be electronically controlled. However, it seems difficult to obtain a high level of reconfigurability, allowing one to change the functionality with one unique device, for example, to transform one power divider into a phase shifter. In the following chapters, we propose to study another solution based on FPMS (Field Programmable Microwave Substrate), allowing to change in the functionality of one circuit thanks to the reconfigurability of the FPMS (Chapter 2). In the same way, as we show in the part of state-of-the-art concerning inhomogeneous lenses, the radiation patterns reconfigurability is achieved by associating multiple sources with the lens but very rarely by modifying the index law inside the lens electronically. Our objective in Chapter 4 will be to design Mikaelian lenses with FPMS technology.

Chapter 2

# FPMS and reconfigurable circuits

## 2.1 Introduction

The Field Programmable Microwave Substrate is a concept which has been developed in 2016 [1] by Canadian research teams. It is the starting point of this thesis's work on FPMS (Field Programmable Microwave Substrates). The principle of the FPMS technology is quite simple. The FPMS can be seen as an artificial substrate, and the dielectric constant can be controlled locally; more precisely, it can be switched between positive and negative dielectric values. This property allows the realization of programmable and reconfigurable waveguides. In order to control the dielectric constant locally, the FPMS is made up of a large number of unit cells that are smaller compared to the wavelength.

In [1], two prototypes using different technologies have been developed: one with PCB technology and one using LTCC technology. The initial FPMS board is presented in Figure 2.1 and works between 1.5 and 3 GHz. This board will be referred to as the First generation of FPMS. This first prototype used a total of 256 unit cells. The schematic of

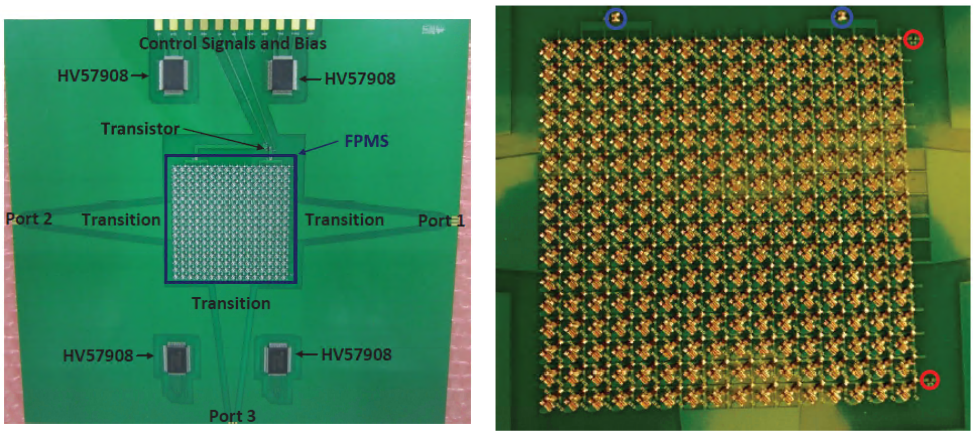


(a) (b)

Figure 2.1 – First generation FPMS board

the unit cell is presented in Figure 2.2 with the variation of dielectric constant versus the bias voltage of the varactor diode and frequency. The global board is shown in Figure 2.1, including microstrip to FPMS transitions. Depending on the bias voltage of the varactor diode, the dielectric constant of the unit cell can be controlled, and most important, at a given frequency, this dielectric constant can be switched from positive to negative values. This allows the conception of reconfigurable waveguides depending on the position and

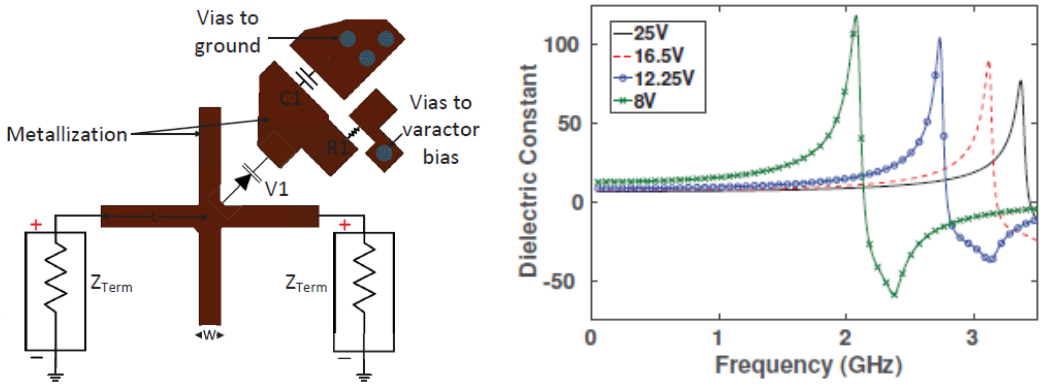


(a) (b)

Figure 2.2 – First generation Unit Cell

number of cells that are considered to have positive or negative dielectric constant. Figure 2.3 gives an example of configuration: the blue corresponds to a positive state, and the white corresponds to a negative state. This first generation of the board has been designed

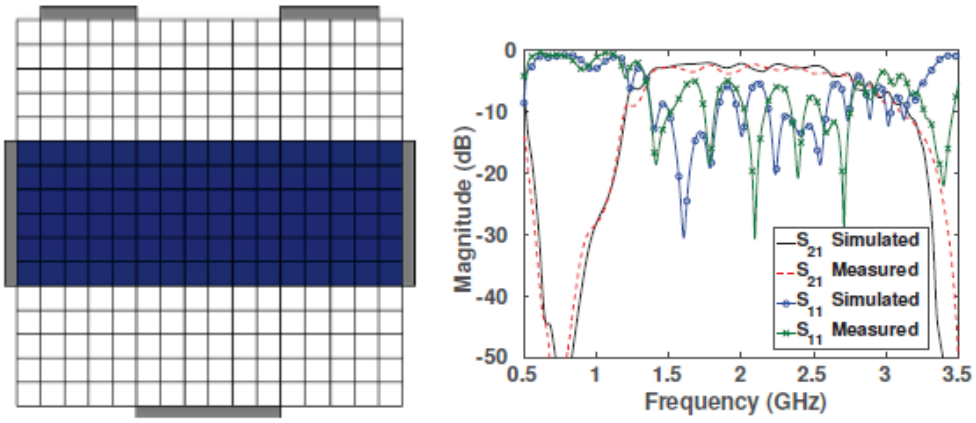


(a) (b)

Figure 2.3 – Strait waveguide configuration

to achieve waveguide configuration but also to synthesize some amplifiers and resonators thanks to the use of a transistor on the board of the FPMS. This board has also been used to synthesize reconfigurable filters with more details are given in [21].

In this chapter, we will discuss the creation of a new FPMS board that will work at a higher frequency. We want to be able to use the FPMS technology in the X-band.

First, we will introduce the theoretical circuit model of the unit cell (UC) and the algorithm used to extract the dielectric parameters of the unit cell from the simulation or measurement of S parameters. Secondly, we will study the development of a new UC that works in the X-band. This second section is the most important, as this thesis work's other circuit and antenna concepts are based on this new unit cell. The last section will present the implementation of an actual FPMS board in the X-band.

## 2.2 Theoretical studies of a unit cell

The section will focus on the FPMS Unit Cell principle and how to optimize it. The primary purpose of the FPMS technology is to create programmable waveguides. As such, the principle is to create a material for which the effective dielectric constant can be controlled and also can be switched between negative and positive dielectric values. So the Unit Cell is the fundamental element to realize this artificial substrate.

One method to analyze such kind of materials is to use an equivalent circuit method for the transmission line (Figure 2.4) [69]. This model divides the transmission line into

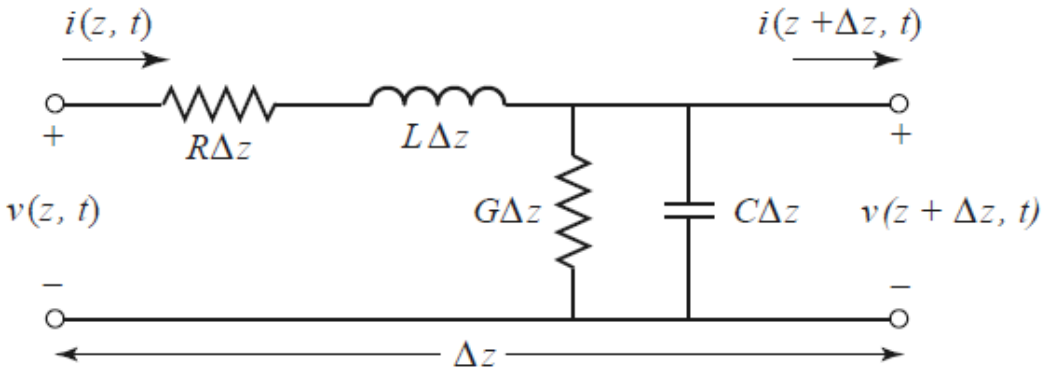


Figure 2.4 – Lumped-element circuit model of a transmission line [69]

small segments of size $\Delta z$. The serial inductance L represents the self-inductance of the two conductors, and the shunt capacitance is due to the proximity of the two conductors.

Finally, R and G are added to consider the metallic and the dielectric loss, respectively. In the case of a parallel plate transmission line, the element L, C, R, and G can be calculated using[69]:

$$L = \frac{\mu d}{w} \tag{2.1}$$

$$C = \frac{\epsilon' w}{d} \tag{2.2}$$

$$R = \frac{2R_s}{w} \tag{2.3}$$

$$G = \frac{\omega \epsilon'' w}{d} \tag{2.4}$$

$$R_s = \sqrt{\frac{\omega \mu}{2\sigma}} \tag{2.5}$$

where w is the width of the line and d is the distance between the two parallel plates.

In the case of lossless material, this equivalent circuit can be simplified. In this situation, the line is only modelized by a serial inductance (L) and a shunt capacitance (C). A perfect negative dielectric material can be represented by replacing the shunt capacitor with an inductance. So, in order to have a tunable metamaterial, the idea is to add a resonant circuit (LC) to the initial model. This resonant circuit is designed thanks to the use of a Varactor diode in our case. As such, when the shunt LC circuit is used below its self-resonance frequency, it will have a capacitance behavior, and the global circuit will have a positive dielectric constant. On the other hand, when the resonant circuit is used after its self-resonance frequency, it will act as an inductance. As such, the global circuit will have a negative dielectric constant.

In order to extract the dielectric parameters of the unit cell from the calculated S-

parameters, we used the Nicolson-Ross-Weir (NRW) algorithm [70]:

$$\Gamma = K \pm \sqrt{K^2 - 1} \tag{2.6}$$

$$K = \frac{S_{11}^2 - S_{21}^2 + 1}{2S_{11}} \tag{2.7}$$

$$T = \frac{S_{11} + S_{21} - \Gamma}{1 - (S_{11} + S_{21})\Gamma} \tag{2.8}$$

$$\frac{1}{\Lambda^2} = -\left[\frac{1}{2\pi\ell}\left(\ln\left(\frac{1}{T}\right) + i2\pi n\right)\right]^2 \tag{2.9}$$

$$\mu_r = \frac{1+\Gamma}{(1-\Gamma)\Lambda\sqrt{1/\lambda_0^2 - 1/\lambda_c^2}} \tag{2.10}$$

$$\epsilon_r = \frac{\lambda_0^2}{\mu_r\left[1/\lambda_c^2 - 1/\Lambda^2\right]} \tag{2.11}$$

where:

- $\Gamma$ is the reflection coefficient, and the correct choice of sign in Equation 2.6 is made by ensuring $|\Gamma| \leq 1$.
- $T$ is the transmission coefficient.
- $\mu_r$ is the relative permeability.
- $\epsilon_r$ is the relative permittivity.
- $S_{11}$ and $S_{21}$ are the reflection and transmission s-parameters.
- $\lambda_0$ is the free-space wavelength.
- $\lambda_c$ is the cut-off wavelength of the transmission line (depending on the transmission line case).
- $\ell$ is the length of the sample and should be less than 180 electrical degrees.
- The term $i2\pi n$ in Equation 2.9 is used to unwrap the imaginary part of $ln(1/T)$.

This algorithm permits the extraction of all parameters of interest from S parameters. The S parameters can come from multiple sources: analytic results using the transmission line model or a full wave simulation of the cell.

In this thesis, we design the UC using full-wave simulation software. The simulation of the UC is performed by exciting it with a plane wave. To do this, the unit cell is exited by a parallel plate waveguide that consists of two perfect electric conductors on the top and the bottom and a perfect magnetic conductor on the sides. The simulation design is shown in Figure 2.5. The S-parameters from these simulations are used in the NRW algorithm to calculate the effective material properties.

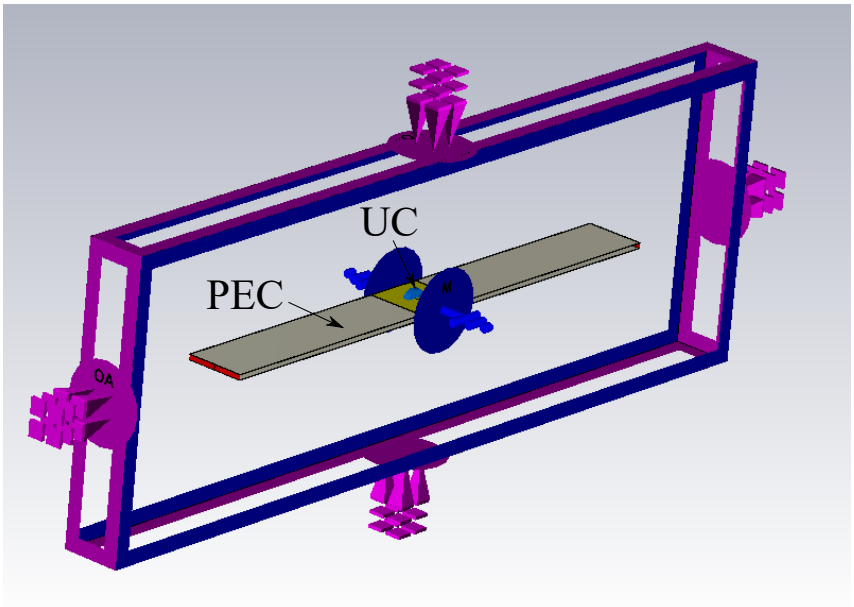


Figure 2.5 – Simulation of a UC

To explain the behavior of the UC, Figure 2.6 shows the relative dielectric constant that can be obtained for a standard UC. The dielectric response can be separated into four areas.

$f \ll f_r$ The first one appears before the system's resonant frequency. In this area, the cell acts mostly as a standard dielectric material: stable positive permittivity and permeability over frequency.

$f = fr$ The second one appears near the resonant frequency. In this area, the cell mostly works as an absorber.

$f_r < f < f_c$ The third one appears after the resonant frequency. In this area, the cell is mostly a reflective structure, and the relative dielectric constant is negative.

$f > f_c$ The cell has a positive permittivity and permeability in this last area.

For the FPMS concept, the two most important areas are the first and the third ones. The system's resonant frequency can be controlled thanks to the tunable LC circuit (with a varactor diode). As such, if the working frequency is fixed, depending on the resonant frequency, the unit cell can go from being used in the first area or in the third one. It allows multiple UC systems to have positive and negative dielectric values at the same frequency. Area 2 needs to be avoided as it is very lossy.

The last area, 4, has an interesting property: a high refractive index variation. This property will mainly be used in Chapter 4 for lens applications.

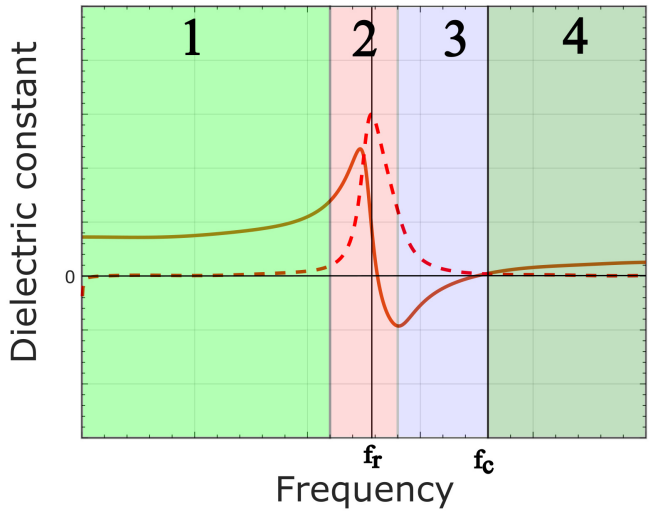


Figure 2.6 – Dielectric response of a UC, real part (solid line) and imaginary part (dotted line)

## 2.3 New unit cell in X band

During the design process, multiple parameters need to be controlled. We focus the studies on two states of the UC: the positive state, where the cell is used below its resonant frequency (area 1), achieving a positive dielectric constant, and the negative state, where the cell is used after the resonant frequency (area 3) achieving a negative dielectric constant. Now, we consider that the positive state is achieved when the capacitance of the varactor used is the smallest and for the negative state when the capacitance of the varactor is the highest.

For the positive state, we focus on having the minimum variation of the artificial dielectric constant and having it as close as possible to the dielectric constant of the host material (Dielectric substrate where the UC are printed and varactor diodes are mounted). This last property will facilitate the integration of the FPMS structure. For the negative state, we will focus on obtaining the maximum bandwidth where the UC has a negative dielectric constant. We will also look at the value of the resonant frequency of the two states (depending on the capacitance value). The resonant frequency of the positive state should be at maximum as possible, and the distance between the two resonant frequencies should be maximized. We also look at the magnetic constant that should remain as close as possible to 1 for the positive state.

### 2.3.1 Varactor diode

A varactor diode is a particular type of diode that allows the production of a junction capacitance ($C_j$) which varies with bias voltage. Due to this property, varactor diodes are used in numerous applications like phase shifters, for example [71]. Figure 2.7 gives an equivalent model of a varactor diode. The junction capacitance is given by :

$$C_j(V) = \frac{C_0}{(1 - V/V_0)^\gamma} \tag{2.12}$$

where $C_0$ is the junction capacitance with no bias; $V_0$ and $\gamma$ depend on the diode's type and fabrication process, and $V$ is the applied bias voltage. In the equivalent circuit, $R_s$ is the serial resistor. $L_s$ and $C_p$ are parasitic elements that come from the diode package.

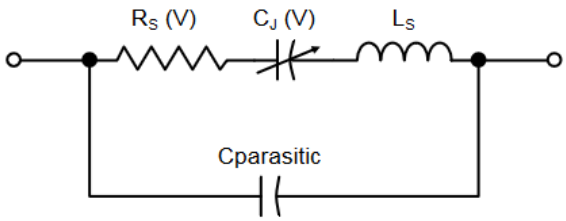


Figure 2.7 – Varactor diode equivalent circuit

In order to choose the "best" varactor diode for the design of an FPMS and, more precisely, of the Unit Cell, we look at the different characteristics of the diode. The most critical parameters are the possible value and the variation range of the junction capacitance; the junction capacitance value combined with the parasitic reactance of the package will define the working frequency of the FPMS. The variation range of the capacitance needs to be maximized to improve the reconfigurability of the Unit Cell. The last thing to look at is the serial resistance that should be minimized in order to limit the loss of the FPMS.

In the first generation of FPMS, the diode that was used was the MACOM BB 833 E6327. The capacitance can vary from 12 pF (0 V) to 0.75 pF (25 V), the parasitic inductance is 1.8 nH and the serial resistor is 1.8 Ω. This diode was chosen to create a FPMS at 2 GHz.

In order to increase the working frequency, one logical step is to change the diode. The first choice was to use a MA46580-1209 MACOM varactor diode. This diode has been characterised in [71], and all parameters are known: the parasitic inductance is

$L_s = 0.108\,\text{nH}$, the serial resistance at 0V is $Rs = 2.2\,\Omega$ and $V_0$ and $\gamma$ have both been estimated to respectively 5.755 V and 1.96, allowing a direct used of the equation 2.12. The capacitance of this diode varies from 1.56 pF to 0.17 pF. The 0.17 pF is achieved for a voltage of 12 V. This capacitance value, combined with the parasitic inductance, gives the diode a high self-resonance frequency.

The problem with this diode, other than the relatively high serial resistance, is that this diode has been depreciated and is no longer available. Therefore, as a part of the studies developed around this diode, we tried to find a diode with equivalent parameters. In the end, the chosen diode is the macom MAVR-000120-1141, the capacitance of this new diode varies between 1.1 pF and 0.14 pF. The serial resistance is estimated to be $0.88\,\Omega$, and the parasitic inductance is unknown, but it can be assessed that it should be at the same level as the previous diode.

The diode will be simulated using the equivalent model (figure 2.7) without considering the parasitic capacitance for all the simulations presented in this thesis. We will use the parameters of the MACOM MAVR-000120-1141 diode for all simulations except for the first part of Chapter 3. In this precise chapter, the old Macom MA46580-1209 is used.

### 2.3.2 Design of the Unit Cell

In order to increase the operating frequency of the FPMS technology, we already discussed the change of the Varactor diode. However, now, we also have to modify the design of the Unit cell. In the first generation of FPMS, the design was based on two perpendicular crossed lines printed on a FR4 substrate. This structure is presented in Figure 2.2. In order to increase the working frequency of the cell, the best way is to reduce the size of the UC. From the previous work, the cell must be less than a quarter of the wavelength. The problem with the first generation of FPMS is that a significant part of the cell's surface is taken to achieve the DC biasing of the cell. So in order to fully study the UC, we will first use a simplified design of the UC called "Basic UC" that does not include the DC biasing of the cell. And from this Basic UC, we will develop an extension that will consider the DC biasing. Also, the new UC will use a better substrate with less loss and lower dielectric constant (Rogers 5880, $\epsilon_r = 2.2$, $tan\delta = 0.0009$). The lower dielectric constant will help with the size problem because $\lambda_g$ depends on the dielectric constant. This will help achieve the size condition to implement the total cell with DC bias and varactor diodes.

#### 2.3.2.1 Basic Unit Cell

The basic unit cell consists of a square parallel plate waveguide where the top plate is connected to the ground through a via and the varactor diode. Figure 2.8 presents the unit cell schematic with the different parameters.

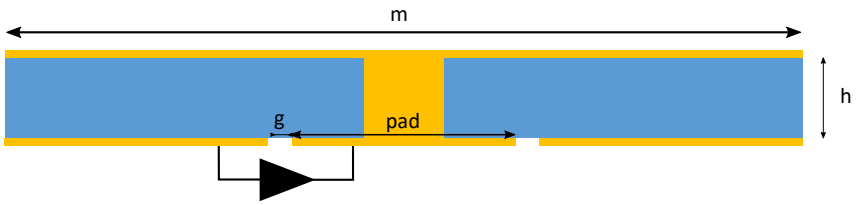


Figure 2.8 – Schema "Basic" unit cell

Studies were done for the different parameters (m, gap, pad, h), for both extreme values of the varactor diode capacitance ($C = 1.1\,\text{pF}$ and $C = 0.14\,\text{pF}$), in order to obtain the highest working frequency for the UC. These studies are highlighted in Figure 2.9 and 2.10.

The basic values of the UC are: $m = 2.5\,\text{mm}$, $gap = 0.1\,\text{mm}$, $pad = 0.5\,\text{mm}$, $h = 0.127\,\text{mm}$. For each curve presented in Figure 2.9 and 2.10, only one parameter varies while the others are equal to the basic values. It can be seen that in order to increase the working frequency, the best way is to minimize all the parameters. However, all parameters do not have the same impact: the size of the UC, the size of the pad, and the gap can be reduced freely; the only limitation would be the fabrication constraint. Nevertheless, the height of the substrate needs to be chosen carefully. Indeed, decreasing the height has some other effects: reducing the bandwidth when the dielectric constant of the cell is negative and reducing the relative dielectric constant in the positive state of the cell ($C = 0.14\,\text{pF}$). Of course, the first effect is unwanted. However, the second can be beneficial, as the closer the artificial dielectric made of cells would be to the dielectric of the primary material, the easier the integration and the impedance matching would be. The magnetic constant can also be monitored (figure 2.10). The two parameters impacting the most the variation of the magnetic constant are the gap size and pad size. As mentioned before, the magnetic constant should be as much as possible, close to 1. Thankfully this condition leads to the same conclusion: the size of the gap and the pad should be minimized. However, it can be interesting to notice that the parameters that affect the dielectric constant do not affect much the magnetic constant and vice versa. It means that a specific combination could be achieved depending on the application.

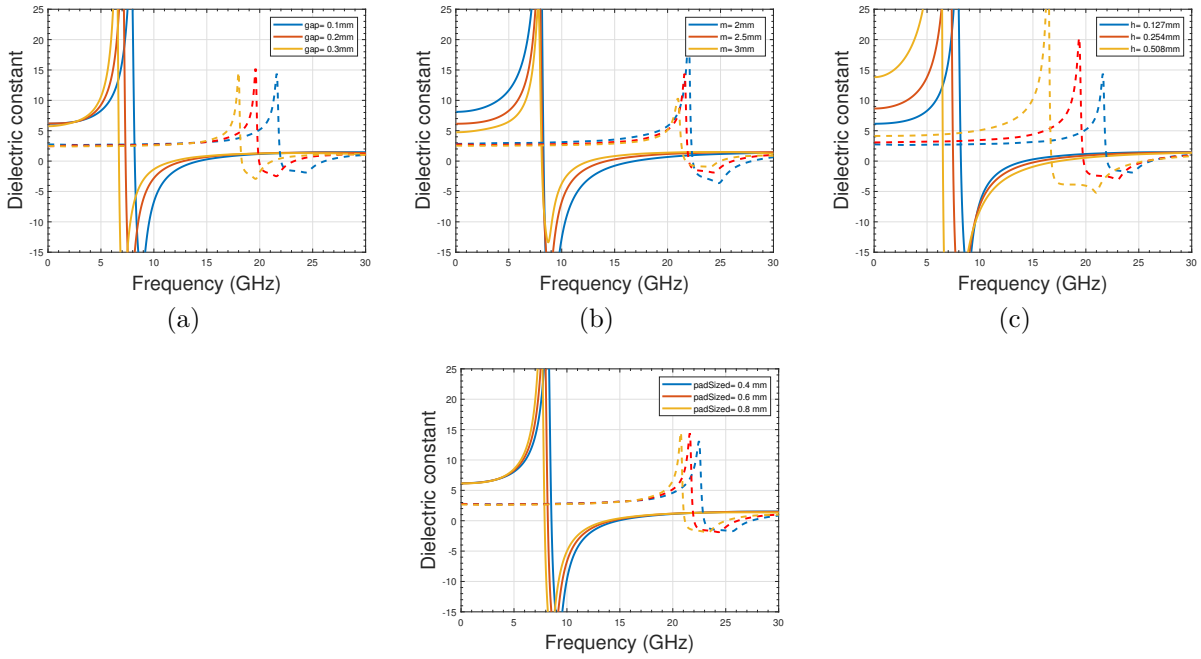


Figure 2.9 – Dielectric constant for C= 1.1pF (solid line) and 0.14pF (dashed line): (a) gap, (b) UC size, (c) Substrate thickness, and (d) Pad size

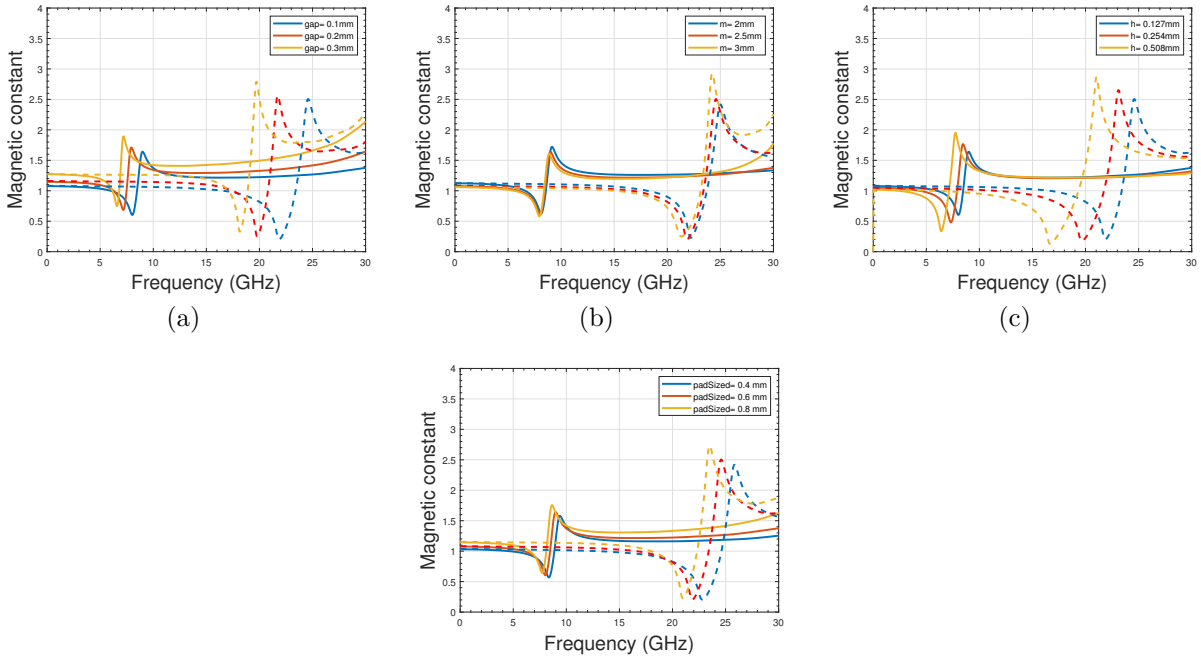


Figure 2.10 – Magnetic constant for C= 1.1pF (solid line) and 0.14pF (dashed line): (a) gap, (b) UC size, (c) Substrate thickness, and (d) Pad size

The diameter of the via also has an impact on the performance of the UC. The bigger the diameter is, the higher will be the resonant frequency. But if we want to increase the diameter of the via, it also needs to increase the pad's size, which will induce a decrease in working frequency as shown in Figure 2.9.

Figure 2.11 presents the extracted dielectric parameters, magnetic constant, and refractive index of the basic unit cell thanks to the Nicolson-Ross-Weir (NRW) algorithm for the final dimensions with $m = 2.5\,\text{mm}$, $gap = 0.1\,\text{mm}$, $pad = 0.7\,\text{mm}$, $h = 0.127\,\text{mm}$ and for three different values of capacitance. The chosen dimensions are the final compromise between the performance of the cell and the fabrication constraint (limitations of the size of the gap and the pad for the PCB etching process) with the chosen diode.

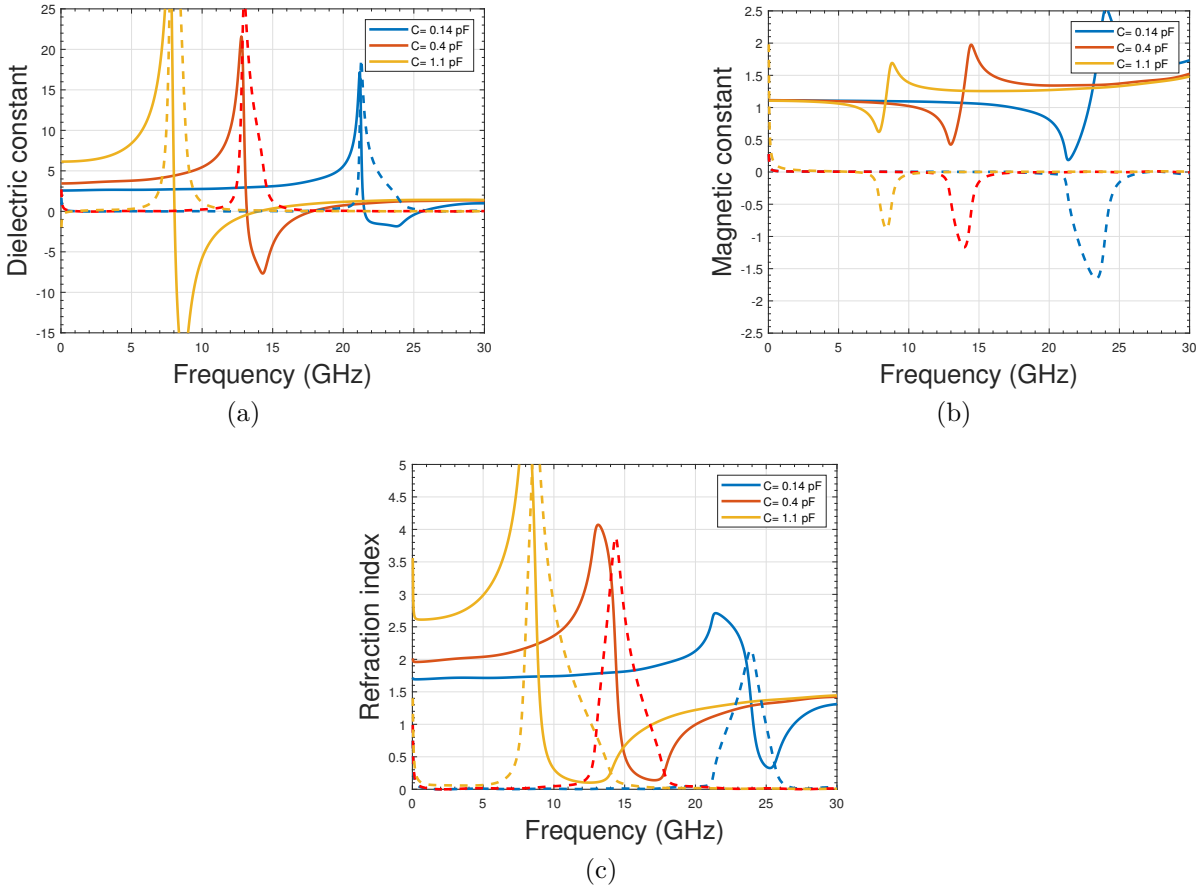


Figure 2.11 – UC parameters

This "basic cell" does not take into account any DC Bias and isolation. This version of the cell will be used for an antenna application in chapter 3 because, for this precise case, independent biasing is not necessary. Nevertheless, for a reconfigurable FPMS system

with several cells, we have to bias each cell individually to control the effective dielectric parameters, so a decoupling between cells is required. Therefore, the final version of the unit cell is presented in the next section.

#### 2.3.2.2 Complete Unit Cell

As the last part mentions, the "Basic cell" does not integrate any DC biasing or decoupling aspect. In order to create a reconfigurable structure, the ability to control each UC independently is needed. To full fill this objective, two problems need to be addressed. Firstly, each cell must have a complete DC biasing and a DC/RF decoupling. Secondly, each unit cell must be isolated from a DC point of view from the other cells. The simplest way to achieve the second point is to separate each cell and connect it through a high enough capacitance to its neighbors. The problem here is to optimize the capacitance. Also, this solution does not address the DC biasing aspect.


(a) (b)

Figure 2.12 – Schematics of the complete Unit-Cell in X band

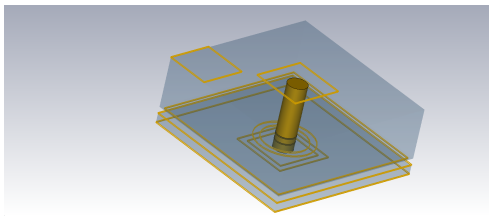

Figure 2.13 – Schematics of the complete Unit-Cell in X band

In order to achieve DC biasing and decoupling, we use a multilayer PCB printed technology. Figures 2.12 and 2.13 propose the final approach of the UC with the DC decoupling. It is composed of four metallic layers and three dielectric ones. A via hole goes through the multilayer structure to bias the Varactor diode placed on the structure's bottom layer. In addition, some annular slots are engraved in the first and third metallic layers, and the reduced size of the second layer allows for isolating the cells relative to

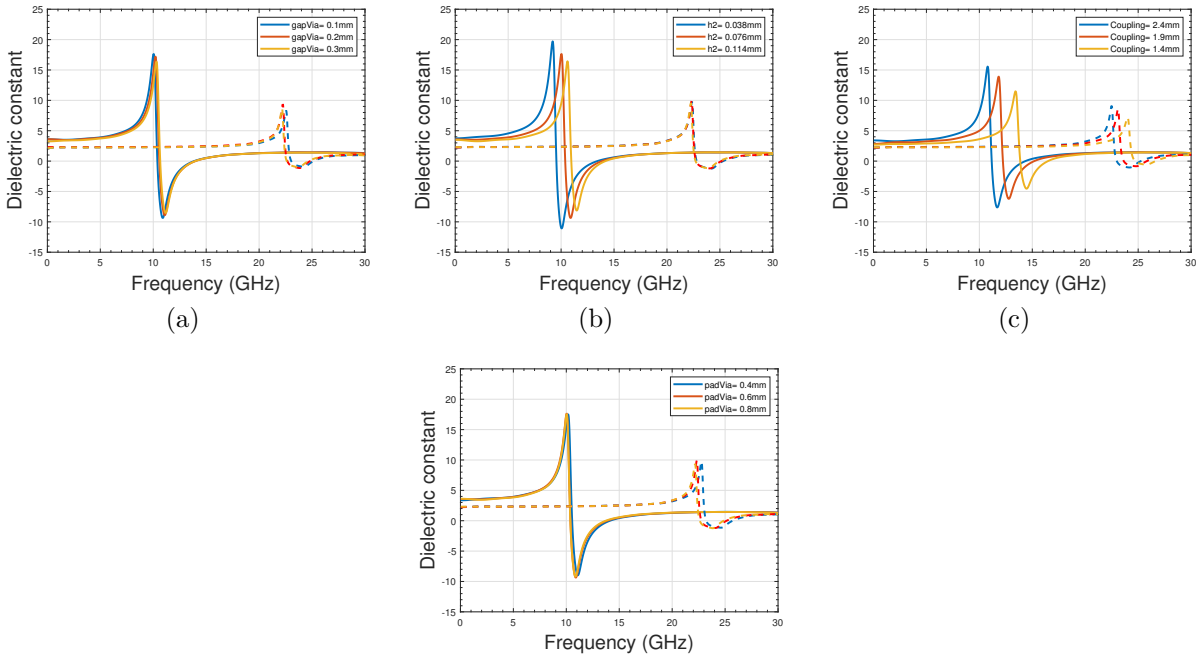


(a) (b) (c) (d)

Figure 2.14 – Dielectric constant C= 1.1pF (solid line) and 0.14pF (dashed line): (a) Second gap, (b) Thickness of the second substrate, (c) Coupling capacitor size and (d) Second pad size

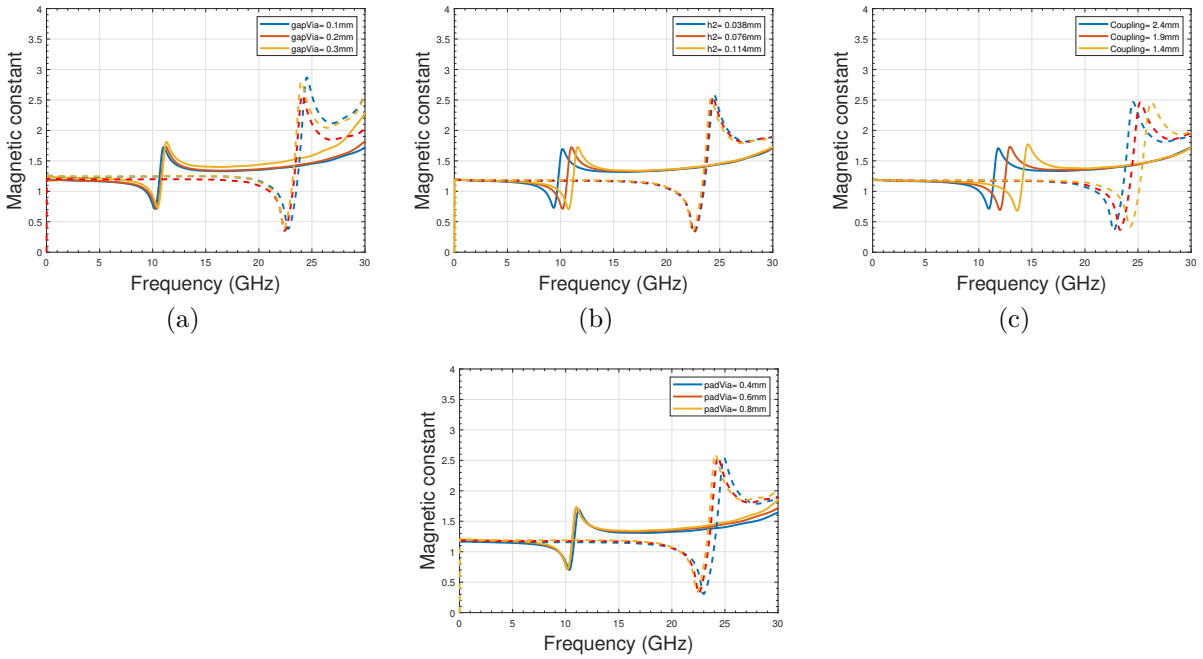


(a) (b) (c) (d)

Figure 2.15 – Magnetic constant $C = 1.1\,\text{pF}$ (solid line) and $C = 0.14\,\text{pF}$ (dashed line): (a) Second gap, (b) Thickness of glue, (c) Coupling capacitor size and (d) Second pad size

each other in order to be able to control each UC independently for the FPMS global concept. The only difference between the two concepts presented in Figure 2.12 (a) and Figure 2.12 (b) is that the two middle metallic layers are inverted. Version (a) is the most logical one, as it is a direct evolution of the basic cell. The basic cell is placed inside a parallel plate waveguide. The only drawback of this solution is that this design can not be integrated easily with other printed technology. For example, in order to feed the structure, both metallic layers 2 and 4 need to be accessible. However, due to the proposed stack-up for case (a), there are both in different dielectric layers, so layer 2 is not easily accessible. This problem is corrected in the second proposed design (b). In this design, the two metallic layers of the parallel plate waveguide are on the same dielectric layer.

Compared to the "Basic cell," the use of multilayer technology with the addition of new layers (top levels) increases the number of parameters. But most of the new parameters do not have a significant impact. For example, the height of the top substrate has totally no effect; it allows only the separation of the DC biasing layer from the active part of the UC and saves space for the implementation. The second gap (gapvia) and the second pad size (padvia) have limited effect as represented in Figure 2.14 (a and d). The only parameters that still have to be looked closely are the height of the "glue" ($h2$, red color on the designs) and the size of the "coupling capacitor" as it is shown in Figure 2.14 (b and c). The thickness of the "glue" is an interesting parameter as it impacts only the negative state of the cell. Decreasing the thickness increases the bandwidth of the negative state of the cell; as such, it should be minimized at maximum. For the final manufactured prototype, we chose the intermediate value as proposed by the manufacturer. The "coupling capacitor" size could be used to increase the resonant frequency further. But again, this comes with some trade-off, as increasing the resonant frequency comes with a reduction of the bandwidth of the negative state. The impact of all these parameters on the permeability is also shown in Figure 2.15 with the same conclusions.

Figure 2.16 shows a comparison of results between the basic cell and the final cell. The final cell has a higher resonant frequency alongside a lower dielectric constant. But this change comes with some drawbacks: bandwidth reduction for the negative state and increase of the magnetic constant.

Figure 2.17 shows the final cell's extracted parameters for different capacitance values. The positive state ($C = 0.14\,\mathrm{pF}$) shows a dielectric constant of around 2.4, and a magnetic constant of around 1.18 at 12 GHz. For the negative state ($C = 1.1\,\mathrm{pF}$) the dielectric

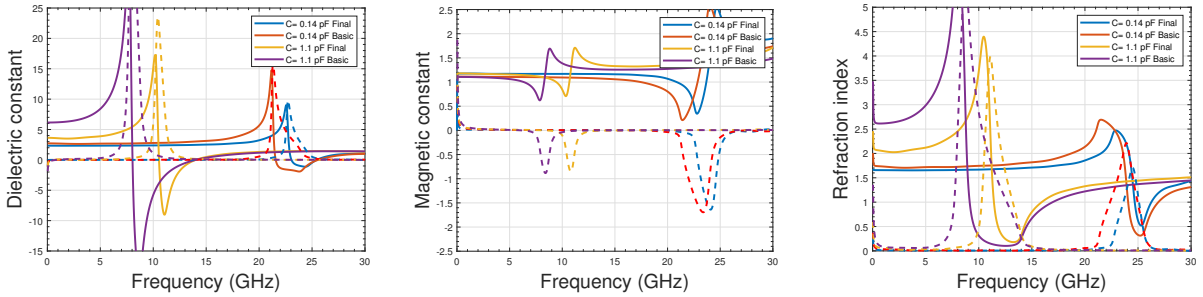


(a) (b) (c)

Figure 2.16 – Comparison between Basic and complete UC for real part (solid line) and imaginary part (dashed line)

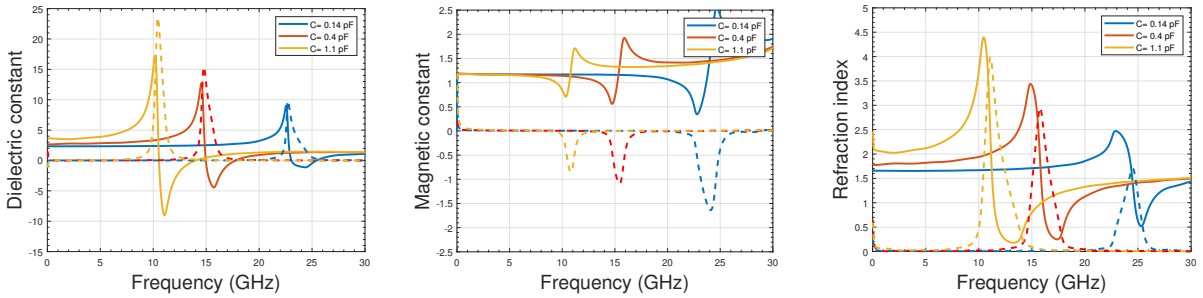


(a) (b) (c)

Figure 2.17 – Complet UC for 3 values of capacitance with real part (solid line) and imaginary part (dashed line)

constant is negative between 10.5 GHz and 14 GHz.

In the end, the most critical design parameters are the height of the substrate ($h1$), the size of the cell, and the size of the coupling capacitance. Of course, the other parameters have their importance, but in the end, the dimensions are tied to the fabrication constraint.

### 2.3.3 Equivalent model

In the FPMS concept, the number of UC can be important. For now, the present UC has been simulated with a Full wave approach using CST. Full wave simulations have the main advantage of providing accurate results that consider all design parameters, but they are time-consuming, especially for large structures. So it can be useful to find an equivalent circuit model of the UC to limit the time consumed during the simulation of global FPMS.

The schematic of the equivalent model is presented in Figure 2.18. The idea of the

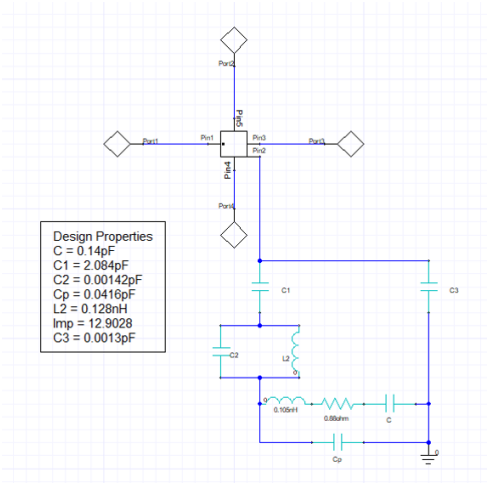


Figure 2.18 – Equivalent model of the UC

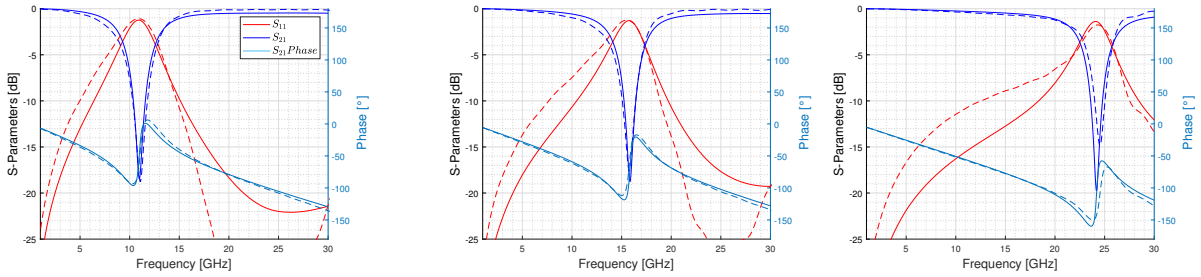


(a) (b) (c)

Figure 2.19 – Comparison between full wave simulation (dashed line) and equivalent model (solid line) of the UC, for (a) $C = 1.1\,\text{pF}$, (b) $C = 0.4\,\text{pF}$ and (c) $C = 0.14\,\text{pF}$

equivalent model is to simulate a parallel plate waveguide (co-simulation EM/Circuits) with the unit cell's dimensions and five connected ports. Four of these ports are connected to neighboring cells, and the fifth one allows the addition of the varactor diode and parasitic elements. The different capacitance and inductance added to the diode's equivalent model are tuned to achieve an equivalent S-parameters response between the equivalent model and the Full-wave simulation of the cell. The "best" matching between the two sets of data is presented in Figure 2.19 with the values of the different capacitance and inductance indicated in Figure 2.18.

It is essential to note that this model has been given to XLIM laboratory (partner of the ANR/NSERC project) to be used in their optimization algorithm to design reconfigurable filters with the new global FPMS presented in the next section.

## 2.4 FPMS in X band

This section focuses on the presentation of the complete FPMS board. We keep the 16 by 16 configuration of the first board as the Canadian research teams designed because it provides a good compromise between the size/number of cells and reconfigurability.

By considering the 2.5 mm square UC presented previously, the total size of the FPMS is 40 mm by 40 mm. It corresponds to 2 $\lambda$g at 10 GHz with a dielectric constant of 2.2. Of course, the final board will be larger than this dimension because we need to add the printed feeding part with an optimized microstrip to the FPMS transition. This transition will be presented in 2.4.3.2.

In the next sections, we discuss different simple designs to present the reconfigurability capability of this new board in the X-band.

### 2.4.1 Waveguide configuration

In this section, different configurations are presented to illustrate the FPMS's reconfigurability.

In order to create a reconfigurable waveguide with the FPMS, we need to use it at one frequency for which we can have positive and negative dielectric constants for the UC depending on the applied Bias voltage for the varactor diode.

#### 2.4.1.1 Strait waveguide

Figure 2.20a shows the first configuration (Full-wave simulation) for which the red color represents the unit cells that are set to be positive ($C = C_p$) and the blue ones that are set to be negative ($C = C_n$).

Figure 2.20b shows the S-parameters of this configuration for which the values of the capacitance are set to both extreme values ($C_p = 0.14$ pF and $C_n = 1.1$ pF). Thanks to the analysis of the UC (see Figure 2.17), we can estimate the working frequency of the created waveguide:

— The resonant frequency of the negative cell ($C_n$) will determine the lower cut-off frequency.

— The resonant frequency of the positive cell will determine the upper cut-off frequency.

— The bandwidth of the negative cell (when the dielectric constant is negative) should correspond to the final bandwidth of the waveguide.

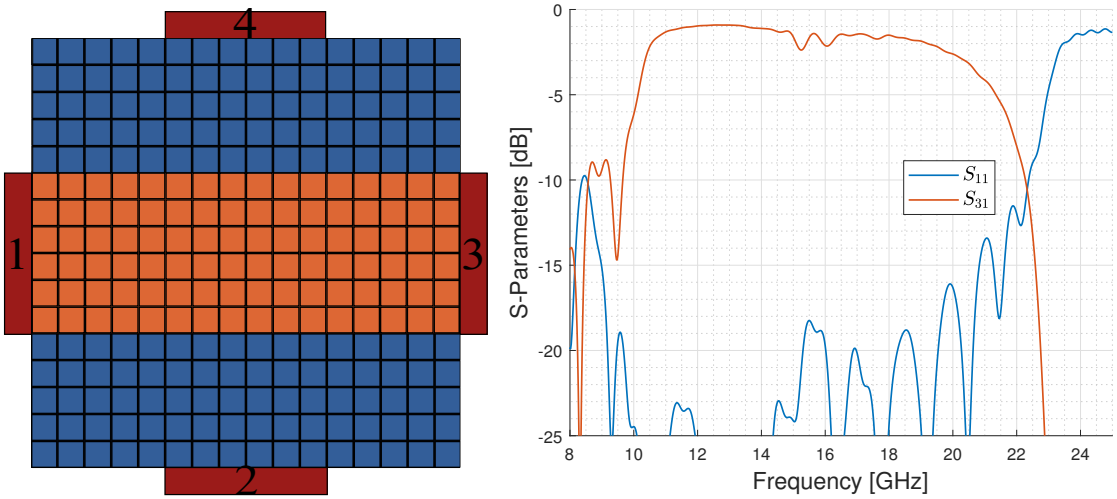


(a) Configuration schematic (b) S-parameters

Figure 2.20 – Strait waveguide configuration

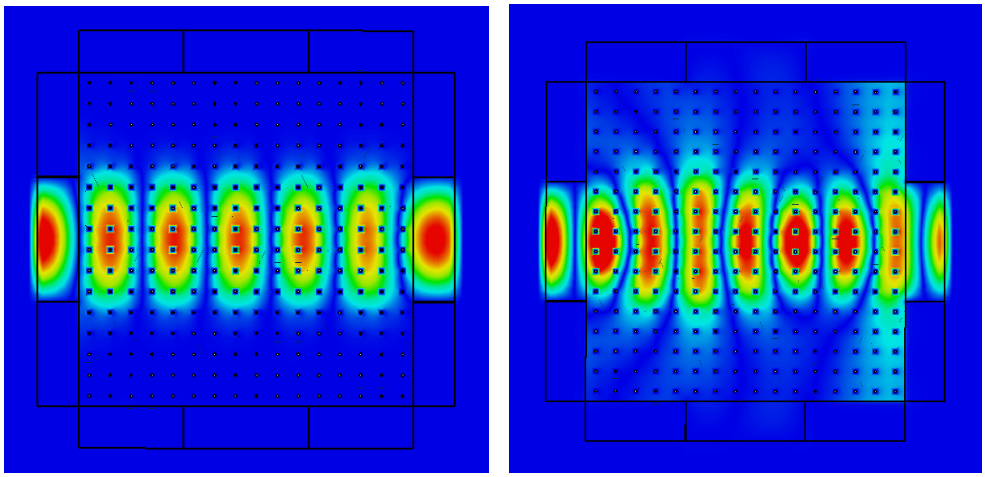

(a) 12.5GHz (b) 15GHz

Figure 2.21 – Electric field inside the FPMS for z=0.05mm

In this configuration, the resonant frequency of the negative and positive cells are respectively 10.5 GHz and 22.75 GHz. The negative cell is purely negative between 10.5 GHz and 14 GHz so the waveguide should work between 10.5 GHz and 14 GHz. It can be observed from the S-parameters (figure 2.20b) that the bandwidth is bigger than expected. The fact is after 14GHz, the dielectric constant of the negative cell becomes positive, but it remains highly different from the dielectric constant of the positive cell. Therefore the field remains mostly confined in the positive cell. This effect can be observed on the

electric field shown in Figure 2.21a. At 12.5GHz, it can be seen that the electric field is confined inside the artificial waveguide, but at 15 GHz, a part of the electric field leaks inside the "negative" cell. The observation of the field can also be used to confirm that the mode that propagates inside the waveguide is a classical $TE_{01}$ mode.

This configuration can be used to study the performance of the FPMS and, more precisely, the loss of the system. At 12.5 GHz, the total loss are equal to 0.91 dB. In comparison, a microstrip line of the same length (4cm) on the same substrate would have 0.35 dB of loss. The loss of the FPMS can be explained in four different ways: the dielectric loss, the metallic loss, the radiating loss, and the lumped element loss. The majority of the loss comes from the metallic loss and the lumped element loss. The metallic loss mainly comes from the low height of the substrate used. The diode internal resistor is one of the most important sources of loss in the FPMS concept.

Figure 2.22 shows different S-parameter results when the value of the positive Cell and negative Cell are modified. The effect of this change can easily be explained: by increasing the voltage of the negative cell (reducing the capacitance value), it increases the lower cut-off frequency, and by reducing the voltage of the positive unit-Cell, it decreases the upper cut-off frequency. So with this simple configuration without modifying the topology, basic bandpass filters can be synthesized with reconfigurability capability.

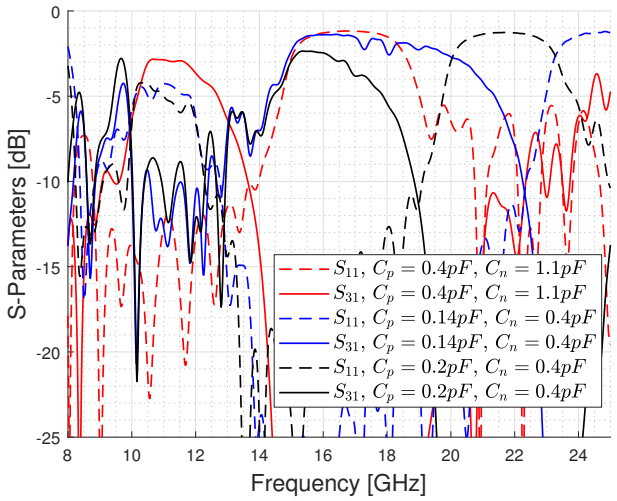


Figure 2.22 – S-parameters for different values of capacitance

Playing with the value of the capacitance of the positive cell has another impact illustrated in the table 2.1. By changing it, the effective value of the dielectric constant is modified, implying that the propagation constant of the FPMS can be controlled, and

so the phase can be changed. That means that using the strait waveguide configuration, we are able to design a simple phase shifter. At 12GHz, the phase shift can go from 106° to −152°. Nevertheless, there is a drawback to this simple technique. Indeed, using

| $C_p(pF)$ | $S_{21}(dB)$ | $Phase(\deg)$ |
|---|---|---|
| 0.14 | -0.96 | 106 |
| 0.21 | -1.2 | 57 |
| 0.27 | -1.7 | -0.2 |
| 0.34 | -2.3 | -68 |
| 0.4 | -3.8 | -152 |

Table 2.1 – Waveguide performance depending on the value of $C_p$ at 12GHz for $C_n = 1.1\,\text{pF}$

a higher capacitance for the positive cell increases the loss of the system. In order to design efficient filters or phase shifters with the FPMS technology, the idea is to use the reconfigurability topology of the FPMS board by optimizing the placement of the positive and negative cells in the configuration. The main advantage of the reconfigurable FPMS is to choose the state of any Unit Cell individually. Some examples of this approach are presented in [21] for the first generation of FPMS.

The last thing that has been tested with this topology is to use it at a higher frequency. For now, we have the frequency limit of the FPMS, which mainly depends on two factors, the resonant frequencies of the negative and positive cells, when they are set to the extreme capacitance values ($C = 1.1\,\text{pF}$ for the negative cell and $C = 0.14\,\text{pF}$ for the positive one).

However, if we look the Figure 2.17, it is easy to see that the original positive cell ($C = 0.14\,\text{pF}$) becomes negative for frequency close to 23-25 GHz and the original negative cell is positive at the same frequency. That means we can use the FPMS at higher frequencies with an inverted behavior for the cells.

This is demonstrated in Figure 2.23. It proves that the FPMS technology with this dimension could be used at higher frequency even if the system is imperfect with more loss and degraded matching ($-10\,\text{dB}$).

#### 2.4.1.2 Corner waveguide

Figure 2.24a shows the corner waveguide configuration. The main goal of this configuration is to direct the signal from port 1 to port 2. The red corresponds to positive cells, and the blue corresponds to negative cells. This configuration demonstrates the rooting capability of the FPMS, which depends on the position of positive and negative cells.

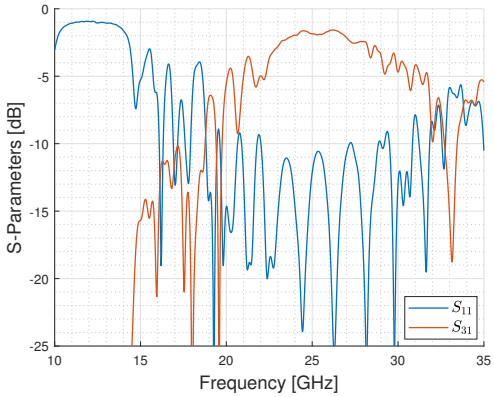


Figure 2.23 – S-parameters for $C_p = 1.1pF$ and $C_n = 0.14pF$

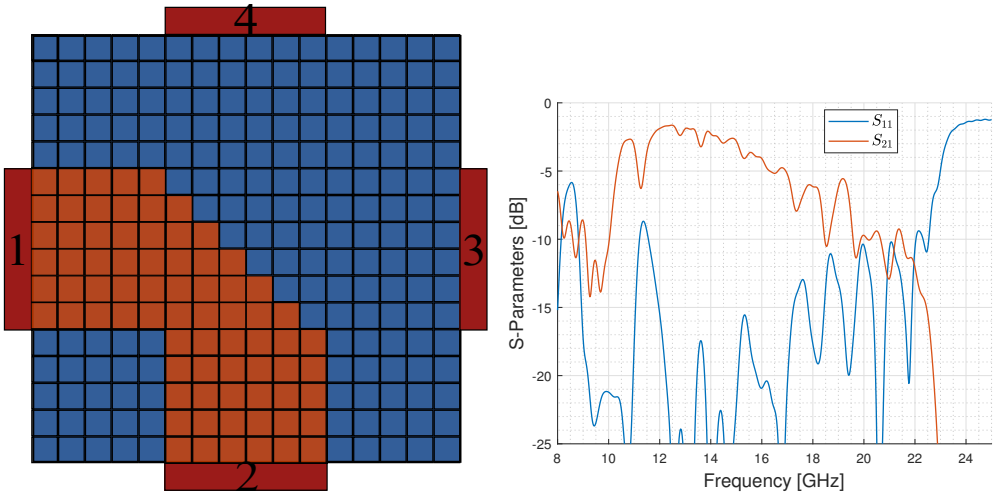


(a) Configuration schematic (b) S-parameters

Figure 2.24 – First corner waveguide configuration

Figure 2.24b shows the performance of this configuration in terms of S-parameters (matching and loss). It can be seen that the main part of the power is going from port 1 to 2 (magnitude of $S_{21}$) between 12 GHz and 14 GHz. The effect of none perfect negative dielectric value can be observed more easily, as the transmission coefficient decreases rapidly after 14GHz when the negative cell is not negative anymore. Also, it can be observed around 11.3 GHz a drop in the transmitted power alongside a degradation of the reflection coefficient ($S_{11}$). This drop seems to depend on the topography of the corner. So it can be reduced/moved by modifying the configuration as presented in Figure 2.25, for which the first drop now appears at 12.4 GHz.

The loss is more important than in the straight configuration. We have now 1.64 dB

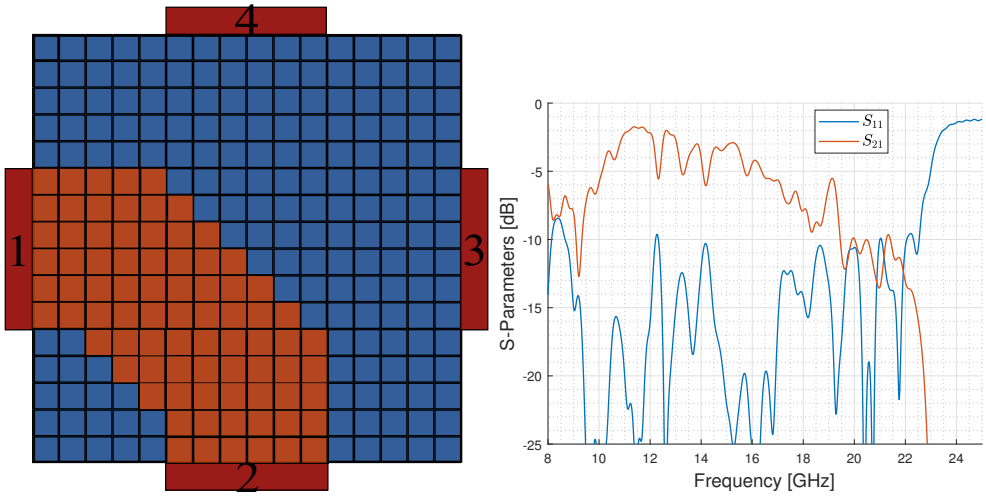


(a) Configuration schematic (b) S-parameters

Figure 2.25 – Second corner waveguide configuration

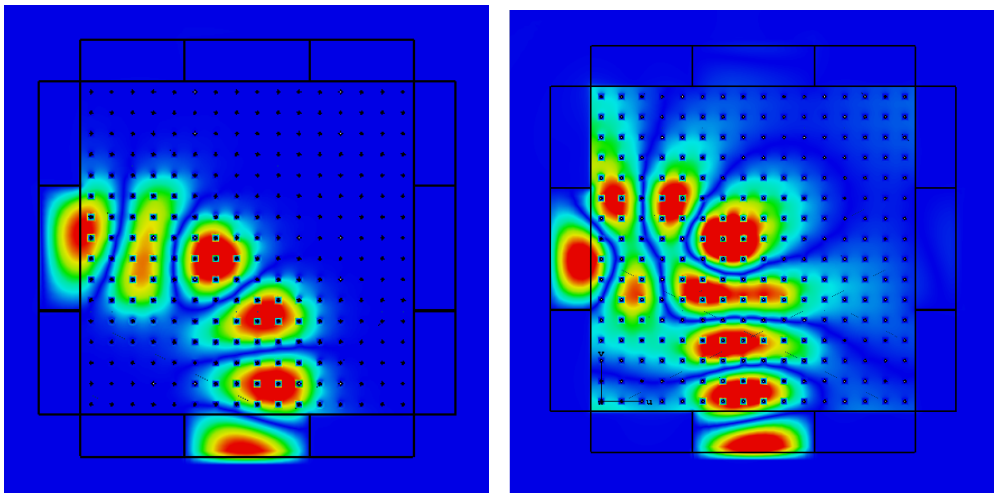

(a) 12.5 GHz (b) 15 GHz

Figure 2.26 – Electric field inside the FPMS for z=0.05mm

of total loss at 12.5 GHz. In fact, due to the configuration forcing the signal to not take the shortest pass with the modification of waveguide direction, the electric field tries to penetrate the negative cell (not a perfect conductor).

Figure 2.26a shows the electric field inside the corner waveguide at 12.5 GHz. As expected, the field follows the path of the positive cell and remains confined inside it. And when we look at the field at a higher frequency when the cell is no more negative, a part of the electric field goes inside the negative cell. Since the path is not the straight

one, the degradation of the performance after the threshold frequency is more important than in the straight configuration (Figure 2.26b).

#### 2.4.1.3 Divider

This section discusses the realization of dividers with the FPMS. Fig 2.27 presents the topology and the performance of an example of a Tee junction divider. The divider presented is composed of two symmetric corner waveguide configurations (2.24a). This configuration works as intended and equally splits the signal between ports 2 and 4. Both $S_{21}$ and $S_{41}$ are around $-5\,\mathrm{dB}$. The result is close to the expected one, as the corner waveguide alone shows a transmission of around $-2\,\mathrm{dB}$.

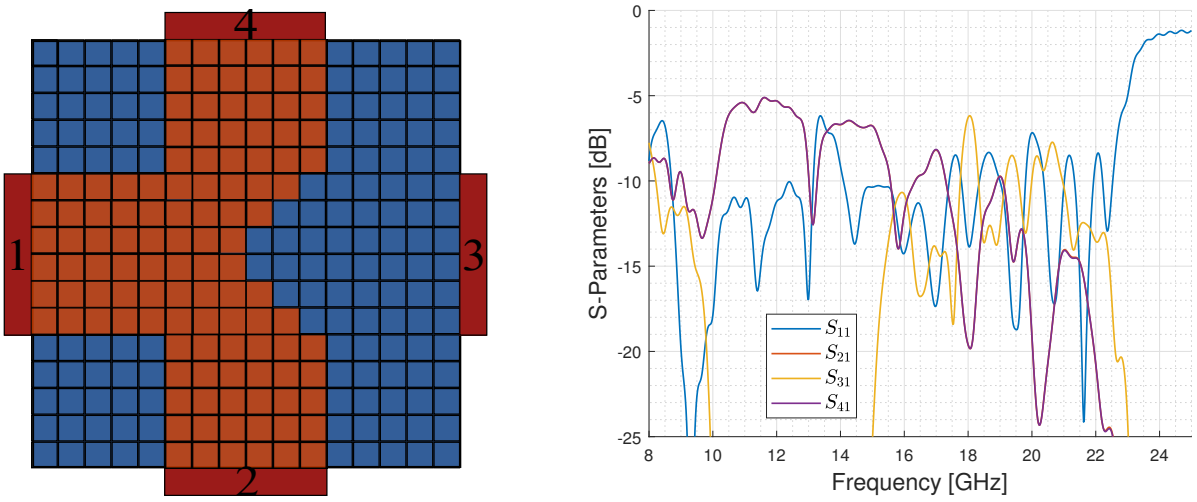


(a) (b)

Figure 2.27 – Power divider (a) configuration and (b) S-parameters

### 2.4.2 Equivalent model

For now, all previous results for the FPMS are simulated with CST, which is a Full wave software. Thus, the simulation takes time and limits the number of configurations that can be tested. However, as mentioned in Section 2.3.3, an equivalent model of the unit cell and the FPMS can be useful. We already designed and presented an equivalent model of the UC, so in order to have the equivalent model of the FPMS, we just need to interconnect 256 UC together. Figure 2.28 illustrates this principle of FPMS based on the unit cell equivalent model.

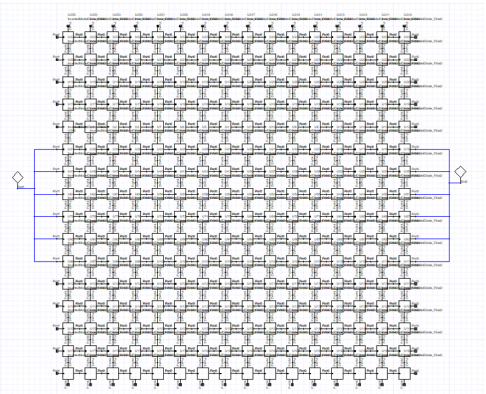

Figure 2.28 – FPMS simulated with Unit cell equivalent model

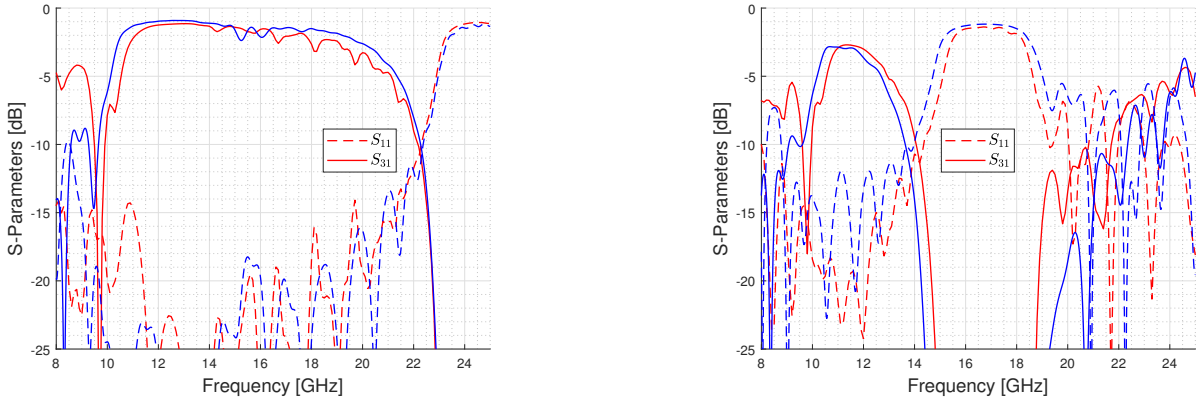


Figure 2.29 – Comparison between Full wave (blue) and equivalent model (red) simulation for straight waveguide configuration: (a) Cn=1.1pF, Cp= 0.14pF and (b) Cn=1.1pF and Cp= 0.4pF

Now we compare the results for the FPMS with the equivalent model to some results of the Full-wave simulation of the FPMS. Figure 2.29 shows the comparison between the two for the straight waveguide configuration. It can be seen that a good agreement between the two simulation results is achieved for two configurations with different values of the capacitance of the UC. Even if the equivalent model is not perfect with an observed frequency shift, the gain on simulation time is enormous: the Full-wave simulation takes about 45 min to complete, and the circuit model less than 10 s. Ultimately, this equivalent model could be used to design and optimize FPMS configurations of reconfigurable filters, for example. In the context of the ANR/NSERC project, this part of the work has been further developed by XLIM (Ph.D.).

### 2.4.3 Realisation of a FPMS prototype

This section concerns the fabrication of a 16 by 16 FPMS board prototype. As this research work has been done with different partners from France (XLIM, IETR) and Canada (OntarioTech, Carleton University), it has been decided to manufacture a complete FPMS board that all consortium partners could use. The manufacturing of this board is complex because the RF FPMS board is composed of 256 unit cells, and for each one, a varactor diode and inductance must be mounted while also associating a DC control card to have the capability to control the DC bias voltage of the varactor diode individually. The Voltakap company in France carries out this global manufacturing of the prototype. This manufacturing has been run at the end of 2022 and is not yet available at this time.

Technically, most of the questions have already been addressed (DC isolation between cells, RF isolation), but two last questions need to be answered. First, how to realize the DC biasing network and the control of the FPMS, and how to realize the feeding part thanks to the use of a microstrip to SIW transition (input of the FPMS)?

#### 2.4.3.1 DC biasing network and control

In the first generation of the FPMS (Canadian teams), the DC bias was controlled by an FPGA controlled by a computer. In this generation, each UC could be switched between only two states: bias or not bias, drastically limiting the reconfigurability of the board. Thus, for the new generation of FPMS, we want to attribute to each UC an independent voltage. This postulate, of course, drastically increases the complexity of the biasing network and the power supplied. As this part of the prototype is not directly linked to the Ph.D. work and is carried out by an external company, we do not develop the part concerning the control network of the cells here.

#### 2.4.3.2 Feeding part Transition from Microstrip line to SIW

The feeding part and the different transitions are one of the effective limitations of the FPMS concept. In the first prototype (1.5-3GHz), the transition used to excite the FPMS from one microstrip line has demonstrated this limitation by adding high loss.

For our new prototype, it has been chosen to use one microstrip line to SIW (Substrate Integrated Waveguide) transition and to connect the SIW directly to the FPMS. This approach comes from the fact that, for now, in simulation, the FPMS was fed by a

dielectric waveguide (close to a SIW). The transition between the SIW and the FPMS is made possible, as mentioned during the cell design, by ensuring that the dielectric constant of the positive state is close as possible to the dielectric constant of the substrate to optimize the matching between SIW and FPMS.

The microstrip line to SIW transition is based on the concept presented in [72]. Figure 2.30 shows the design and the performance of a back-to-back transition simulated with CST. This transition is composed of one microstrip line, which excites the SIW thanks to using a microstrip taper to match the impedance. In addition, two vias are added at the input and output of the SIW, respectively, to reduce the size of the taper to improve the design's compacity. This transition is designed to work between 9GHz and 16GHz. It can be noticed that the lowest frequency chosen for the transition is lower than the expected working frequency of the FPMS (10.5 GHz). Due to the complexity of the FPMS design and the use of active elements (varactor diodes), a frequency shift may occur. The lowest frequency for the transition will ensure that if the frequency is lower than expected, the design will still work.

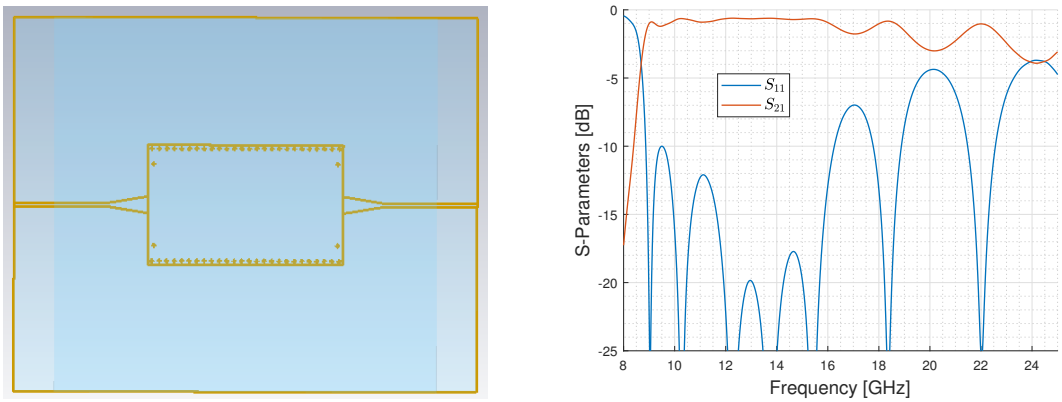


(a) (b)

Figure 2.30 – The different metallic layers of the final design

### 2.4.3.3 Complete design of the FPMS RF board

Figure 2.31 shows the schematic of the final stack-up of the dielectric (Roger RT 5880) and metallic layers that compose the FPMS with the 256 unit cells. Figure 2.32 shows the different metallic layers of the final FPMS board with the FPMS alone and the added microstrip line to SIW transitions. Four ports are considered in this final design. The 256 UC can easily be identified. As mentioned, the final size of the FPMS

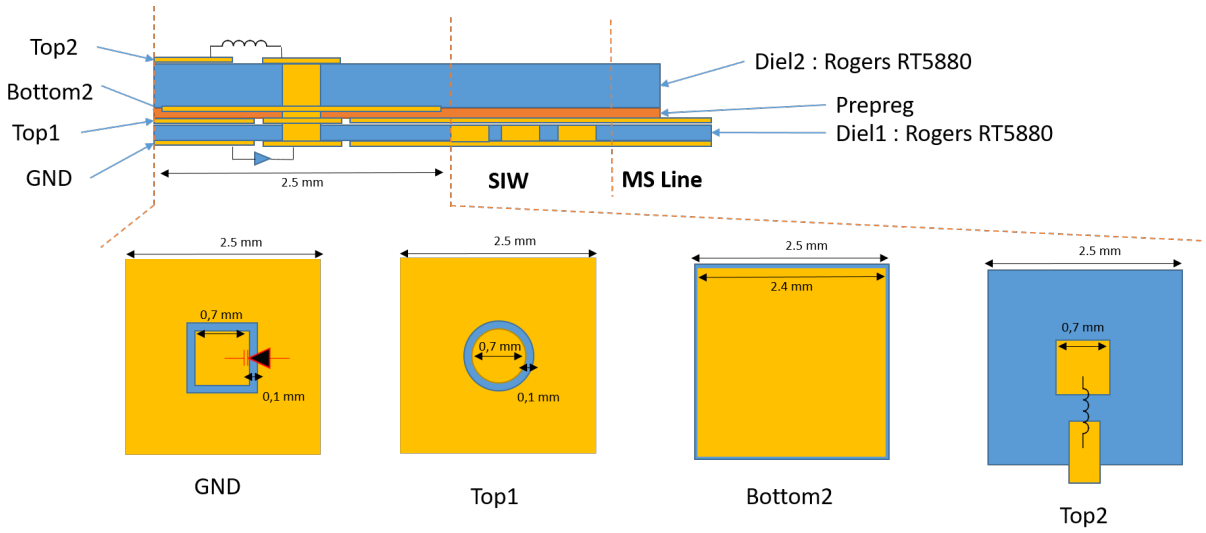


Figure 2.31 – Schematic of the Final UC

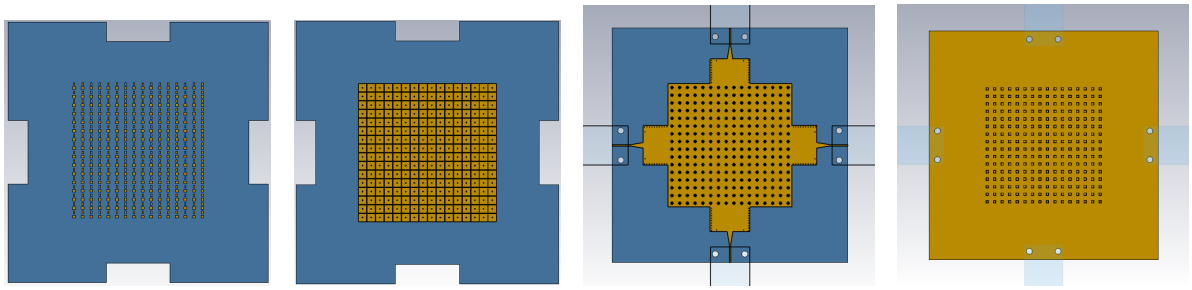

(a) Top 2 (b) Bottom 2 (c) Top 1 (d) GND

Figure 2.32 – The different metallic layers of the final design

is 40 mm × 40 mm, and it is located in the center of the board. The total dimension of the board is 76 mm × 76 mm, including the transition, the four ports, and transitions can be observed in the metallic layer top 1 (Figure 2.32c). A part of the dielectric 2 will be removed in order to access the microstrip line and fix the SMA connectors. A 3D model of the board is plotted in fig (2.33).

This design has been fully simulated in CST, and Figure 2.34 shows a comparison of results between the complete design and the simplified design (without transitions) that has been presented previously. As it can be expected, the final performances are lower than the simple design. The loss coming from two added transitions can be estimated to be around 1 dB. It can also be demonstrated that the performances at higher frequencies (for example, 16 GHz) are degraded. We obtain less than 10 dB of matching ($S_{11}$) since

(a) (b)

Figure 2.33 – 3D model

the transition has a smaller bandwidth than the FPMS. But in the end, matching also depends on the configuration of the FPMS. In other words, a FPMS configuration may exist that can improve the matching at a higher frequency.

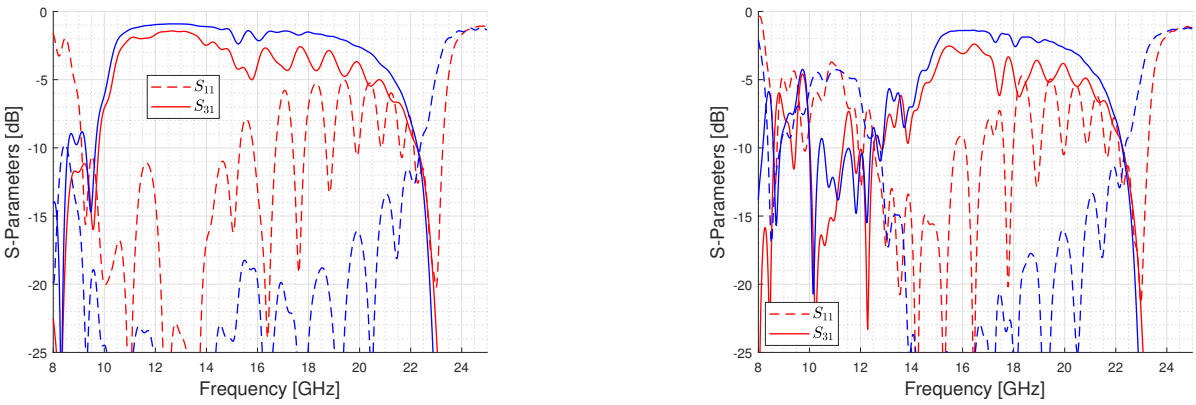


(a) (b)

Figure 2.34 – Comparison between the complete FPMS design (blue) and the simple design without transition (red) for strait waveguide configuration: (a) Cn=1.1pF, Cp= 0.14pF and (b) Cn=0.4pF and Cp= 0.14pF

Figure 2.34b shows a comparison for a different set of capacitance. In this configuration, the loss coming from the transitions is still about 1 dB. However, for more extreme configurations, like the inverted $C_p$ and $C_n$ values and a working frequency around 25 GHz, the transition will not work.

## 2.5 Conclusion

In this chapter, we have discussed the development of a new FPMS in the X band. We have started with the study of the key element: the unit cell. Depending on the

biasing of a varactor diode, the resonant frequency of the unit cell can be controlled. The resonant frequency of the final UC can be varied from 10.5 GHz and 22.75 GHz. The UC will have a positive or negative dielectric constant at a given frequency. Using the developed UC, an implementation of a $16 \times 16$ UC FPMS board is designed. To demonstrate the reconfigurable capacity of the board, different functions have been tested: simple waveguide, corner waveguide, filter, phase-shifter, and divider. The final plane is to have an independent biasing for each UC; this will allow the creation of a considerable amount of different functions with high tunability. This is why an equivalent electronic model has been developed, as it will allow quick simulation and optimization of many configurations. The prototype. The prototype is currently being manufactured (Voltakap) and will probably be available in the next few weeks. Based on the FPMS presented in this chapter, this prototype is the main technological output of the ANR/NSERC project, which will end in June 2023. Of course, when the board will be fabricated, an extensive measurement campaign will be necessary to adjust the simulation model.

### 2.5.1 Perspective

The FPMS circuit presented in this thesis works in X-band; the next logical step with this technology is to make it able to work in the millimeter wave band. From the study, using the same design for the UC, one way to increase the working frequency further is to reduce the cell's size and use a varactor diode with lower capacitance values. It seems that we have reached the limitation of the PCB technology. Reducing furthermore the size of the cell will lead to the impossibility of realizing the bias network and/or integrating the electronic components. For now, the only realistic way to increase the working frequency will be to change the technological process and go to LTTC technology, for example.

The FPMS performance is limited by two significant factors: the choice of the diode and the feeding part. Varactor diodes are the critical component of the system because they directly impact the loss, the frequency range, and the possible dielectric constant values. The main concern for the feeding part is the matching, as the impedance of the FPMS depends on many factors. The feeding transition has a lower bandwidth in the proposed design than the FPMS board. Despite the performance issue, the proposed FPMS board is a significant step in developing a fully reconfigurable system for RF functions. The idea is still to develop an equivalent of the FPGA for high-frequency systems.

Chapter 3

# Reconfigurable antenna based on one-dimensional FPMS

## 3.1 Introduction

The previous chapter was about the study and the design of a new FPMS board that works in the X band. This new board allows the optimization of different reconfigurable circuit functions: waveguides, filters, dividers, and phase shifters... Now in the two following chapters, we want to exploit the FPMS technology in order to realize reconfigurable antennas in terms of radiation patterns. We can distinguish two different approaches: one is to use a modified FPMS board that will allow the synthesis of an antenna. This first approach will be discussed in the last chapter of the manuscript and can be referred to as a two-dimensional FPMS inhomogeneous lens antenna. The second one is to use a limited number of unit cells for other antenna designs; this can be referred to as a discrete FPMS antenna or a one-dimensional FPMS Leaky Wave antenna. This second approach is studied in this chapter.

This chapter discusses how FPMS technology is used to design a reconfigurable antenna. We combine here the FPMS technology with an Half-Mode Substrate Integrated Waveguide (HMSIW) leaky wave antenna. The main objective is to develop an antenna that provides a beam steering at a fixed frequency. The chapter will be divided into 3 sections:

— The first section will be about the basic passive design,
— The second section will present the complete antenna, combining the basic antenna and the FPMS technology, that will provide a beam steering in the H-plane,
— The last section will deal with a modified antenna that allows to change the direction of the main beam and focus the radiation pattern in the E plane.

## 3.2 Passive design

The antenna presented in this section is a uniform leaky-wave antenna based on the Half-Mode Substrate Integrated Waveguide (HMSIW) technology. The HMSIW technology was first introduced in 2006 [73] and was a modification of the Substrate Integrated Waveguide (SIW) technology. In fact, the HMSIW is obtained by cutting a SIW in half along the longitudinal axis. In this case, the field that propagates inside the HMSIW corresponds to half the field of the SIW. This phenomenon can be observed in Figure3.5. It is possible thanks to two points: first, the fundamental mode of a SIW ($TE_{1,0}$) has a magnetic symmetry in its center, and secondly, the thickness of the substrate is small compared to the wavelength, so by removing half of the SIW structure, the created aperture can be approximated as a perfect magnetic conductor (PMC). This allows the HMSIW to support the $TE_{0.5,0}$ mode.

This waveguide type is, in fact, one-half of a SIW structure, yet provides the same performance for frequencies above the cut of frequency [73]. Moreover, it has been demonstrated in [45] that the open side radiates when the HMSIW is used close to the cut-off frequency. The cut-off frequency ($F_c$) of the fundamental mode of a SIW is calculated using the following formulas:

$$F_c = \frac{c}{2\sqrt{\epsilon_r} W_{eff}} \tag{3.1}$$

$$W_{eff} = w - \frac{d^2}{0.95p} \tag{3.2}$$

where $W_{eff}$ is the equivalent size of SIW compared to a standard waveguide, $w$ is the width of the SIW, $d$ is the diameter of the vias, and $p$ is the distance between two vias. The beam direction of such an antenna varies with the frequency, and it is given by the following formula [41]:

$$\theta_m = sin^{-1} \frac{\beta}{k_0} \tag{3.3}$$

Where $k_0$ is the free space wave number, and $\beta$ is the phase constant. As $\beta/k_0$ changes with frequency, the direction of the main beam also varies.

The passive design of our HMSIW Leaky-wave antenna is presented in Figure3.1 alongside a photograph of the manufactured prototype. The length of the HMSIW is $l = 79.5\,\text{mm}$, and the total length of the substrate is $L = 89.5\,\text{mm}$. The width of the global substrate is $W = 40\,\text{mm}$ and the width of the HMSIW is $a = 7.35\,\text{mm}$. The width

of the microstrip line is $Wl = 2.4\,\text{mm}$. The diameter of the vias is 0.3 mm and the pitch between them is $p = 1.5\,\text{mm}$. The design is done on a 0.787 mm thick Rogers RT5880 substrate. With the given dimensions, the cut-off frequency is estimated to be at 7.5 GHz using equation 3.2.

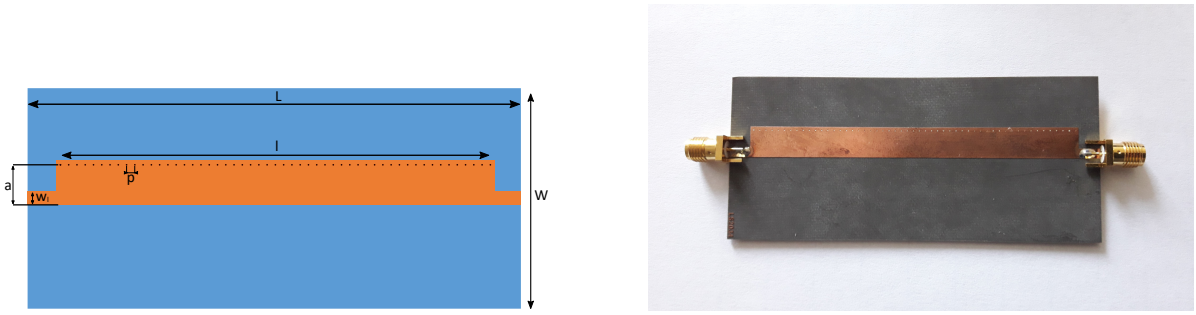


Figure 3.1 – Antenna prototype

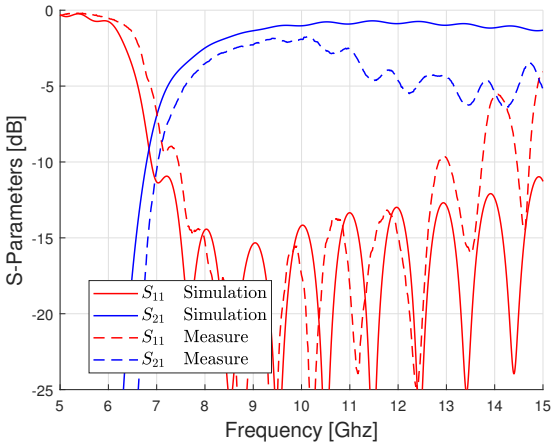


Figure 3.2 – Simulated and measured S-parameters

Simulated (CST) and measured S-parameters are shown in Figure 3.2. From the $S_{21}$ parameter, it can be observed a 250 MHz frequency shift between simulation and measurement results. Moreover, it exists a higher loss for measurement at high frequencies ($> 10.5\,\text{GHz}$) probably due to the connector used (mismatching and radiation).

Figure 3.3 presents the antenna's simulated and measured radiation patterns. The frequency shift has been taken into account. The simulated and measured results have been normalized to their respective maximum, 9.2 dBi at 7 GHz for the simulated ones and 8.4 dBi at 7.5 GHz for the measured ones. As can be expected from a leaky wave antenna,

the main lobe direction changes with the frequency. The steering angle also depends on the cut-off frequency. The gain variation and the main lobe direction can be observed in Figure 3.4. It can be easily demonstrated that the gain varies with the frequency and the steering angle too. To define the antenna's bandwidth, we consider that it works when the gain variation from the maximum gain achieved is less than 3 dB. In this case the antenna will work between 6.7 GHz and 8.5 GHz, with a main beam direction variation between 13° and 53° for measurement. Figure 3.5 presents the electric field along the HMSIW for two different frequencies. When the frequency changes, it is easy to see that the number of maxima of the electric field is impacted, demonstrating that the phase constant $\beta$ is modified, and so is the beam steering angle.

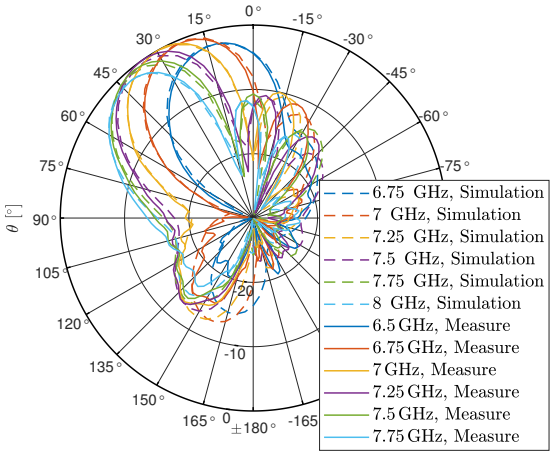


Figure 3.3 – Simulated and measured normalized radiation patterns

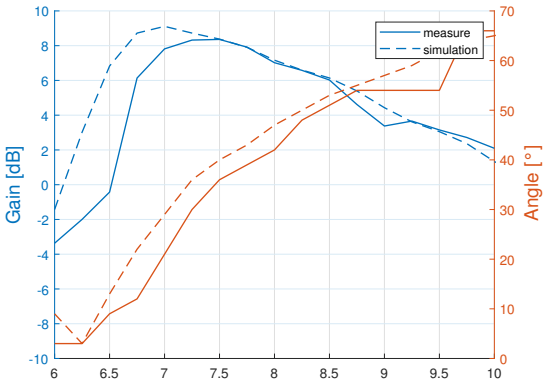


Figure 3.4 – Simulated and measured normalized gain and beam steering

(a) (b)

Figure 3.5 – Electric field distribution along the waveguide at (a) 7.5 GHz and (b) 8.5 GHz

## 3.3 Reconfigurable leaky wave antenna

This section aims to develop an antenna giving the capability of a beam steering at a fixed frequency. To achieve this objective, the phase constant $\beta$ in the equation 3.3 needs to be controlled by other means than changing the frequency. So in this section, we integrate FPMS unit cells into the previous design in order to be able to control the beam direction at a fixed frequency.

### 3.3.1 Unit Cell

The unit cell used for this reconfigurable antenna is based on the basic one presented in 2.3.2.1. This cell is shown in Figure 3.6 with $m = 1.5\,\text{mm}$, $g = 0.2\,\text{mm}$, $pad = 0.6\,\text{mm}$ and $h = 0.787\,\text{mm}$.

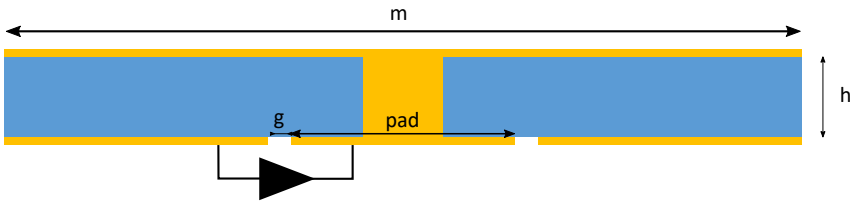


Figure 3.6 – Schematic of the "Basic" unit cell

The cell's extracted parameters (dielectric constant, magnetic constant, and refractive index) are shown in Figure 3.7. These parameters are extracted with the same method as in the precedent chapter. Again it can be observed that the capacitance variation changes the resonant frequency. Also, thanks to the small size and high thickness of the cell, the cell offers a very wide band for negative dielectric constant.

The cell's performance is an interesting metric to look at, but for this precise application, the hypothesis for the cell is not fulfilled. In fact, in order to extract the parameters of the cell, the cell is considered to be inside a parallel plate structure. However, in the

present reconfigurable HMSIW design, the cell is not surrounded by other cells with a periodic structure, as was the case for the 2D FPMS in the previous chapter.

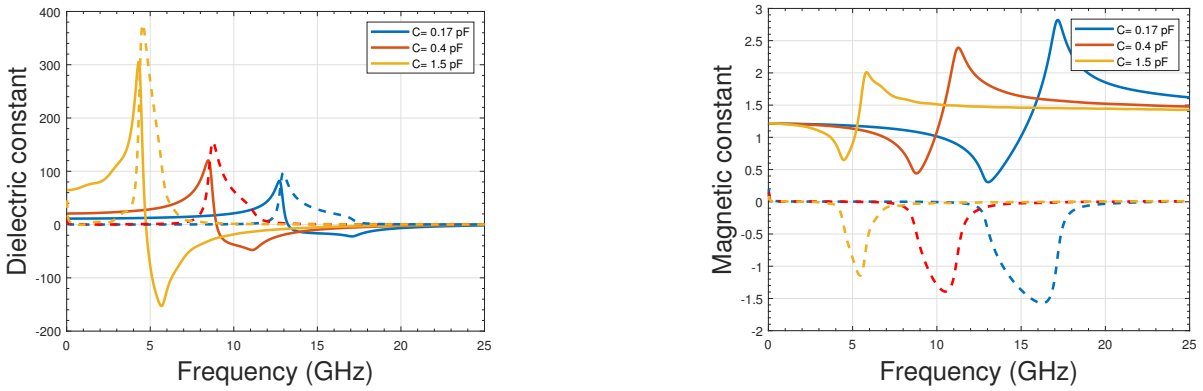


(a) (b)

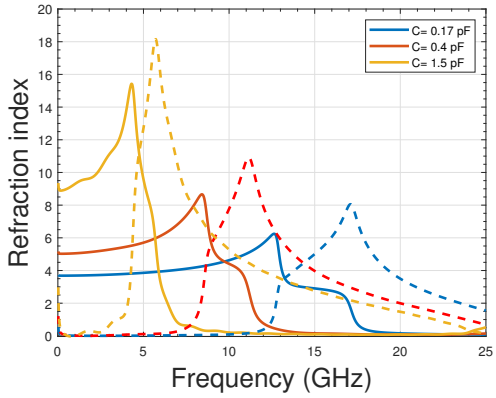


(c)

Figure 3.7 – UC parameters

### 3.3.2 Antenna design

The antenna is a half-mode substrate integrated waveguide (HMSIW) structure of 79.5 mm length ($l$) and 7.25 mm width ($a$). It is realized on Rogers RT5880 substrate with a thickness of 0.787 mm, dielectric constant $\epsilon_r = 2.2$ and loss tangent of $tan\delta = 0.0009$. The fabricated prototype of the HMSIW antenna is shown in Figure 3.8. The conceptual image of the unit cells integrated along the PEC boundary of the antenna is illustrated in Figure 3.8 (c) alongside a zoomed photo of the actual structure. The diameter of each via is 0.3 mm ($d$) and the spacing between via ($S$) is 1.5mm. Each via is connected to the ground through a MA46580-1209 Macom varactor diode (Beam lead). With the chosen

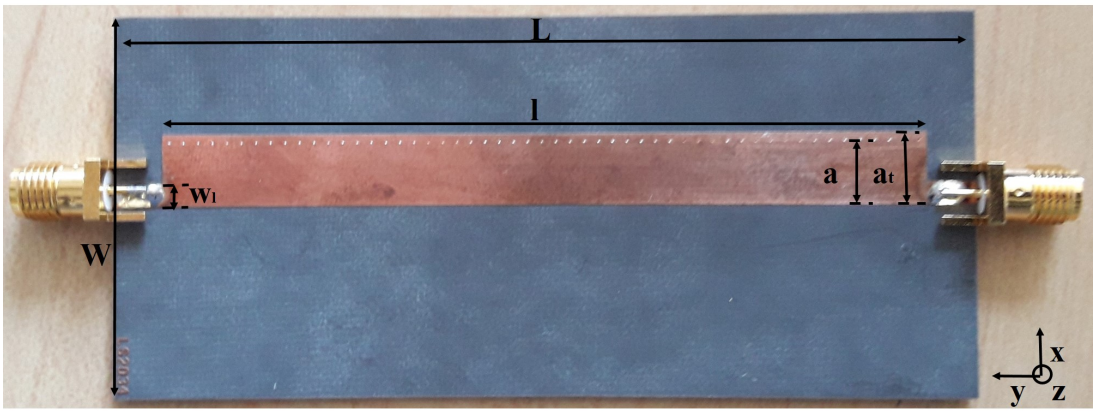


(a)

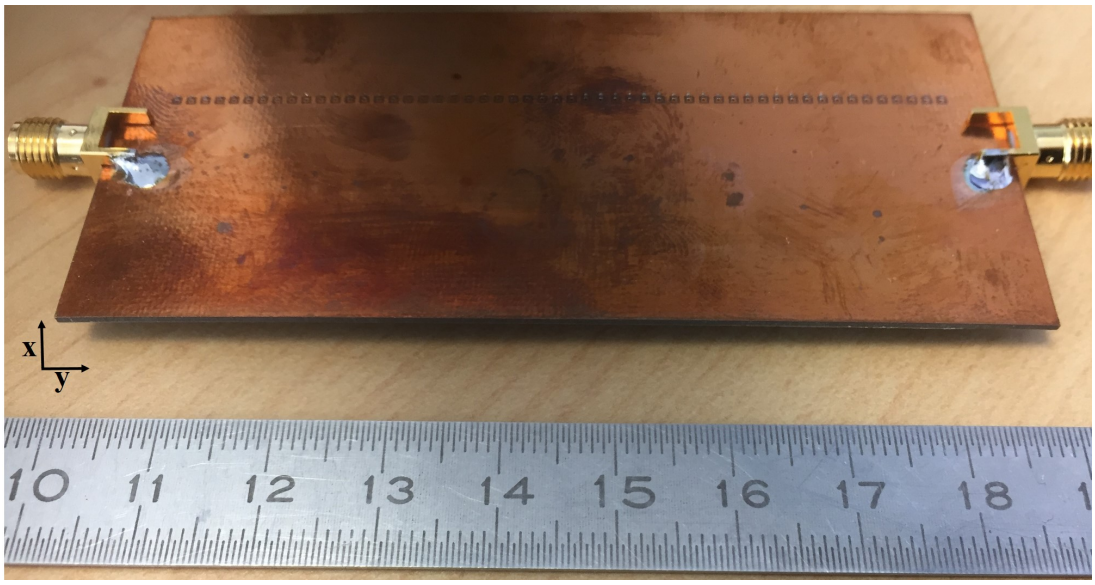


(b)

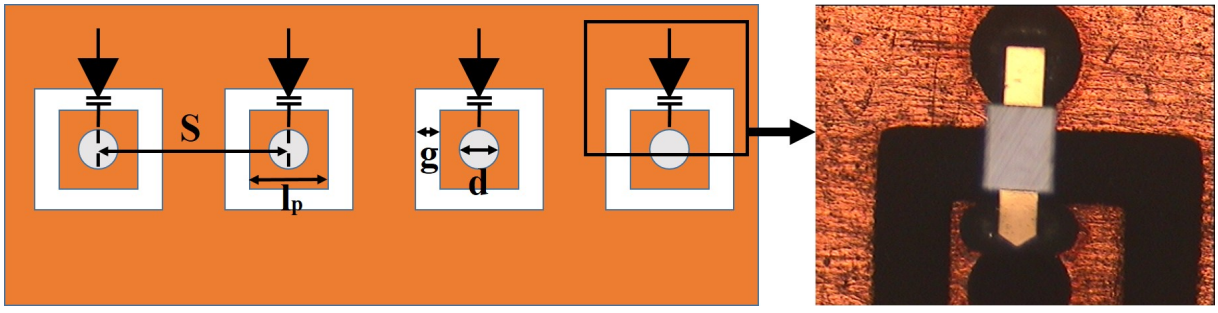


(c)

Figure 3.8 – Antenna prototype: (a) Top view, $L = 89.5\,\text{mm}, W = 40\,\text{mm}, l = 79.5\,\text{mm}, a = 7.25\,\text{mm}, a_t = 8\,\text{mm}, w_l = 2.4\,\text{mm}$, (b) bottom view and (c) Varactor placement, $g = 0.2\,\text{mm}, d = 0.3\,\text{mm}, l_p = 0.6\,\text{mm}, S = 1.5\,\text{mm}$

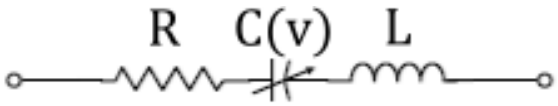


Figure 3.9 – Varactor diode equivalent RLC circuit

dimensions, this antenna uses a total of 53 diodes, all biased with the same voltage at a time.

As mentioned in 2.3.1, the varactor diode used for this precise design is depreciated. However, all parameters of the diode are already known since it has been characterized in [71] and an equivalent RLC circuit (Figure 3.9) can be used to explain its RF response. The equivalent circuit consists of a serial combination of $L = 0.105\,\text{nH}$ and $R = 2.2\,\Omega$ along with a variable capacitor. The value of the capacitor can be ascertained using (3.4) as it can be observed that the applied bias across the varactor controls the capacitance value and its resulting performance. This model is used in this work to carry out the full-wave simulations of the antenna design.

$$C(V) = \frac{C_0}{(1 + \frac{V}{V_0})^{\psi}}, C_0 = 1.56\,\text{pF}, V_0 = 5.755\,\text{V}, \psi = 1.96 \tag{3.4}$$

### 3.3.3 Simulation results

The electric field distribution inside the FPMS HMSIW is shown in Figure 3.10. The simulated results show the magnitude of the propagating E-field inside the waveguide. In the unbiased state (0 V) at 8 GHz (Figure 3.10(a)), the via wall loaded by varactor diodes acts as a quasi-normal metallic wall, thus allowing the propagation of $TE_{0.5,0}$ mode. This state corresponds to the case of a waveguide with the maximum effective width. By changing the voltage, the distance between two maxima of the electric field in the waveguide is modified, which means that the propagation constant is changed and the effective width of the waveguide is reduced (Figure 3.10(b)). In fact, in this case, it can be observed that some energy is stored inside the unit cell.

In the extreme case of varactor bias (12 V) (Figure 3.10(c)), the effective size of the waveguide becomes too small for the $TE_{0.5,0}$ mode to propagate at 8 GHz, and most of the power is reflected.

This physical explanation of the waveguide performance is clear from the simulated S-parameters shown in Figure 3.11. Depending on the varactor diodes' state, the waveguide

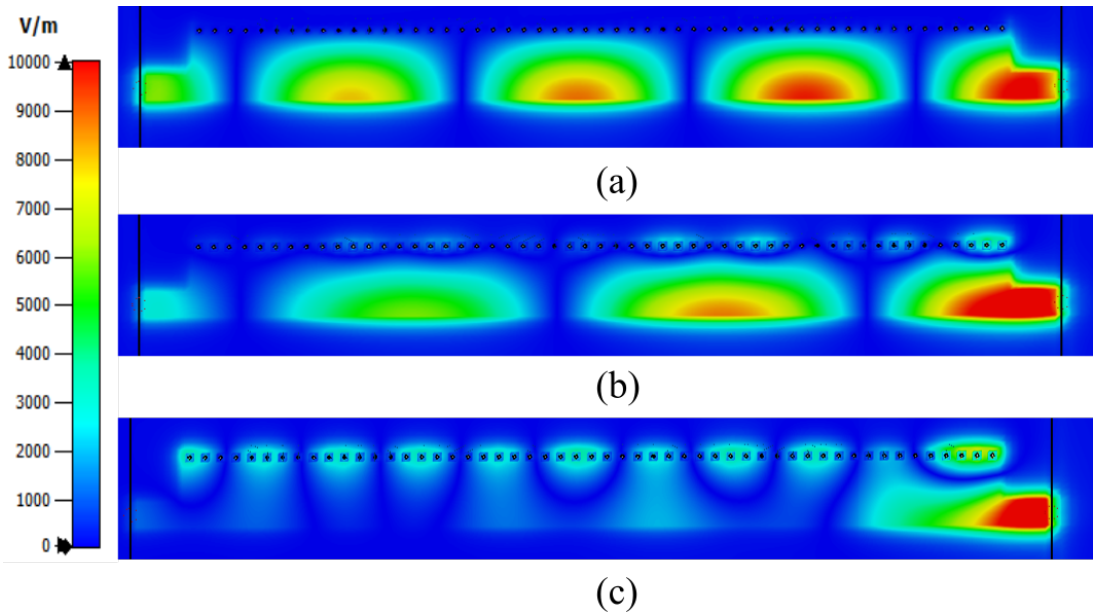


Figure 3.10 – Electric field distributions along the waveguide ($z = 0.25\ mm$) at 8 GHz for three different voltages: (a) 0 V, (b) 4.7 V and (c) 12 V

structure's cut-off frequency can be controlled, as shown from the $S_{21}$ plot in Figure 3.11. These results validate the operating principle of the waveguide structure loaded with FPMS unit cells.

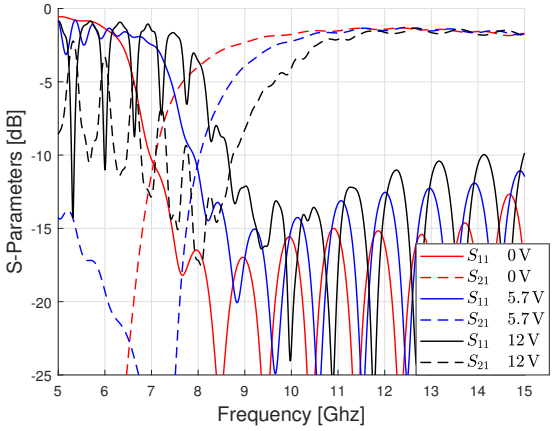


Figure 3.11 – Simulated S-Parameters for 3 different biases

The overall antenna has been simulated in CST Microwave Studio. The varactor diode of the FPMS unit cell is modeled by an RLC lumped element circuit with a variable capacitance. As mentioned above, the cut-off frequency changes with the varactor diodes' DC bias. The radiation pattern of the simulated antenna in the H-plane at 7.75 GHz is

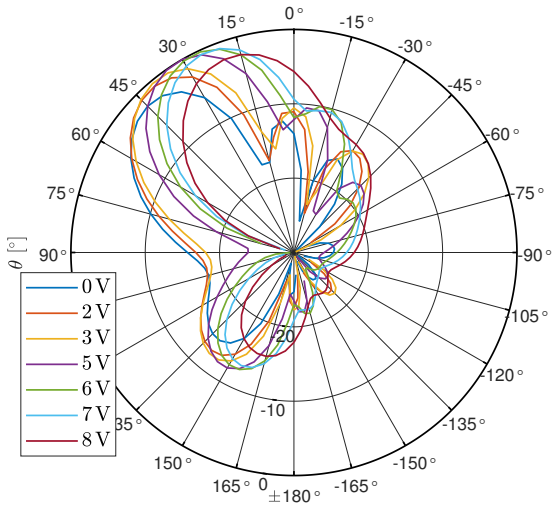


Figure 3.12 – Realized normalized radiation pattern at 7.75GHz in H-plane($\Phi = 90°$) for different bias voltage

shown in Figure 3.12. At this frequency, the antenna achieves a beam steering from 18° to 45° with gain varying from 6.7 dBi to 9 dBi. The maximum gain is obtained with the 5V configuration for an angle of 32°. It is noticeable that the extreme angles (18° and 45°) have the lowest gain, which is expected. The 18° angle is obtained when the voltage is set at 8V. For this configuration, the return loss is -6 dB, reducing the antenna's gain. In fact, a higher bias voltage could provide a better steering range. However, it would reduce the overall gain of the antenna due to its poor matching performance. On the other hand, for a steering angle of 45°, the bias voltage is set at 0 V. In this case, the antenna gain is still affected but not due to the mismatch of the antenna. Instead, it is due to the transmission of the power to the other port. This is evident from $S_{21}$ of the antenna shown in Figure 3.11.

Figure 3.13 shows a results comparison between the 0V configuration and the passive design presented previously. As expected, both cases show similar behavior, the same angle achieved, and the same gain variation. The only observable difference is the reduced gain of the active antenna, but this reduction directly comes from the parasitic resistor of the diode, which induces loss.

One can increase the antenna size to improve the gain and radiation performance. This phenomenon is illustrated in Table 3.1, where longer antennas provide better gain values. However, a longer antenna complicates the practical handling of the antenna. Therefore, we kept the antenna size to 79.5 mm as it still provides the proof-of-concept.

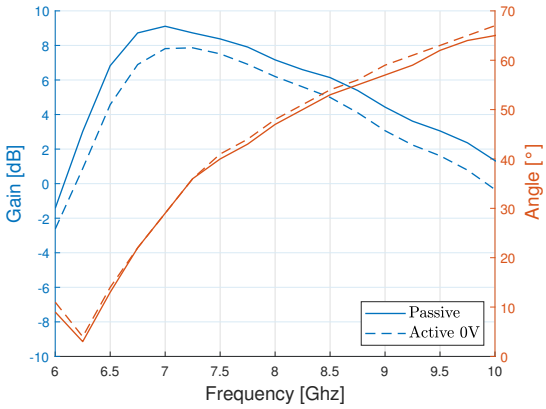


Figure 3.13 – Realized gain and main beam angle

Table 3.1 – Impact of the size of the waveguide on the performance of the antenna at 8 GHz

| Size | number of Diodes | Beam steering | Maximum gain |
|---|---|---|---|
| 79.5 mm (2.12 $\lambda$) | 53 | 18° to 48° | 9.3 dBi |
| 150 mm (4 $\lambda$) | 100 | 28° to 54° | 11.9 dBi |
| 225 mm (6 $\lambda$) | 150 | 29° to 57° | 13.2 dBi |

Another way to improve the radiation performance is to reduce the parasitic resistance by changing the used diode.

Note that this antenna has two input ports, so if the signal is exited on the second port, it leads to the same results but for a beam varying from $-18°$ to $-45°$.

The antenna radiates with a beamwidth of 30° in the H-plane. However, this value varies with the applied voltage. As the antenna beam is steered, its beamwidth is seen to increase in the H-plane. In E-plane, the antenna beamwidth is between 55° and 65°.

The cross-polarization is below $-15$ dB, whatever the voltage configuration and the frequency. Thus, these results validate the effect of FPMS unit cell integration on the antenna radiation performance by steering the beam around the maximum gain value with acceptable radiation performance.

The design is simple, so the different parameters which can be changed to tune the antenna to a specific application are limited. First, the width of the waveguide will directly impact the working frequency as the cut-off frequency changes with the width. Of course, for the active design, the behavior of the unit cell needs to be taken into account. The length of the waveguide, on the other hand, impacts the gain of the antenna: the longer the antenna, the higher the gain (up to a certain limit). The goal of a leaky-wave antenna

is to have the minimum power that goes to the end of the antenna, which means all the power has been radiated. The last parameter concerning the global design is the size of the ground plane. It mainly affects the shape and beam width in the E-plane.

### 3.3.4 Prototype results

The measured S-parameters of the antenna for three different bias voltages of the varactor diodes are shown in Figure 3.14. The results are in good agreement with the simulated ones (Figure 3.11) with two minor deviations. Firstly, a frequency shift is observed between the simulated and measured results that changes with the applied bias. The range of this shift in the frequency is from 0.25 GHz to 0.5 GHz. The frequency shift for the low bias voltage is the same as the one observed for the passive design (section 3.2). The increase of the frequency shift with the voltage could come from the non-perfect model of the used Varactor diode.

It can also be observed that there is some discrepancy between simulated and measured results at higher frequencies (above 12 GHz), but for these frequencies, the antenna is not designed to radiate well, thus it is not of any concern.

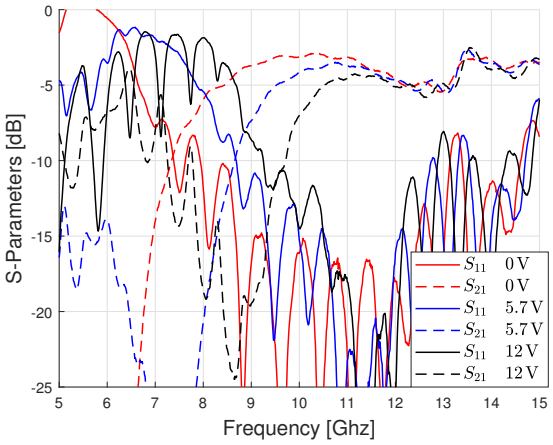


Figure 3.14 – Measured S-Parameters for 3 different bias voltages

An essential issue in the measured reflection coefficient ($S_{11}$) of the antenna is that the antenna matching at 8 GHz is affected due to the biasing of the varactor diodes. This is an anticipated response from a waveguide-based LWA structure. Such a design radiates well close to the cut-off frequency of the waveguide, which is the rationale for choosing 8 GHz as the frequency of interest. However, due to biasing of the varactor diodes, this frequency shifts towards the higher bands as explained in section 3.2. The resulting deterioration in

the reflection coefficient affects the overall gain of the antenna. Nonetheless, in this case, the antenna did not incur a significant change in maximum gain due to the mismatch. Thus, as the first-ever design using FPMS technology and delivering acceptable radiation performance, these results are presented without further optimization. In future antenna designs, a key objective will be to improve impedance matching as a refinement of the design concept.

The measured radiation patterns of the antenna in the H plane for different bias voltages are shown in Figure 3.15. This prototype achieves a measured beam steering from 18° to 45° with the gain variation from 5.95 dBi to 7.55 dBi. By taking into account the frequency shift, this result can be compared with the measured ones in Figure 3.16. Generally, a good agreement can be observed between the two sets of results with some difference in the gain values. One observation is that the tilt angle 18° is achieved for the 7 V configuration and not for the 8 V configuration, like in the simulation. This is due to the frequency shift that increases with the bias voltage. For the 8 V configuration, the antenna prototype achieves a tilt angle of around 15°, but the gain falls to 4.22 dBi, which is relatively low as compared to the maximum antenna gain. Only a finite number of configurations are shown in the measurement, but this antenna uses varactor diodes, allowing continuous beam steering. Thus, the simulated and measured results clearly validate the effectiveness of this LWA design in providing beam steering at a fixed center frequency of the antenna.

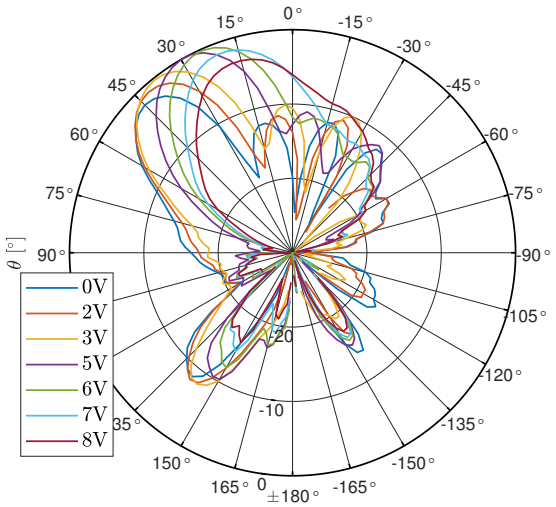


Figure 3.15 – Measured normalized radiation pattern at 8 GHz in H-plane($\Phi = 90°$) for different bias

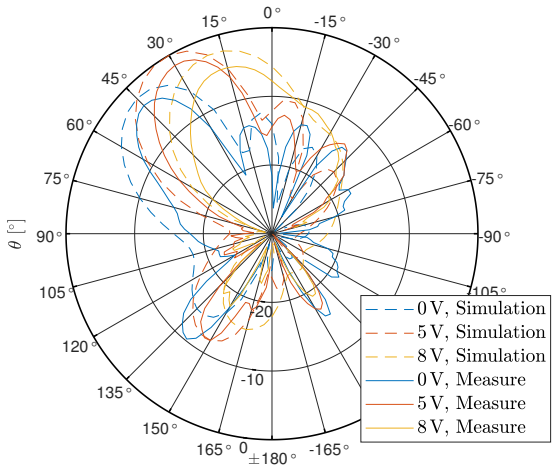


Figure 3.16 – Comparison between simulated and measured gain in H-plane for different bias (simulated results are at 7.75 GHz and measured result are at 8 GHz taking into account the frequency shift)

Figure 3.17 presents a comparison of measurement results between the passive design and the active antenna at 0 V. In addition, this result can be compared to the simulated one (figure 3.13). As expected, the active antenna has the same gain and beam angle variation as the passive design for the 0 V configuration. Again it illustrates that most of the gain reduction comes from the varactor diodes with their parasitic resistor.

In any case, the antenna's performance is slightly lower than what was expected from the simulation. The table 3.2 shows a compilation of the gain variation. As it was mentioned for the passive antenna, the maximum gain is already lower than expected. This further increases with the active antenna.

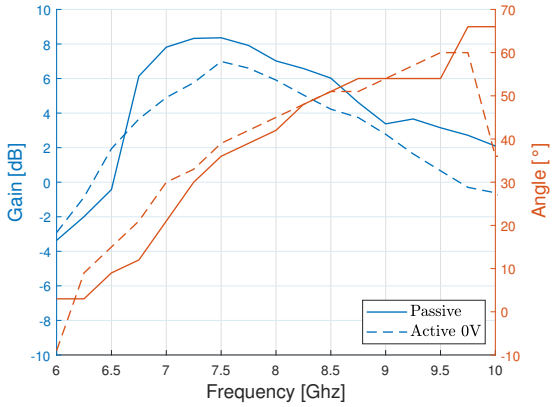


Figure 3.17 – Measure gain and main beam angle

| Configuration | 7 GHz | 7.5 GHz |
|---|---|---|
| Simulation passive | 9.2 dBi | 8.4 dBi |
| Simulation active 0V | 7.8 dBi | 7.5 dBi |
| Measure passive | 7.8 dBi | 8.4 dBi |
| Measure active 0V | 4.9 dBi | 7 dBi |

Table 3.2 – Gain for the different configurations

### 3.3.5 Fixed Beam over frequency

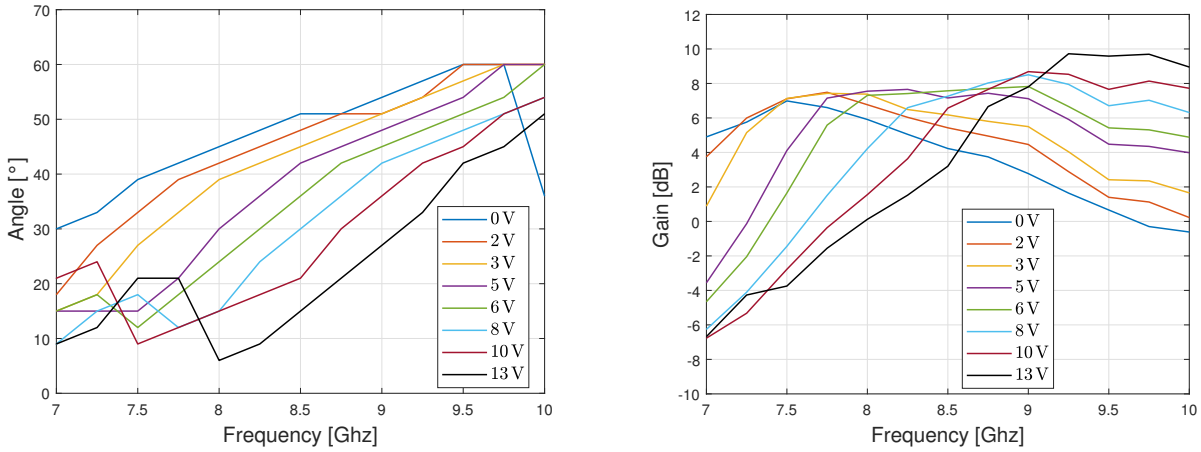


(a) (b)

Figure 3.18 – Maximum measured gain and main beam direction for different configurations

Another investigation carried out on this design is to achieve constant beam direction for different signal frequencies. This can be accomplished by properly modulating the antenna waveguide with the varactor diodes biased in a particular fashion. For this purpose, the antenna is characterized over a wide frequency bandwidth for different bias voltages. These results are illustrated in Figure 3.18a and Figure 3.18b. The first of these two Figures explains the variation of the main beam direction vs. bias voltage, while the latter one shows the gain variation. By appropriately combining these two results, one can obtain a constant radiation direction over a frequency band. The proposed antenna is able to provide these results by carefully selecting the bias voltages for different center frequencies. The results are shown in Figure 3.19 where a fixed beam at $35° \pm 2°$ is radiated from the antenna at each frequency. The antenna gain varies from 7.13 dBi to 9.7 dBi, over 1.75 GHz of bandwidth between 7.5 GHz and 9.25 GHz. Different fixed angles between 20°

and 40° can be achieved, but not always for exactly the same frequency bandwidth.

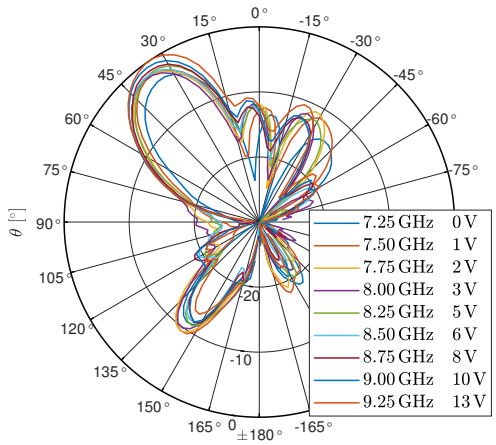


Figure 3.19 – Measured normalized radiation pattern for a fixed beam in H-plane ($\Phi = 90°$) at $35° \pm 2°$ over frequency

This is an interesting result that is derived from the proposed LWA design. As the state-of-the-art of LWAs usually shows one characteristic at a time. Either beam steering is achieved by varying the signal frequency, or it is obtained at a single frequency.

We have demonstrated that this antenna can work in three different manners: beam steering over frequency, beam steering at one fixed frequency, and fixed beam over frequency. The first one comes from the classical behavior of a leaky wave antenna, but with the active design, the center frequency can be adjusted. The second one is the primary goal of this design, achieving beam steering at a given frequency. Finally, the last one combined the two other properties to cancel the natural behavior of a leaky wave antenna.

## 3.4 E-plane focusing

For now, we have mainly discussed the antenna's performance concerning the radiation patterns on the H-plane, as it is the plane where the beam steering is controlled. In this part, we will focus on the performance of the E-plane and how to narrow it.

### 3.4.1 Impact of the size of the ground plane in E-plane

The radiation pattern in the E-plane of the passive design is presented in fig 3.20. The beam width is around 65°. Note that the active one shows the same result. For this type

of structure, the beam width and the beam direction in the E-plane are mostly linked to the size of the ground plane.

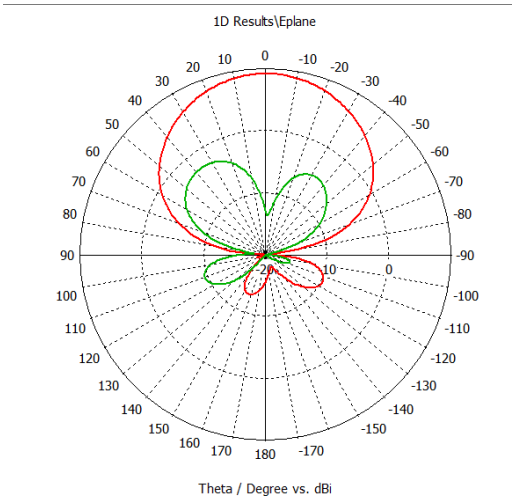


Figure 3.20 – Simulated realized gain at 7GHz in E-plane (co and cross-polarization)

One very interesting case is when the ground plane is reduced to the minimum possible. The ground plane is limited to the edge of the radiating side of the waveguide. In this case, a quasi-omnidirectional beam can be achieved in the E-plane. This phenomenon is illustrated in Figure 3.21. Of course, the performance in the H-plane remains the same. The antenna will still have a beam steering over the frequency (and with the applied voltage on the varactor diodes in the case of the active concept).

In order to reduce further the beam width in the E-plane, one solution will be to create an array of LWAs in this plane, but the implementation is not so easy. Another solution is to add a horn-like structure to the antenna to focus the beam. This solution is explored in the next section.

### 3.4.2 LWA associated to a horn-like structure

In order to narrow the beam in the E-plane, the previous HMSIW antenna is cut (along its radiating edge) and placed between two half metallic horn structures as shown in Figure 3.22. This horn structure is also used to change the propagation vector, which will be in the X direction, while this vector was in the Z direction without the horn-like structure. The shape of the metallic structure is optimized to have a constant radiating aperture (Height of 78mm) over the phi angle ($xy$ plane) in order to keep a stable gain when the beam is steered in the H plane as shown in the previous section.

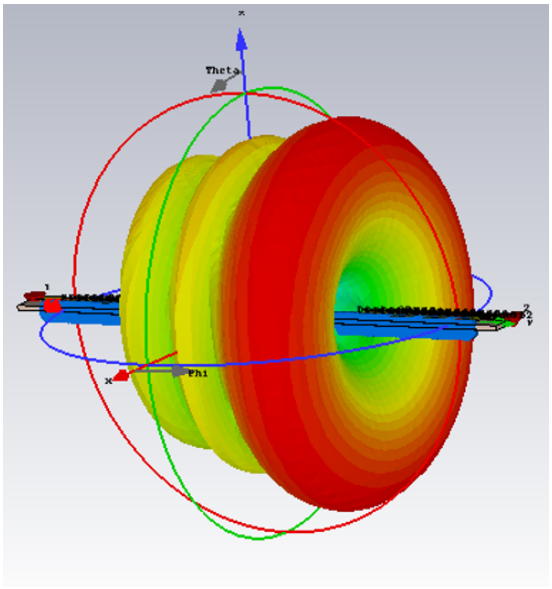

Figure 3.21 – Quasi-omnidirectional antenna in E-plane

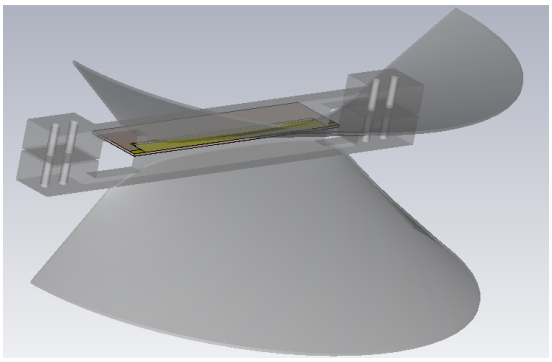

Figure 3.22 – HMSIW inside the mechanical horn.

The simulated radiation pattern in E-plane is plotted in Figure 3.23a. It can be seen that the beam width has been drastically reduced and is now around 24°. The side lobe level is close to −10 dBi, but this level could be reduced by optimizing the size and shape of the horn structure.

In the H-plane, the antenna keeps the same behavior as the HMSIW without the horn-like structure. Figure 3.23b shows the radiation pattern of the simulated antenna in the H-plane for different bias voltage at 8.5 GHz. At this frequency, the antenna achieves a beam steering from 19° to 45° with gain varying from 10.2 dBi to 13.4 dBi. The maximum gain is obtained with the 5V configuration for an angle of 39°. The beam width in the H-plane has been a little bit increased and it is now between 28° and 32°, and the side-lobe

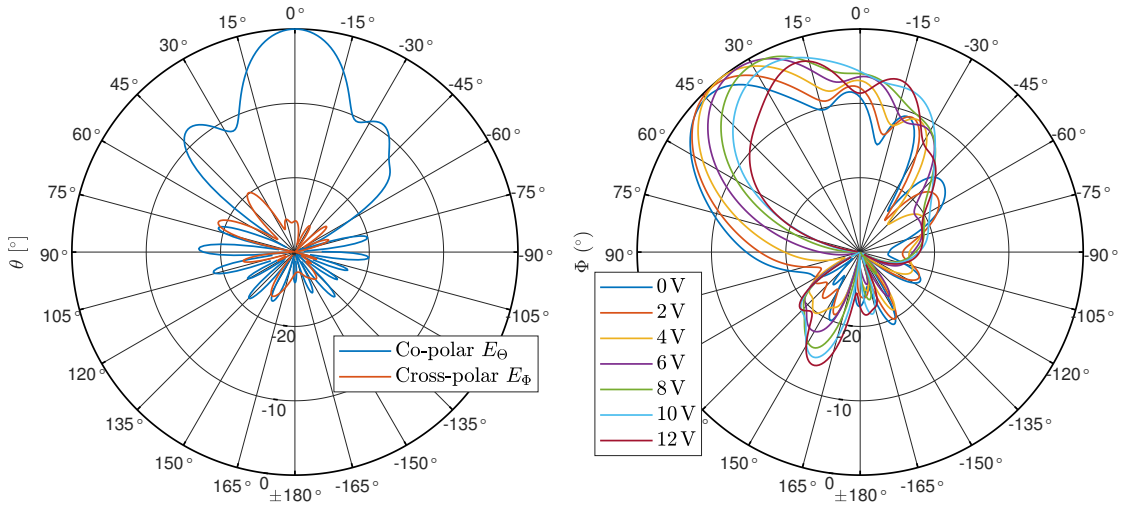


(a) (b)

Figure 3.23 – Realized normalized gain: (a) in E plane ($xz$ plane) for a 13 V bias at 9 GHz and (b) in H plan($\Theta = 90°$, $xy$ plane) for different bias at 8.5 GHz.

level has increased too.

#### 3.4.2.1 Experimental result

To validate the results experimentally, the initial idea was to use the previous active prototype and directly modify it. However, during this process and due to the mechanical weakness of the diodes and the gluing method, the first prototype no longer works. So, finally, a new prototype has been made. However, as it was stated in section 2.3.1, the initial MA46580-1209 Macom varactor diode is no longer available, so the final prototype uses an equivalent diode: the MAVR-000120-1141 Macom varactor. The final prototype is shown in Figure 3.24, where the antenna is placed inside the metallic structure.

The measured radiation patterns are shown at 8 GHz in Figure 3.25 for both planes (E and H). At this frequency, the antenna achieves a beam steering from 48° to 26° with a gain varying from 6.8 dBi to 8.8 dBi. Compared to the simulation, the prototype has a lower gain, mainly due to a wider beam in the H-plane and higher back lobe radiation. These degraded parameters may come from different sources, such as the performance of the new diode and the fabrication process. It is also likely that the SMA connectors used produce some unwanted leakage. Also, as the diodes are mounted in a serial configuration, it is impossible to check if all the diodes are working correctly. In the E-plane, the metallic horn gives the expected result as it is shown in Figure 3.25a for a 8 V bias voltage at 8 GHz.

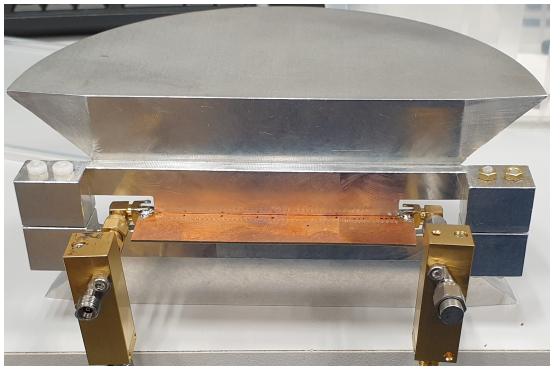

Figure 3.24 – Photo of the antenna prototype.

The beam width remains around 24°.

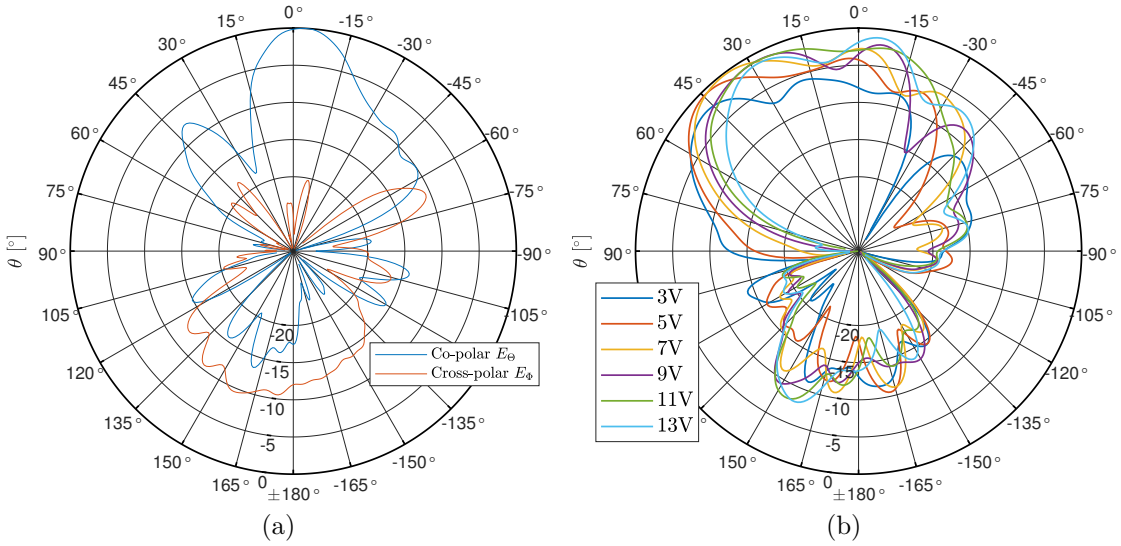


(a) (b)

Figure 3.25 – Measured normalized gain: (a) in E plane ($xz$ plane) for a 8 V bias at 8 GHz and (b) in H plan($\Theta = 90°$, $xy$ plane) for different bias at 8 GHz.

In the end, compared to the first antenna, it can be concluded that it is possible to change the beam direction and to focus the beam in the E-plane. Therefore, and despite the degraded performance in the H-plane, this antenna keeps the property of the first antenna. That means this second prototype will achieve H-plane beam steering over frequency, beam steering at a fixed frequency, and a combination of both.

## 3.5 Conclusion

In this chapter, in the first part, an electronic fixed-frequency beam-scanning LWA based on a combination of HMSIW structure and FPMS technology is presented. The beam-scanning property is achieved by electronically changing the waveguide's effective width thanks to adding varactor diodes inside the wall via holes. By changing the bias voltage of all the varactor diodes between 0 V and 13 V, the beam direction can be controlled. A continuous beam steering can be achieved at one fixed frequency, with the best case exhibiting beam steering from 18° to 45°. This antenna can also overcome the natural beam steering of a LWA with frequency to achieve a fixed beam angle over a wide frequency bandwidth up to 1.75 GHz band for an angle of 35°. In the second part, the LWA antenna is modified and used as a feeder of the like-horn antenna. The electronic beam-steering property is kept.

Chapter 4

# Reconfigurable lens antenna based on two-dimensional FPMS

## 4.1 Introduction

In the previous chapter, a reconfigurable leaky-wave antenna that used the FPMS technology is presented. However, only a limited number of unit-cell were used, all placed in a line. That is why the previous antenna was referred at a 1D FPMS antenna. This chapter will present a 2D FPMS approach for designing antennas. We will use the FPMS capability to control the artificial material's refractive index to design inhomogeneous lens antennas. Depending on the achievable refractive index from the unit cell, most of the lens design could be achieved like Lunberg one, but we will focus our research work on Mikealian lenses.

This chapter is composed of two parts. In the first part, passive Mikaelian lenses will be studied. In the second part, a FPMS lens will be presented. The FPMS board will be used to synthesize a Mikaelian lens, and the reconfigurability of the FPMS will be used to achieve beam steering capability for this lens design.

## 4.2 Mikaelian lens

Basically, the Mikaelian lens is a cylindrical lens [54]. The refractive index decreases from the center to the periphery of the lens, so the ray path inside the lens would have the same length. This means it has the same propagation velocity throughout the modes, similar to how an optical fiber works. Figure 4.1a shows the ray tracing inside an optical fiber, and Figure 4.1b shows the ray tracing of a Mikaelian lens.

Comparing the Mikaelian lens with other gradient index lenses, at least two advantages can be noted. First, the Mikaelian lens has a flat surface in contact with the primary source, which is at the base of the cylinder. This allows ease of integration with any source

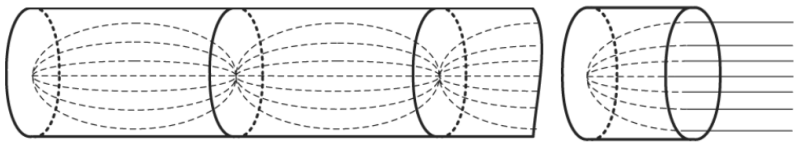


Figure 4.1 – Ray tracing inside: (a) optical fiber or self-focusing waveguide, (b) Mikealian lens

or antenna. Next, the Mikaelian lens also has an axial symmetry of its refractive index distribution compared to the Luneburg lens and Maxwell's fisheye lens, which have central refractive index distribution. This leads to a less complex and ease of manufacturing for the Mikaelian lens.

The refraction index of the Mikaelian lens varies with the radial distance $r$ as defined by the following equation 4.1:

$$n(r) = \frac{n(0)}{cosh(\frac{\pi}{2T}r)}, \text{avec } 0 \leq r \leq R \tag{4.1}$$

$T$ and $R$ correspond respectively to the cylinder's thickness and radius (see Figure 4.2). $n(0)$ is the refractive index along the cylinder axis. $n(0)$ could be any value, and this property provides a degree of freedom. Another interesting property of this law is that the ratio $T/R$ directly impacts the refractive index range. Figure 4.3 illustrates this impact. The thicker the lens is compared to its radius, the smaller the variation of the refractive index. Indeed a compromise needs to be found between the size of the lens and the variation of the refractive index.

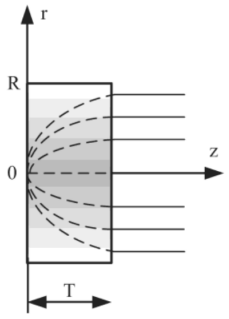


Figure 4.2 – General view of ray tracing inside a Mikaelian lens

The Mikaelian lens will be the central subject of this chapter. First, we will study

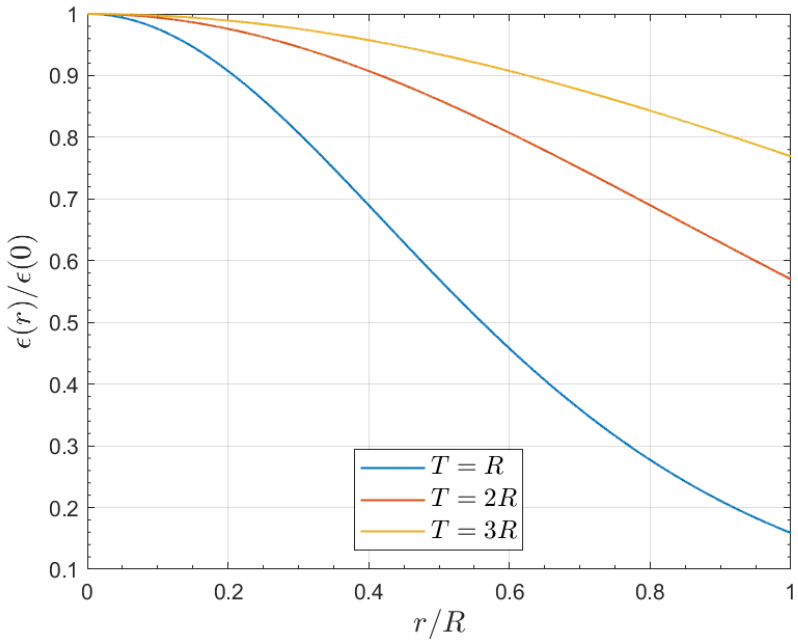


Figure 4.3 – Impact of the ratio $T/R$

the beam-steering capability of this lens. We will start with a passive design manufactured thanks to a straightforward and accurate technological process based on one unique foam material, but as we will advance in this chapter, we will look at the electronic reconfigurability of the radiation pattern. The final step will be associating the Mikaelian concept with the FPMS technology to access an original reconfigurability principle. Until recently, the beam-steering capability of passive Mikaelian lenses has never been studied extensively. The first complete study with a working prototype was published in 2021 [74]. The different results for passive design in this chapter will be similar, but essential differences will concern the fabrication process, the compacity of our design, and the feeding techniques.

## 4.3 Passive Mikaelian lens using pressed foam technological process

This section presents the design of a foam-based Mikaelian lens. We will discuss the theoretical law of the Mikaelian lens and the fabrication technique used to realize such antennas by respecting the index law inside the lens. After that, we will study the results

of three different prototypes. The two first prototypes are standard plate Mikaelian lens antennas that will work respectively at 15 GHz and 30 GHz. The last prototype will have the thickness of the lens reduced to 0.8 mm, a dimension that is closer to what is achievable with the FPMS technology. In all the configurations, we will mainly focus on the beam steering capability of the antenna.

### 4.3.1 Pressed foam technological process

In order to synthesize the variable refracting index of the lens, we use a simple and original technological process that consists of pressing a foam (composite material) to control its relative permittivity [61]. Foam materials are basically composed of a core material that has been injected with a gas in order to make the permittivity close to the unity. The desired value of permittivity can be achieved by changing the ratio between the core material and the gas (air) by removing the amount of air within the foam. In other words, the process consists of expelling the air of the foam material by pressing it, thus increasing its density and so its relative permittivity. This process is illustrated in Figure 4.4.

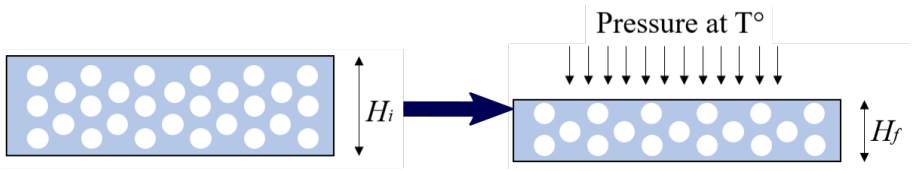


Figure 4.4 – Foam pressing technique [61]

The foam that we used is the airex PXc 245: this foam has already been used multiple times to realize lens antennas [75], [76]. The density law of the foam is plotted in Figure 4.5. The relative permittivity goes from 1.33 (initial relative permittivity of the foam) to 2.8 when all the air is expelled from the foam (only the basic polymer remains).

### 4.3.2 Antenna at 15 GHz

#### 4.3.2.1 Design

In order to design Mikaelian lens antennas, different parameters need to be fixed to obtain the wanted properties in terms of directivity and radiation patterns. One thing to note is that we will realize a plate lens. So only one slice of height $h$ of the cylinder

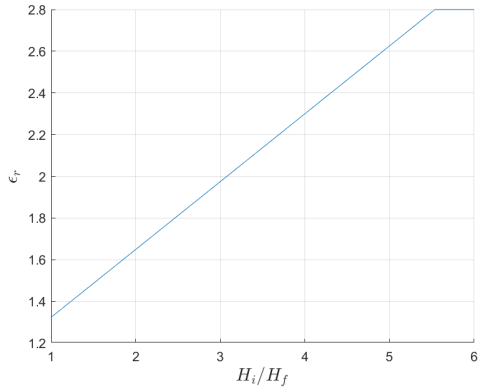


Figure 4.5 – Variation of the dielectric constant

is considered here. The lens will be placed between two parallel metallic plates. In conclusion, the focusing beam behavior, thanks to the lens, will be only effective in one principal plane (H plane). In the E-plane, the beamwidth of the radiation pattern will be relatively wide because of the limited height of the lens. The first dimension to define is the ratio $T/R$ as it establishes the index law variation. For simplicity, this ratio is fixed at $T = 2R$; it corresponds to a square lens. Figure 4.6 shows the normalized continuous law of a square lens and a discrete version with 8 steps. This discretization is not mandatory as the fabrication process could handle the realization of a continuous law. The stepped design simplifies the fabrication process, and the number of steps (8) is the chosen configuration of the active lens that will be presented in the second part of this chapter.

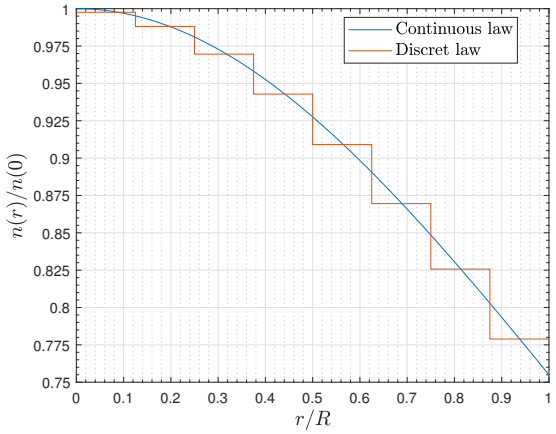


Figure 4.6 – Continuous and stepped index law of Mikaelian lens for $T = 2R$

The complete law is presented in tab 4.1, where the wanted law and the pressed foam

technological process are considered to manufacture the Mikaelian lens. It can be noticed that the value of the dielectric constant of the last stair of the law is fixed to be equivalent to the unpressed foam ($\epsilon_r$=1.32). This choice has been made in order to limit the total height of foam needed and limit the loss, as the loss of the foam increase when it is pressed.

| $r/R$ | $H_i/H_f$ | $\epsilon_r$ |
|---|---|---|
| 0.125 | 3.6 | 2.17 |
| 0.25 | 3.5 | 2.14 |
| 0.375 | 3.3 | 2.07 |
| 0.5 | 2.9 | 1.94 |
| 0.625 | 2.5 | 1.81 |
| 0.75 | 2 | 1.65 |
| 0.875 | 1.5 | 1.49 |
| 1 | 1 | 1.32 |

Table 4.1 – Characteristiocs of the lens with 8 steps and using the foam pressed technological process ($T = 2R$)

It can be noted that the dimensions are still normalized. In fact, the final size (R) only depends on the wanted directivity at a given frequency. The radius R of the lens is directly linked to the beamwidth. In order to have a good compromise between performance and size, the final dimensions of the lens are set at $T = 2R = 4\lambda_0$. It corresponds to a lens of 80 mm at 15 GHz. The final height is set to 12 mm in order to allow a good matching between the dielectric foam and the air at the output of the lens and allow good lens radiation. It means that the initial height in the center of the lens is set at 43.3 mm. In order to feed this lens, a WR62 standard waveguide is used. Figure 4.7 alongside the mobile waveguide support presents the foam profile before and after pressing. This mobile support will allow moving the WR62 waveguide behind the lens.

#### 4.3.2.2 Simulation results

All antenna designs are simulated on CST Microwave Studio. We want to study the beam steering capability of Mikaelian lenses depending on the position of the source. Fig 4.8 shows the electric field inside the lens for two different positions of the source at 15 GHz. The center position is the classical case to feed the lens, and the lens's focusing can be easily observed because a plane wave exists at the output of the lens. With the offset source (b), it can be seen that the focusing (plane wave) is achieved with a particular orientation of the wavefront plane. It means that we can achieve beam steering with this

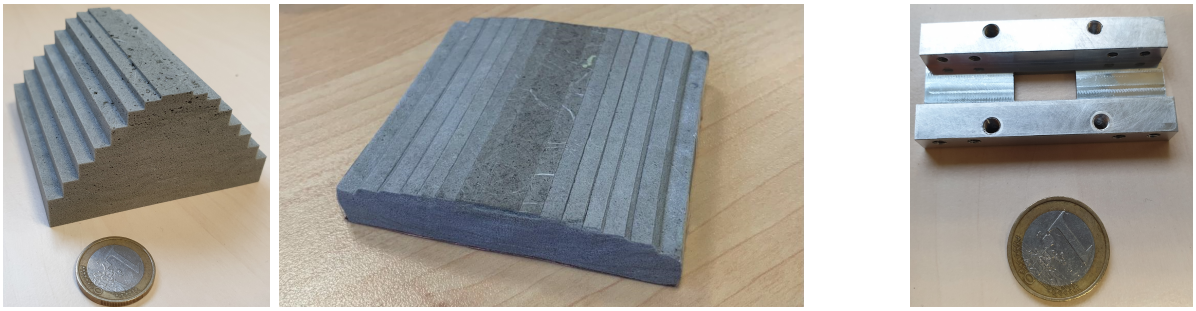

(a) (b) (c)

Figure 4.7 – Prototype: (a) foam before pressing, (b) foam after pressing, and (c) waveguide support for WR62

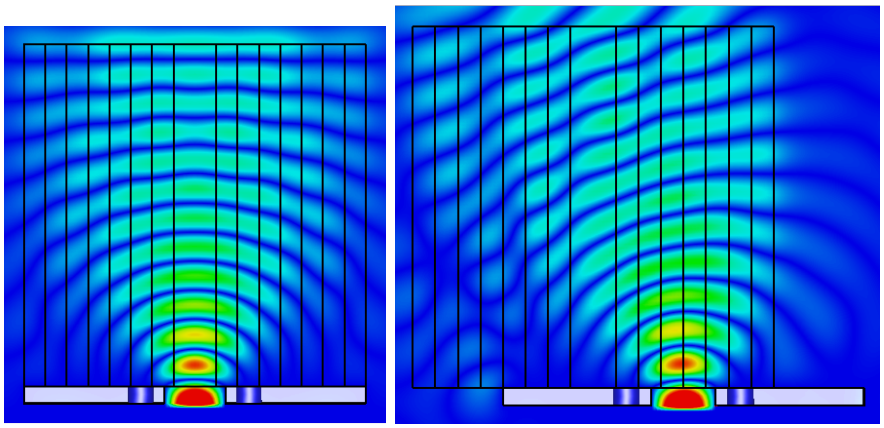

(a) (b)

Figure 4.8 – Electric field : (a)Centered waveguide, (b) Shifted waveguide (10 mm)

antenna by moving the waveguide behind the lens.

This beam-scanning capability is also demonstrated in Figure 4.9 where the radiation pattern in H-plane is plotted at 15 GHz. The source is shifted between each curve in every 5 mm. The radiation pattern at 0° is, of course, achieved for the source placed in the center position. The antenna allows a beam steering of ±35° for a source moving between $\pm 25mm$. For the center configuration, the gain is about 14.5 dBi. The beam width is about 13°, and side lobes are at −18.5 dB. The side lobe levels are linked to the angle of the beam and rise to −10.5 dB for the 35° angle.

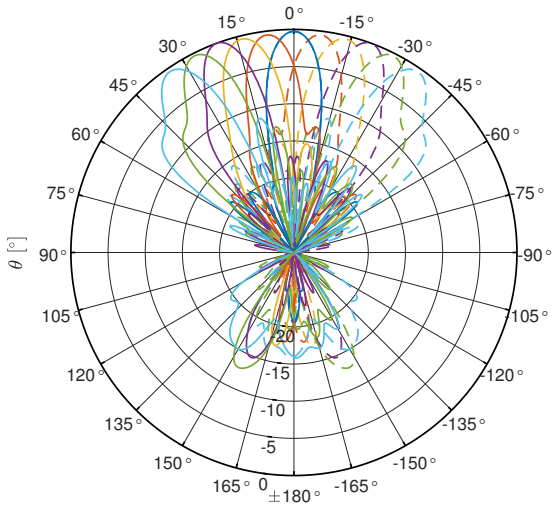


Figure 4.9 – Normalized radiation pattern at 15 GHz

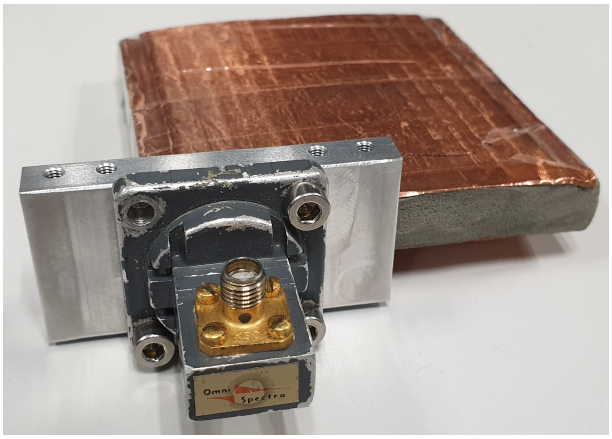

Figure 4.10 – Picture of lens at 15 GHz

#### 4.3.2.3 Measurement

After manufacturing, the lens at 15 GHz has been measured. In order to move the source easily, a removable waveguide holder is used (Figure 4.7c). Finally, Figure 4.10 shows the assembly of the antenna, including the pressed foam, the waveguide holder positioned at 25 mm from the center, and the waveguide fixed on the holder.

Figure 4.11a shows the radiation patterns of the antenna in the H-plane. The antenna's performance is in accordance with the predictions of the simulations; the obtained beam direction is ±35°. The side lobes vary between −17 dB and −10 dB. The maximum gain is 13 dBi, which is lower than the simulation value, but this difference can be explained by the fact that the simulation does not consider the foam's dielectric loss. Figure 4.11b shows

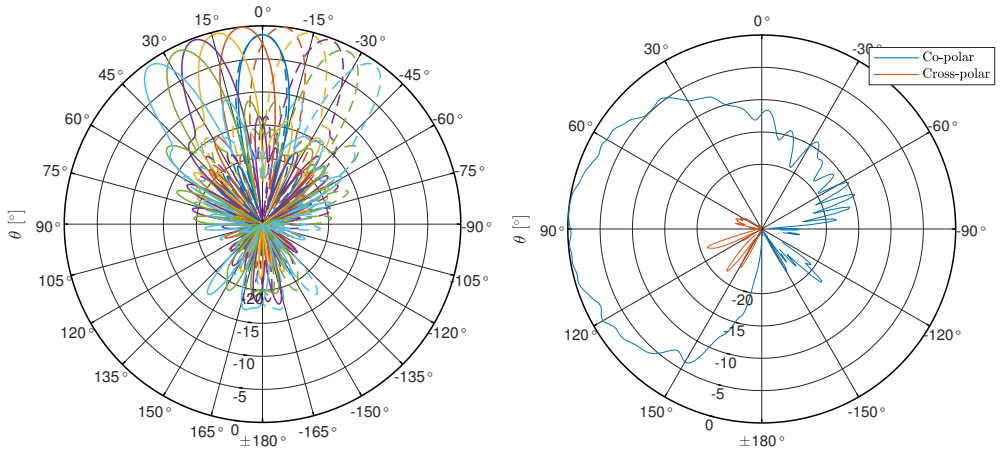


(a)

Figure 4.11 – Normalized radiation pattern: (a) H-plane and (b) E-plane

the E plane radiation pattern for an excitation in the central position. The beamwidth in this plane is about 60°.

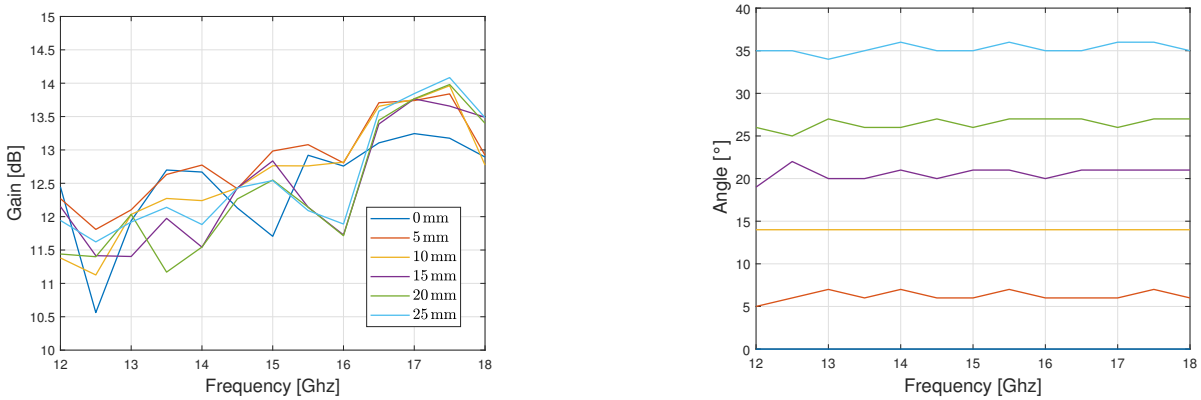


(a) (b)

Figure 4.12 – Maximum gain and beam tilt

Fig 4.12 shows the maximum gain, as well as the off-angle obtained as a function of the source position and frequency (from 12 GHz to 18 GHz). This Figure highlights the stability of the antenna between 12 GHz and 18 GHz whether it is for the variation of the maximum gain which for each given frequency is less than 2 dBi or for the different angles obtained which do not depend on the frequency.

### 4.3.3 Reconfigurability: commutable sources

The most straightforward way to achieve some degree of reconfigurability is to use commutable sources instead of moving the source physically behind the lens. In this section, we study a multi-port version of the Mikaelian lens. For a Mikaelian lens working at 15 GHz, 5 standards waveguide (WR62) sources are put behind the lens and illuminate the lens sequentially or simultaneously to show the electronic beam scanning or beam-shaping capability. The spacing between each waveguide is 16 mm. Fig 4.13a shows the radiation pattern at 15 GHzwhen the 5 waveguides excite the lens sequentially. Each excited waveguide allows the achievement of a different beam tilt angle($-43°$, $-22°$, $0°$, $22°$ and $43°$). For the 3 center configuration (2,3,4) configurations, the beam width is 12.5°, and the gain varies between 14.9 dBi and 14.3 dBi. For the 2 extreme configurations (1 and 5), the gain drop to 12.9 dBi, and the beams have high-level side lobes. Unfortunately, it is impossible to overlap (-3dB) the different tilted beams because of the size of each waveguide that is too wide.

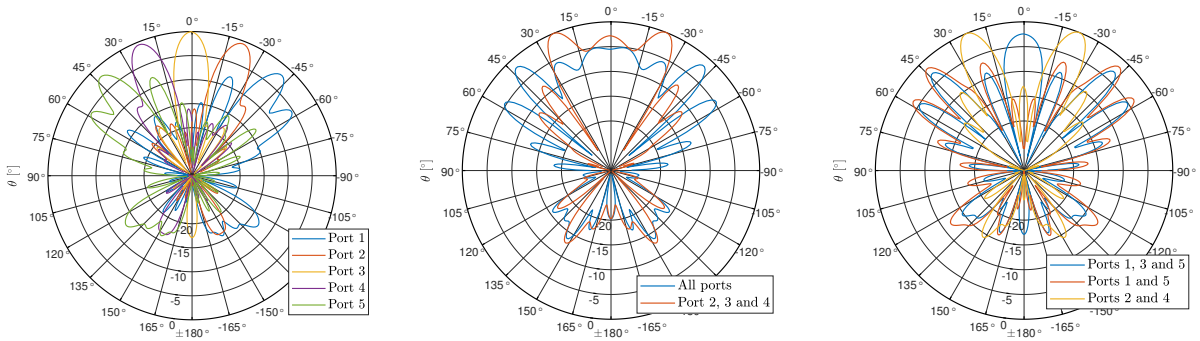


(a) (b) (c)

Figure 4.13 – Normalized gain at 15 GHz: (a) Sequential, (b) Sectorial-beam and (c) Multi-beam

Figure 4.13b shows the radiation pattern when waveguides feed the lens simultaneously with the same amplitude and phase. The goal is here to achieve a sectorial radiation pattern. When all five ports are used simultaneously, the antenna does not produce a sectorial beam due to the poor performance of configurations 1 and 5. However, for the 3 port configuration, if we tolerate the high ripple of the gain in the beamwidth, a sectorial antenna of 55° is achieved, the maximum gain is 10.6 dBi and drop to 5.1 dBi at the angles $\pm 12°$. Using non-adjacent waveguides to excite the lens, it is possible to achieve multi-beam radiation patterns. Figure 4.13c shows some examples, with 2 and 3 beam

directions of radiation patterns. The problem with this approach is that the number of beams and direction depend on the source number and their position. It means that some angles can not be achieved, and the crossover point between two adjacent beams is unsatisfactory.

#### 4.3.3.1 Solution to overlap beams with the Mikaelian lens and feeders

In order to achieve a crossover point between two beams at -3dB or to obtain flat sectorial radiation patterns with a limited ripple, it is impossible to use a classical open-ended waveguide as a feeding source because of its excessive width. The solution proposed in this section is to optimize one source with a limited size in order to put a total of 9 sources close to each other.

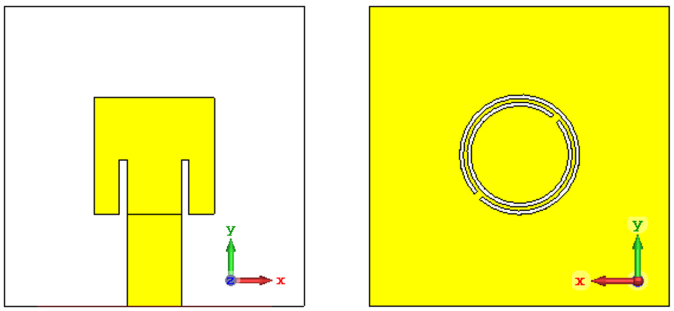


(a) (b)

Figure 4.14 – Patch antenna: (a) top and (b) ground plane

(a) (b)

Figure 4.15 – Fabricated patch antenna: (a) top and (b) ground plane

The source consists of a microstrip patch antenna combined with a Complementary

Split Ring Resonator to achieve a compact size at 17 GHz. The design of the source is presented in Figure 4.14. The patch is realized on Rogers/Duroid RT5880 with a dielectric constant of $\epsilon_r = 2.2$, and the height of the substrate is $h = 0.508$ mm. The patch is 3.2 mm × 3.1 mm. A CSRR structure of radius 1.6 mm is printed on the ground plane. Figure 4.15 shows the fabricated prototype of one patch.

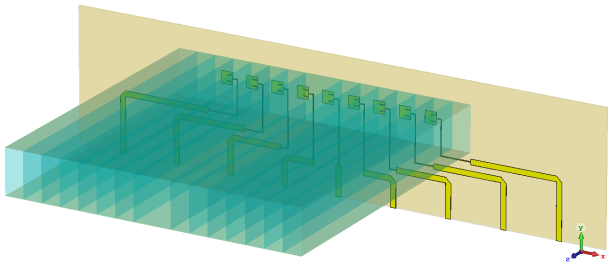

Figure 4.16 – Model of the Mikaelian lens fed by 9 patch antennas

We associate after 9 printed patches with CSRR for each one and the Mikaelian lens. It is illustrated in Figure 4.16 for the simulated complete system. In order to feed the patches and place the different coaxial connectors, long microstrip transmission lines have been added.

(a) (b)

Figure 4.17 – Fabricated antenna array: (a) top and (b) ground plane

The final prototype is presented in Figure 4.17. Figure 4.18 presents the measured normalized radiation patterns. A different beam is obtained for each patch, exiting the lens. This antenna achieved ±45° beam steering. The crossover point is less than −3 dB, demonstrating that the overlapping of beams is effective. This antenna suffers from the limitation of the Mikaelian lens concerning beam tilt capability; as such, the side lobe level increases with the scanning angle. Compared to the previous design, the side lobe levels are degraded (more than −10 dB). This phenomenon is mainly due to the presence of the feeding lines and the coupling effect between the different sources exciting the lens.

The feeding line is also responsible for the non-symmetry between left and right radiation patterns.

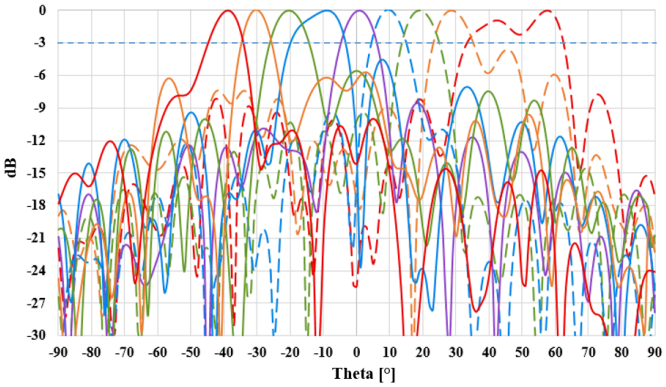


Figure 4.18 – Measured normalized radiation pattern at 17.5 GHz

This antenna is still passive, but thanks to the used PCB technology, the antenna can easily be modified in order to achieve electronic beam-steering. The idea is to add active switches into the feeding line network to excite the nine different sources independently.

### 4.3.4 Mikaelian lens at 30 GHz

The final objective of the research work concerning the Mikaelian lens is to design reconfigurable lenses using the FPMS concept with active Unit cells. The future FPMS lens is aimed to work between 25 GHz to 30 GHz. Before manufacturing the final prototype with FPMS, two passive lenses at 30 GHz have been studied using the precedent press foam technological process to validate the concept of reconfigurability. The only difference between these two lenses is the final height of the lens. Indeed, the first one will have a classical height (same ratio) as the precedent lens working at 15 GHz while the second lens will have a thin height close to the one used with the FPMS substrate. The two lenses use the same index law as for the 15 GHz concept; they also keep the same size proportion: $T = 2R = 4\lambda_0$. It corresponds to lenses of 40 mm width at 30 GHz. As mentioned, the key difference between the two lenses is their height: one is 6 mm and will be referred to as a "high-profile lens," and the second one is 0.8 mm thick and will be referred to as "low-profile lens."

The high-profile lens should achieve the same performance as the first lens (15 GHz). The low profile lens, however, cannot directly radiate efficiently because of its very small height. So in order to match the end of the lens to radiate well, a focusing device is needed. Another difficulty for the low-profile lens is that a standard waveguide cannot directly feed it. Therefore, we need to design a transition that goes from the standard height of a classical WR28 waveguide to less than 0.8 mm (height of the low profile lens).

The prototype of low-profile lens is presented in Figure 4.19.In order to feed the low-profile lens, an open-ended-ridged waveguide is optimized and fabricated (figure 4.19b); it consists in designing a waveguide transition from 3.55 mm (the height of a classical WR28 waveguide) to 0.6 mm (less than the height of the low-profile lens). A total of five symmetric stairs of 0.375 mm height and 2.5 mm long are used. For the focusing design, the idea is to match the final height of the lens 0.8 mm to the air . The final aperture is about 9.15 mm. The height change is linear, and the distance between the edge of the lens and the aperture is about 38 mm in all directions. The different dimensions have been tuned in order to have a good compromise between the size of the structure and the final matching. That means that the low profile lens with the focusing part allows having a narrower beam in E-plane even if it is always relatively wide. The structure is composed of two identical parts that are fixed together with two screws.

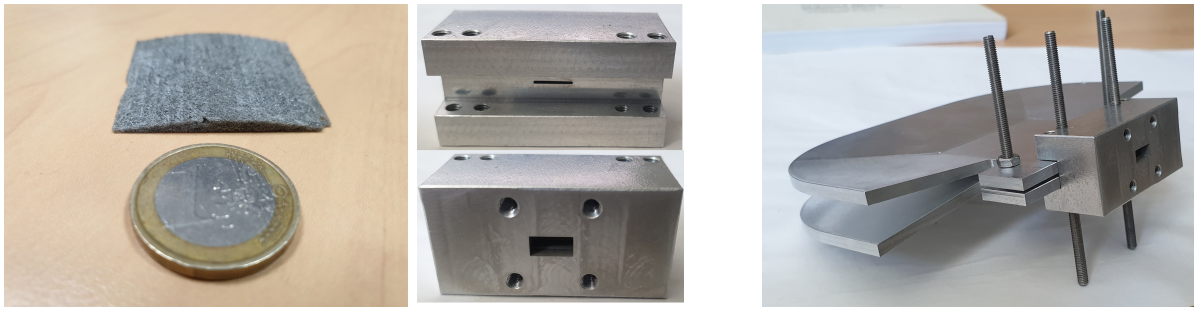

(a) (b) (c)

Figure 4.19 – Prototype: (a) foam before pressing, (b) ridged waveguide support for WR28, and (c) final prototype

#### 4.3.4.1 Simulations and measurement

The two antennas are simulated on CST Microwave Studio. We will study the beam steering capability of these antennas depending on the position of the source.

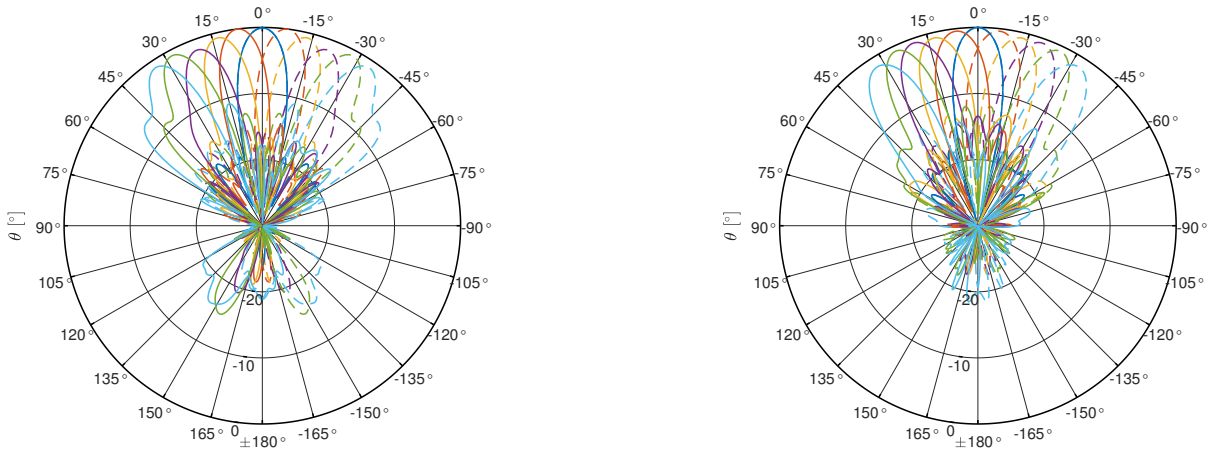


(a) (b)

Figure 4.20 – Normalized radiating pattern at 30 GHz:(a) high-profile lens and (b) 30 GHz low profile-lens

Figure 4.20 shows the radiation pattern in H-plane for both antennas. The source is moved between each curve by 2.5 mm. A total shift of ±12.5 mm permits to achieve ±35° angle beam-steering. For the center configuration, the gain is about 15.5 dBi for the high-profile lens and 17 dBi for the low-profile lens. Both antennas show a beam width of about 13° and side lobes at −18.5 dB. The side lobe levels are linked to the angle of the beam and increased to −10.5 dB for the 35° angle. Thanks to the focusing device, the

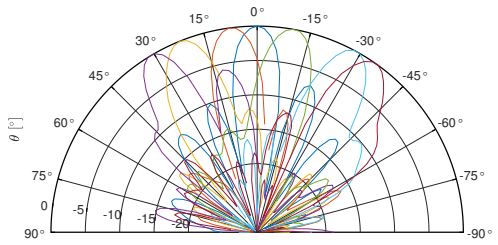


Figure 4.21 – Measured normalized radiating pattern at 30 GHz

low-profile lens has improved performance compared to the high-profile one. Figure 4.21 shows the measured radiation pattern of the low-profile lens. The antenna's performance is in accordance with the predictions of the simulations.

A quasi-equivalent concept for the focusing part will be associated with the active lens based on FPMS and presented in the following section.

## 4.4 Reconfigurable Mikaelian lens using FPMS

This section aims to use the FPMS technology to fabricate a reconfigurable lens antenna around 25-30 GHz.

We have seen in the previous section that the Mikaelian lens can permit to achieve beam steering by moving the excitation source behind the lens. In the case of the FPMS lens antenna, the source will be put at one central position, and the beam steering capability will come from the reconfigurability of the lens by electronically varying the index law. The simple idea is to shift the lens's index law laterally in front of the excitation source.

This section will start with the design of the UC and the synthesis of the refracting index. After that, a complete FPMS board will be presented and studied.

### 4.4.1 Unit cell

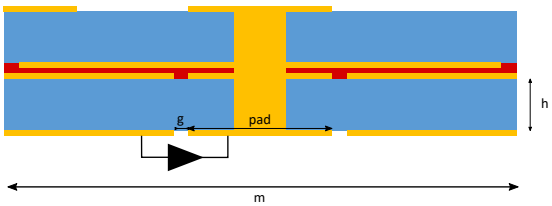


Figure 4.22 – Unit cell

In this part, we will discuss the design of a FPMS unit cell that can be used to synthesize the refracting index of an inhomogeneous lens. For the design of an inhomogeneous lens, the most crucial property to achieve with the UC is to have a high variation of positive dielectric constant at a given frequency. In this case, the property to achieve a negative dielectric constant is unnecessary. According to section 2.2, the property of controlling the value of the positive dielectric constant appears at two different places, in area 1 before the resonant frequency of the UC and in area 4 after the resonant frequency when the dielectric constant becomes positive again.

The constraint for the design of the FPMS lens Unit Cell is linked to the lens design. We want to limit the number of cells for a given size of the lens in order to simplify the DC bias control of the cells. The height of the cell (and so of the artificial substrate) needs to be adjusted because we want the final FPMS lens to be able to radiate "directly" in the air. The height of the UC for circuit application is 0.127 mm, and it has been demonstrated previously that a low-profile lens needs a matching device to achieve the same performance as a thicker lens. The problem with increasing the height of the unit cell is that this will reduce the cell's resonant frequency. This problem can be mitigated using the cell after the resonant frequency (area 4). A compromise is to design the FPMS lens with a 0.8 mm lens thickness.

The design used for lens application is quite the same as the final UC presented in 2.3.2.2, only with size optimization (thickness). Figure 4.23 presents the parameters (dielectric constant, magnetic constant, and refractive index) of a 2.5 mm UC with a substrate height of 0.787 mm. The resonant frequency of the cell varies from 8 GHz to 16 GHz depending on the capacitance value (varactor diode). This UC could be used before this resonant frequency between 0 GHz to 15 GHz in order to synthesize a refractive index, but we want to use such a UC around 25-30 GHz. Nevertheless, if this cell is used after the resonance frequency and, more precisely, after the negative dielectric zone (after 25 GHz), the dimension and the height of the UC will be suitable because the results show that it is possible to vary the refractive with acceptable values up to 1.4.

This cell will be used after 25 GHz and Figure 4.24 presents the possible variation of the UC parameters at different frequencies, depending on the capacitance values. It can be seen that the dielectric constant increases with the increase of the capacitance. The magnetic constant, however, increases with the reduction of the capacitance. The most important parameter for lens application is the refractive index which increases with the capacitance value. It can be seen that the possible values and variation depend on the

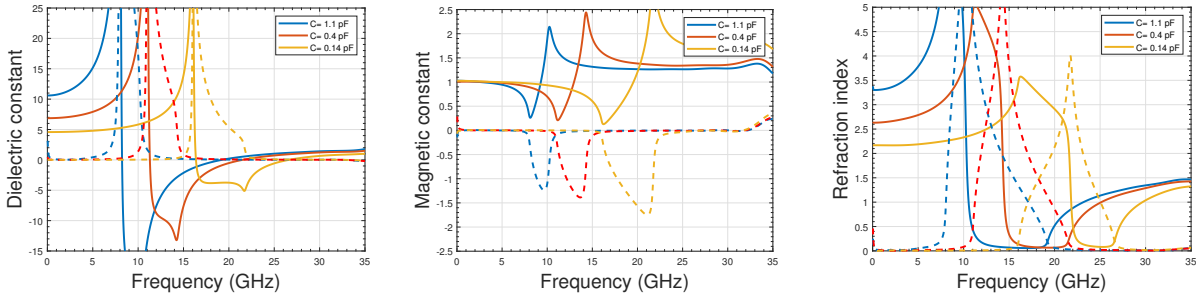


(a) (b) (c)

Figure 4.23 – UC parameters for 3 values of capacitance with real part (solid line) and imaginary part (dashed line)

chosen frequency.

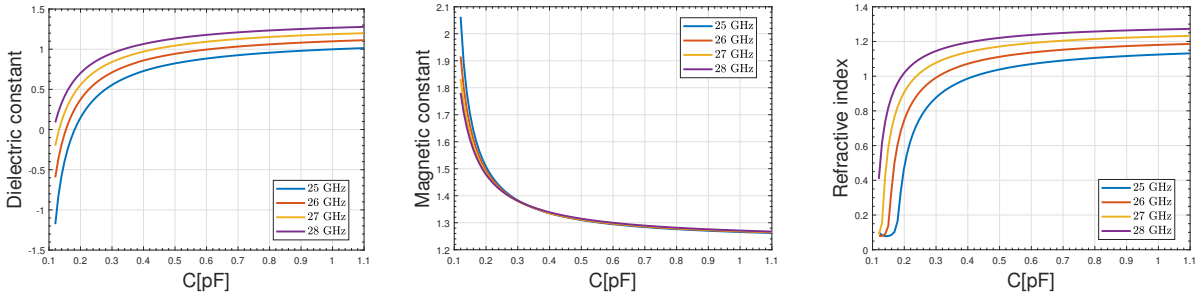


(a) (b) (c)

Figure 4.24 – UC parameters for 4 different frequencies

## 4.4.2 Index law and simulation of lens

### 4.4.2.1 Index law

In order to create the law of the FPMS lens, we have all the information needed: the discretized Mikaelian index law (Fig 4.6) and the variation of the reflective index at a given frequency (Fig 4.24c). The tab 4.2 presents a Mikaelian index law associating the normalized refractive index to the capacitance at 25 GHz.

This law will be used to create a $16 \times 16$ FPMS structure using eight different capacitance values. The most important thing to understand about this synthesis is that it depends on the frequency. So if the frequency is modified, the law should be adjusted. With the given cell, it is possible to realize the given normalized law up to 28.3 GHz. The

| $r/R$ | $n_r/n_0$ | $n_r$ | $\epsilon_r$ | $\mu_r$ | $C(pF)$ |
|---|---|---|---|---|---|
| 0.125 | 0.9976 | 1.1313 | 1.0139 | 1.2620 | 1.1 |
| 0.25 | 0.9881 | 1.1206 | 0.9902 | 1.2678 | 0.951 |
| 0.375 | 0.9696 | 1.0996 | 0.9450 | 1.2790 | 0.760 |
| 0.5 | 0.9428 | 1.0692 | 0.8827 | 1.2947 | 0.598 |
| 0.625 | 0.909 | 1.0309 | 0.8086 | 1.3138 | 0.481 |
| 0.75 | 0.8695 | 0.9861 | 0.7278 | 1.3351 | 0.400 |
| 0.875 | 0.8257 | 0.9363 | 0.6453 | 1.3576 | 0.344 |
| 1 | 0.7789 | 0.8833 | 0.5647 | 1.3801 | 0.304 |

Table 4.2 – Mikealian law for a FPMS lens at 25 GHz

adjustment of the law is needed if we want to have a "perfect" law for each frequency. This means that a law made for one precise frequency should still work for close frequency. After 28.3 GHz, the range of possible refractive index values (maximum possible value/minimum possible value) will be insufficient.

#### 4.4.2.2 Simulation technique

As for the circuit FPMS, simulation time is a concern. The most direct way is to simulate the complete FPMS structure. However, this solution can be time-consuming, especially when external elements to the FPMS need to be considered, like the different transitions (microstrip or CPWG to SIW transitions).

One way to simulate the structure for a lot number of configurations (by changing the index law) is to replace the unit cell with an equivalent dielectric material, as we know the different values of the $\epsilon_r$ and $\mu_r$ of each cell precisely depending of the capacitance. The only thing to remember is that this technique only works for a given frequency. So the impact of the frequency on the radiation pattern can only be studied if we simulate an equivalent FPMS for each frequency which takes a lot of design time. In the following subsection, with this simulation technique, we are able to shift the index law in order to steer the beam in different directions, always with a centered excitation source.

### 4.4.3 Proof of concept of reconfigurability

The first reconfigurability we want to explore is the possibility of obtaining beam scanning capability with the antenna. To achieve beam scanning with a FPMS lens instead of moving the source, we have to move the law. With a classical Mikaelian lens

(without any reconfigurability), the main lobe direction can be modified by moving the primary source (waveguide) behind the lens. But for this project, we use controlled UC in the FPMS to design this lens. So by changing the polarization of the varactor diodes of the UC, it is possible to move the law artificially and so to obtain beam scanning or beam shaping capability without any motion of the primary source. One important thing to note about these preliminary simulations is that they do not consider a realistic (prototype) case that would require the implementation of an output focusing system for the lens to radiate correctly, nor a real excitation via the addition of a transition. For these preliminary simulations, OPEN boundary conditions are applied at the output and on the edge of the lens, and a theoretical waveguide excites the lens. These first results are presented to prove the concept of reconfigurable index law in order to steer the beam of the lens.

#### 4.4.3.1 Centered law

The first configuration that needs to be explored is the simplest one: the index law is centered in regard to the FPMS. The law that we used is the one presented in the table 4.2. Figure 4.25a shows the radiation pattern in the H-plane of this center configuration at 25 GHz. In this configuration, the beam width is of 19.6° and side lobe level at −10.7 dB. Figure 4.25b shows the electric field inside the lens. As expected for the center configuration, the FPMS lens results are similar to the passive one.

#### 4.4.3.2 Shifted law

In order to achieve beam steering capability with this FPMS design, the idea is to shift the law laterally. This principle is illustrated in Figure 4.26. When the center of the refractive law is modified, the raws at the opposite of the move have unassigned values. Different approaches to define the values of the unassigned rows can be used:

1. The law can be considered periodic, with the center of the law as the center of the periodicity. This approach is illustrated in Figure 4.26b.
2. The unassigned row can be set to the final step of the law.
3. The law can be extended; in this case, we consider that $r$ in the Mikaelian law formula (equation 4.1) can go beyond 1. This approach is illustrated in Figure 4.26c.

The first and second approaches have the advantage of keeping low the number of different values needed to synthesize the lens. Only eight values are needed. The last

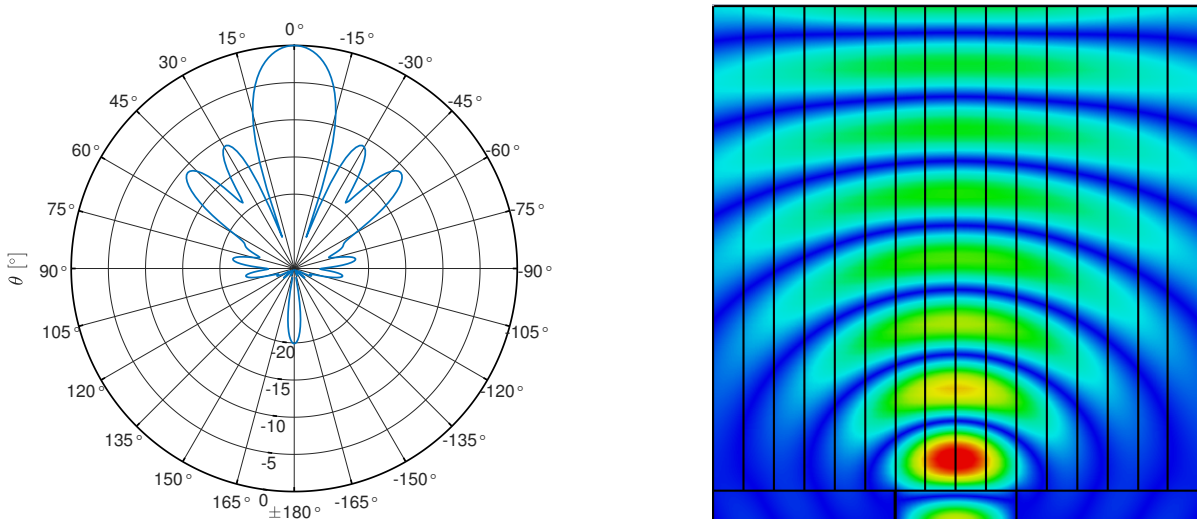


(a) (b)

Figure 4.25 – Center law at 25 GHz: (a) Normalized radiation pattern and (b) Electric field

approach should be the one that gives the best performance, but it increases the number of parameters (more different voltage/capacitance), and UC needs to have the capacity to produce the refractive value needed.

Figure 4.27a shows the different steering angles achieved by moving the law in a periodic configuration. It can be seen that moving the law by one row allows a beam steering of 7°/8°. However, the performance starts to decrease after a shift of three rows. The maximum angle achievable is 33° and appears for the five rows shift configuration. Figure 4.27b corresponds to the case we extend the law. Meaning that the eight rows shift configuration needs sixteen different values of refractive index (equivalent to capacitance voltages). It can be observed that for the extreme angle ±30°, the lens performs better than in the first approach due to a lower side lobes level. The beam steering per shifted row decreases with the number of rows shifted. For example, the beam steering direction between the case with the center law and the case with the first shifted row is about 8°, but it is only 3° for the last shifted configurations (6 and 7).

Figure 4.28 shows the electric field inside the lens for the periodic approach and the extended approach for a five rows shift. It can be seen that the extended version gives a better plane wave at the output of the lens.

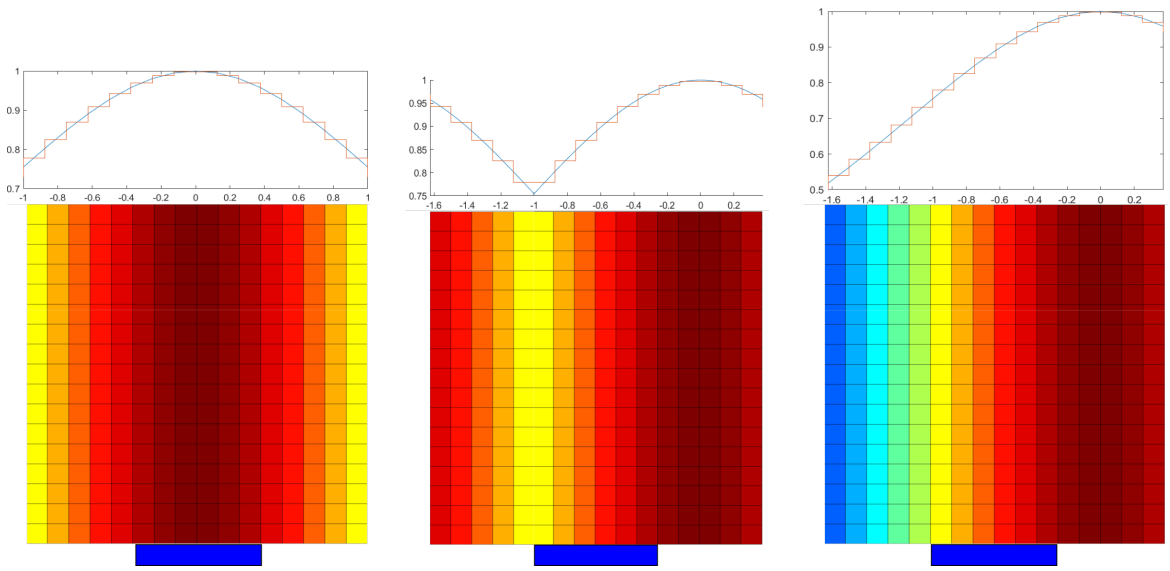

(a) (b) (c)

Figure 4.26 – Representation of law inside the lens: (a) centered law, (b) 5 row shifted with the periodicity of the law, (c) 5 row shifted law with an extended law

### 4.4.4 Prototype

In order to realize a realistic prototype, some design issues need to be addressed: the different transitions for the feeding part, the metallic output structure for focusing, to improve the radiation of the structure, and the DC biasing aspect.

#### 4.4.4.1 DC biasing

In order to achieve the maximum possible reconfigurability, each cell of the FPMS lens should have an independent DC biasing. This is what is planned for the FPMS circuit design (section 2.4). However, some compromises have been made to reduce the cost and fabrication complexity of the FPMS lens. As a result, we have reduced the two hundred and fifty-six needed independent biasing to sixteen. It corresponds to one biasing line per FPMS row. The final biasing network is illustrated in Figure 4.31a. Sixteen biasing lines are present, and each cell is connected to these lines through an inductance in order to isolate the DC signal from the high-frequency signal.

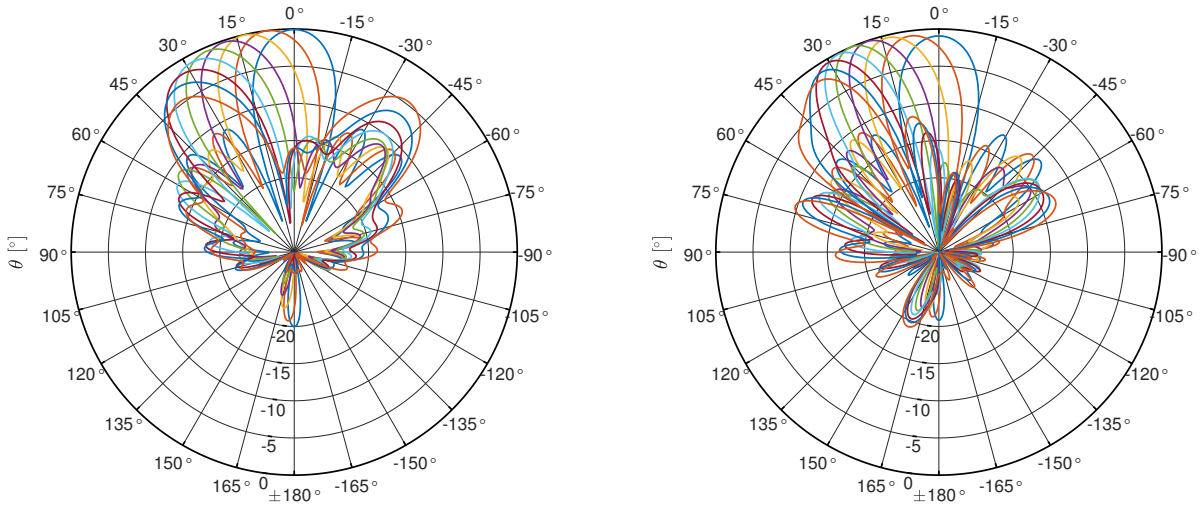


(a) (b)

Figure 4.27 – Radiation pattern at 25 GHz: (a) periodic configuration, (b) extend configuration

#### 4.4.4.2 Transition CPWG to SIW to FPMS

In order to feed the FPMS lens structure, we use the same idea as for FPMS reconfigurable circuit presented in Section 2.4.3.2. Again, a SIW waveguide will feed the FPMS lens, but a transition is needed between the connector and the SIW. This time as the substrate height is more important in the lens antenna design, we will design a transition that goes from a CPWG (grounded coplanar waveguide) to a SIW. The transition is shown in Figure 4.31c and 4.31d.

#### 4.4.4.3 Focusing device

Due to the low profile of the lens (0.787 mm), as it has been mentioned previously, a focusing device is needed at the output of the lens to improve its radiation. This device will follow the same concept as the one presented in section 4.3.4. Figure 4.29 presents the 3D model of this metallic device alongside an actual photo of the realized piece thanks to the numerical milling machine in IETR.

One problem appeared during the design and association of this device with the FPMS board that needed to do some adjustments. In fact, the focusing device needs to be in contact with the inner parallel plate of the FPMS (it corresponds to the metallic face of the first substrate). To ensure this contact, we need to extend the parallel plate outside the

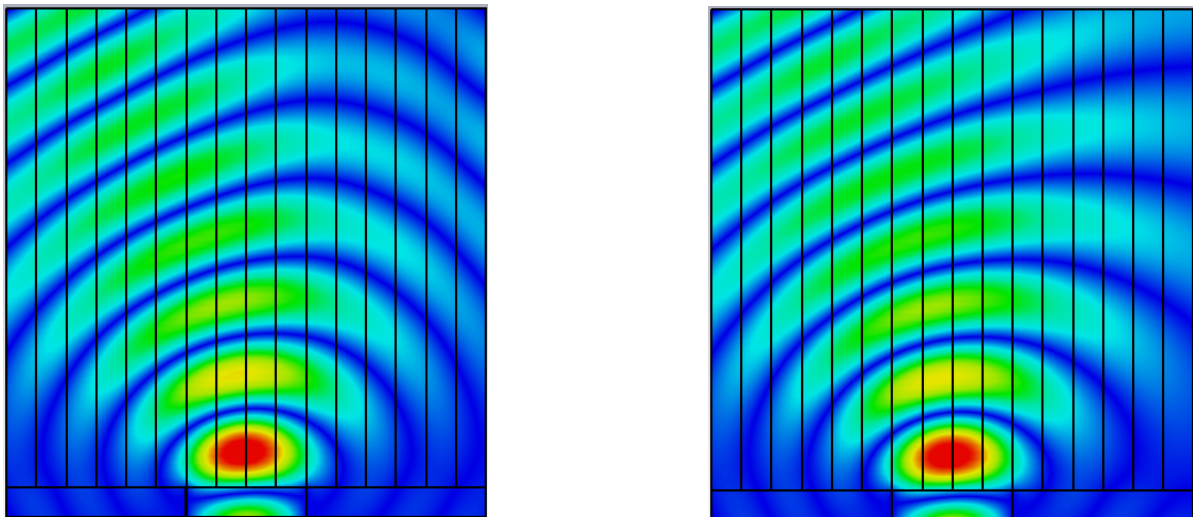

(a) (b)

Figure 4.28 – Electric field for a 5-row law shift at 25 GHz: (a) periodic approach, and (b) extend approach

FPMS. The problem is that the extension of the parallel plate creates a layer of reflection. This reflection can be explained by looking at the different values of the refractive index:

1. the refractive index of the basic dielectric is 1.48 (Rogers/Duroid RT5880)
2. inside the FPMS lens, the artificial refractive index varies between 1.3 and less than 1 (at 25 GHz)
3. the refractive index of the air is 1

The thing to note is that a transition between the FPMS and the air has less reflection than a transition that goes through the basic dielectric substrate. The effect of the dielectric

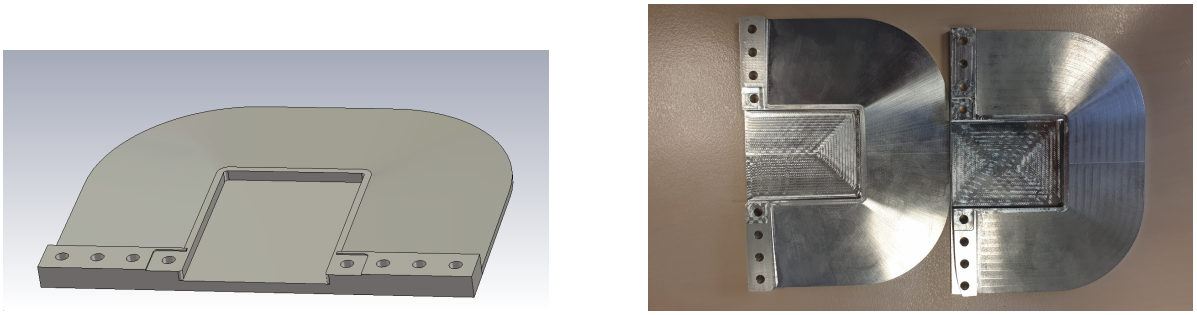

(a) (b)

Figure 4.29 – Focussing device: (a) 3D model and (b) realize pieces

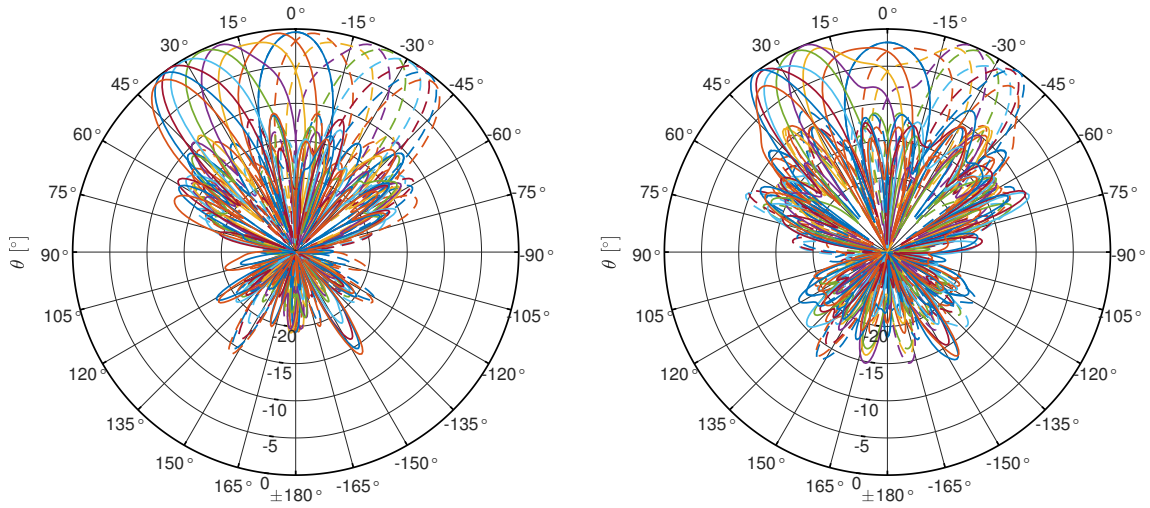


(a) (b)

Figure 4.30 – Radiation pattern at 25 GHz for 8 rows shift: (a) without the dielectric slab, (b) with the dielectric slab

slab on the radiation pattern is illustrated in Figure 4.30. Without the extended dielectric slab, the performance of the antenna is good. We achieve ±40° of beam steering, the gain varies from 14.5 dBi to 13.2 dBi with a beam width about 18° for the center law configuration. In the E plane, the beam width is around 60° for all the configurations. However, when the dielectric slab is extended outside the structure, it drastically affects the shape of the beam with a decrease in performance. The dielectric slab mainly affects the first case of shifted rows (center law to 3 shifted rows). The most notable effects are a lower gain and a wider beam width.

On the brighter side, this unwanted perturbation due to the the extended dielectric slab could be compensated by adjusting the law or by moving in frequency (the global refractive index increases with the frequency).

#### 4.4.4.4 Complete design

The complete design is shown in Figure 4.32. The complete structure has been simulated with CST Microwave Studio. In this simulation, all added designs have been taken into account: the CPWG-SIW-FPMS transition, the final focusing device with the extended dielectric slab, the DC biasing lines, the decoupling inductance, and the loss of the varactor diode.

Figure 4.33 shows the radiation pattern in the H-plane for different law configurations

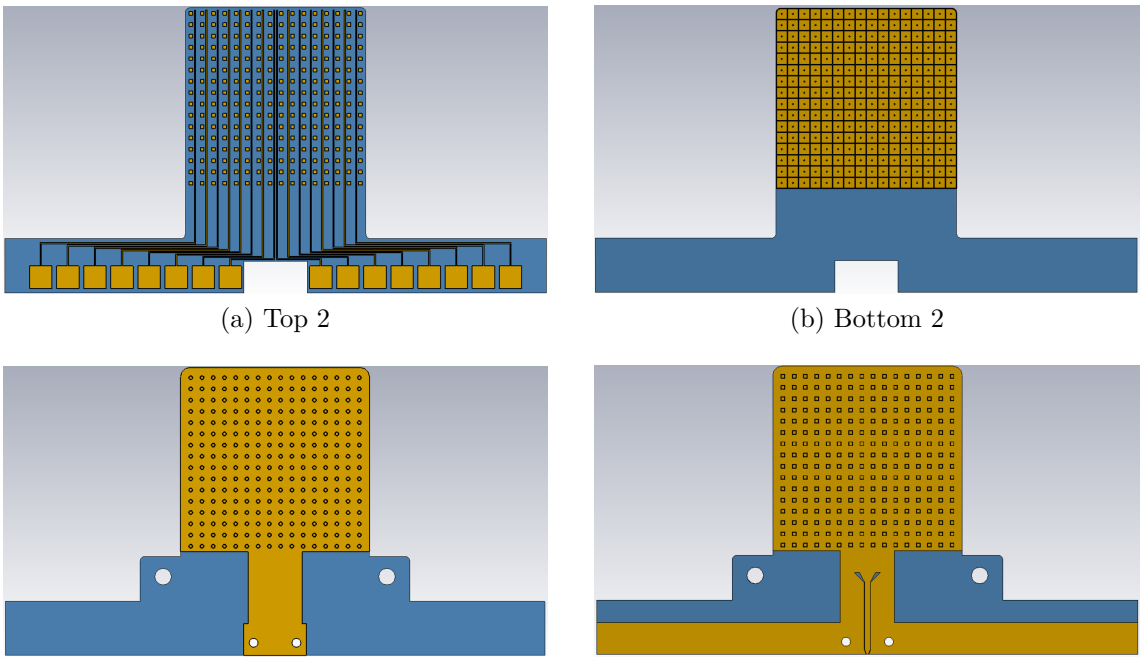

(a) Top 2 (b) Bottom 2

(c) Top 1 (d) GND

Figure 4.31 – The different metallic layers of the final design

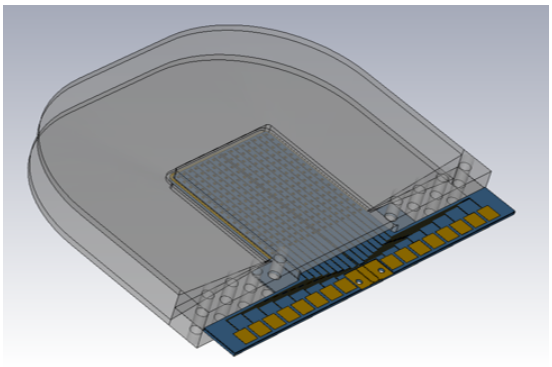

Figure 4.32 – Final design of the FPMS lens

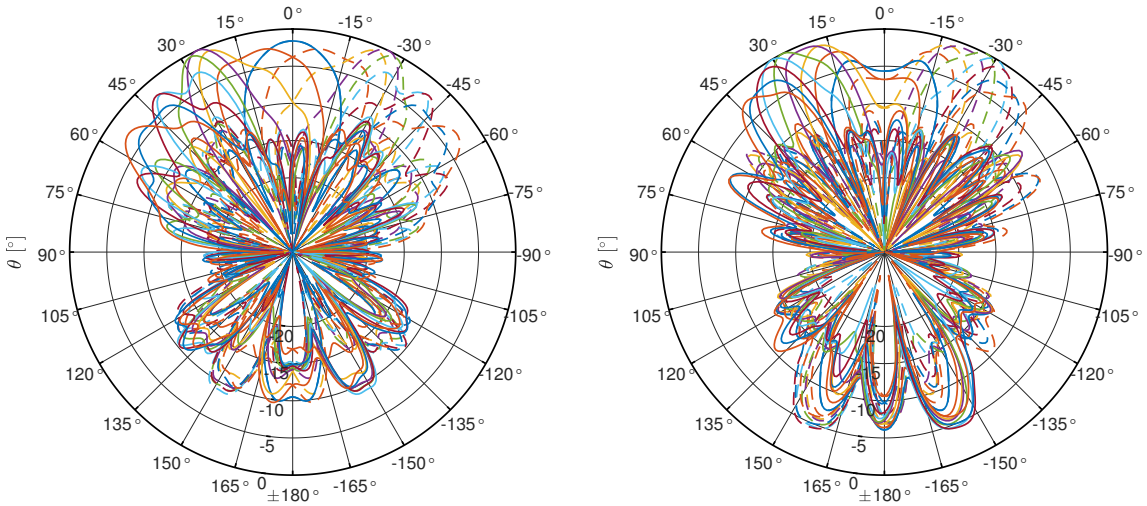


(a) (b)

Figure 4.33 – Radiation pattern for 8 rows shift: (a) 25 GHz, (b) 26 GHz

at 25 GHz and 26 GHz. At 25 GHz, the maximum gain is at 9.6 dBi and appears for the case where four rows are shifted. The beam steering angle in this configuration is 25°.

Up to the configuration with six shifted rows, the shape of the beam is quite similar to the result obtained with the dielectric simulation when the extended dielectric slab is considered (see Figure 4.30b). However, for the upper configurations (more than six shifted rows), some unexpected results can be observed, especially for the eight shifted rows configuration that achieves a beam angle of 54° for a gain of 6.8 dBi.

In this simulation, contrary to the simulation with equivalent dielectric slabs (without varactor diodes), the frequency effect can be studied. As mentioned previously, during the UC study, the refractive index value depends on the value of capacitance and frequency. As such, the synthesized law is created at one given frequency. In this case, the law has been synthesized at 25 GHz. It means that the behavior of the antenna will change with the frequency. One example is given at 26 GHz (Figure 4.33b). In this case, the antenna still achieves beam steering, but the performance with the centered law configuration is degraded. In order to improve this configuration, the simplest way is to adjust the lens law to the frequency.

Another problem with this final design is the increase in the backside radiation level. But, again, it is the result of the different fabrication choices and the nature of the UC. Each UC is composed of numerous slots that can radiate at 25 GHz. The cumulative radiation of all the UC is trapped inside a cavity created by the focusing structure that

is opened in the rear of the antenna. So all the leakage from the UC is concentrated at the rear of the antenna, leading to high backside radiation. At the start, the cavity was made in order to protect the lumped elements (inductance and diodes).

Figure 4.34 presents the photo of the realized prototype (Lithos company) before gluing the lumped elements (inductance and varactor diodes). Figure 4.34 (a) and (b) show the two observable faces (Top 2 and GND), and (c) shows the assembling of the FPMS Lens and the focusing device.

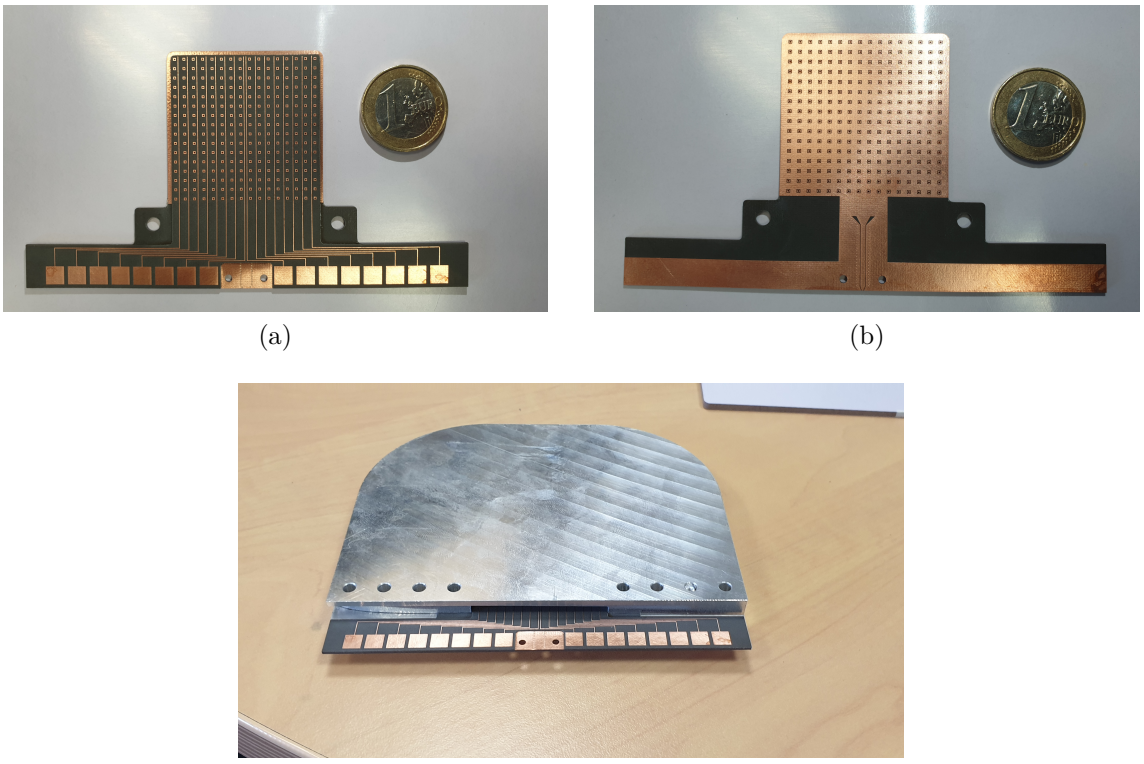

(a) (b)

(c)

Figure 4.34 – Picture of the FPMS Lens: (a) Top 2, (b) GND, and (c) assembling

The assembling of the board for varactor diodes and inductances has been done by the French company Voltakap. The assembling (Figure 4.35) is done using ROHS process (double refusion).

### 4.4.5 Measurement

It took more than 8 months to build the prototype, including producing the multilayer PCB (Lithos company) and assembling the diodes and inductors (Voltakap company).

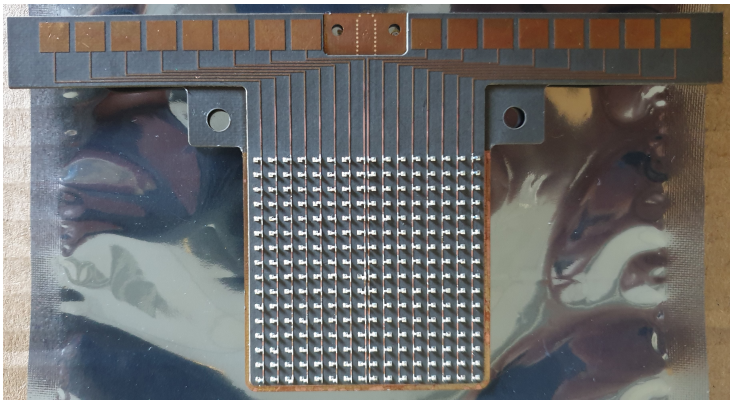

(a)

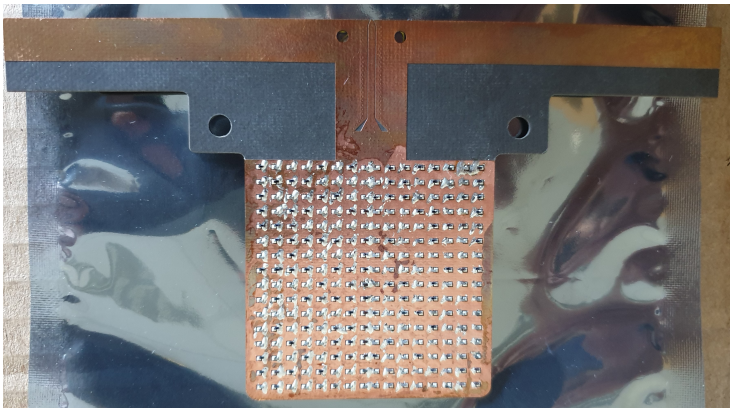

(b)

Figure 4.35 – Picture of the FPMS Lens with diodes and inductances: (a) Top 2, (b) GND and

## 4.5 Conclusion

In conclusion, this chapter has presented a new approach to designing antennas using the FPMS technology. By moving from a 1D FPMS antenna to a 2D FPMS approach, the potential for designing more complex and sophisticated antennas has been demonstrated. Furthermore, the use of inhomogeneous lens antennas has been introduced, with a focus on the Mikaelian lens. The chapter is divided into two parts, with the first study for a passive Mikaelian lens and the second exploring the use of FPMS technology to synthesize and reconfigure a Mikaelian lens for beam steering. As a proof concept, the FPMS lens technology shows great potential. In this section, we wanted to demonstrate that the FPMS's ability to control the material's dielectric property can be used to synthesize an inhomogeneous lens antenna. This research has the potential to open up new possibilities

for antenna design engineering and contribute to the development of advanced wireless communication systems.

# Conclusion

This thesis has been focused on the Field Programmable Microwave Substrate (FPMS) technology. The FPMS is a structure composed of a significant number of programmable unit cells. Depending on the bias voltage of each unit cell, their dielectric constants can be controlled, and most importantly can be switched between positive and negative dielectric constants. This allows the realization of a programmable slab waveguide with a positive dielectric constant in the center and a negative dielectric constant on the side. In this thesis, 3 topics have been developed using FPMS technology. First the development of a new unit cell and associated FPMS in X-band. Multiple circuits have been demonstrated using the new FPMS: filters, dividers, and phase-shifters. The new board under fabrication will allow a fine-tuning of a $16 \times 16$ UC FPMS, as each UC will have an independent and controllable biasing. In other words, the number of possible configurations is infinite, this is why an analytical model or at least an equivalent circuit model is important. It will allow us to simulate and optimize a large number of functions. In the context of the ANR/NSERC project, this analytical model has been transferred to XLIM laboratory to be used for their optimization algorithm in order to design reconfigurable filters or circuits with a high level of tunability.

Secondly, a demonstration of the implementation of an electronically reconfigurable leaky wave antenna has been demonstrated. Here a HMSIW structure is associated with a line of unit cells. By controlling the bias of the UC, the main beam direction can be steered at one frequency. It allows also to have a fixed beam direction for a relatively wide frequency bandwidth.

Lastly the development of a FPMS lens antenna has been shown. Combining the FPMS technology with inhomogeneous lens theories, a reconfigurable lens antenna has been developed. Complex prototypes have been manufactured and will be measured in the next weeks.

These 3 parts can be studied independently as the only real common point is the use of the FPMS technology. But the final idea behind this technology is the development of a structure that can be programmed to do any high-frequency function. For now, antenna and circuit applications are separated for ease of fabrication and testing. It is important

to note that at some point during this thesis, the idea was to create a board that can do both circuit and lens antenna applications. For this reason, most of the dimensions are similar for both FPMS circuit and lens. In fact, the only change between the two is the substrate height and the external layout (feeding part, flange for the antenna).

# BIBLIOGRAPHY


[1] N. Jess, B. A. Syrett, and L. Roy, « The Field-Programmable Microwave Substrate », *IEEE Transactions on Microwave Theory and Techniques*, vol. 64, *11*, pp. 3469–3482, Nov. 2016, ISSN: 1557-9670. DOI: 10.1109/TMTT.2016.2604315.

[2] Q. Li and S. Xiao, « Reconfigurable Voltage Controlled Single-Band and Multiband Bandstop Filters With High Selectivity and Wide Tuning Range », *IEEE Transactions on Circuits and Systems II: Express Briefs*, vol. 69, *6*, pp. 2702–2706, Jun. 2022, ISSN: 1558-3791. DOI: 10.1109/TCSII.2022.3151076.

[3] M. Fan, K. Song, and Y. Fan, « Reconfigurable Low-Pass Filter With Sharp Roll-Off and Wide Tuning Range », *IEEE Microwave and Wireless Components Letters*, vol. 30, *7*, pp. 649–652, Jul. 2020, ISSN: 1531-1309, 1558-1764. DOI: 10.1109/LMWC.2020.2997099.

[4] S. Kingsly, M. Kanagasabai, G. N. A. Mohammed, *et al.*, « Bandwidth reconfigurable microwave filter using stepped impedance c-shaped resonator », *Microwave and Optical Technology Letters*, vol. 63, *2*, pp. 432–436, Feb. 2021, ISSN: 0895-2477, 1098-2760. DOI: 10.1002/mop.32616.

[5] M. Wang, F. Lin, and M. Rais-Zadeh, « An X-band reconfigurable bandpass filter using phase change RF switches », *in 2016 IEEE 16th Topical Meeting on Silicon Monolithic Integrated Circuits in RF Systems (SiRF)*, Austin, TX, USA: IEEE, Jan. 2016, pp. 38–41, ISBN: 978-1-5090-1688-4. DOI: 10.1109/SIRF.2016.7445462.

[6] D. Bouyge, A. Crunteanu, J.-C. Orlianges, *et al.*, « Reconfigurable bandpass filter based on split ring resonators and vanadium dioxide (VO2) microwave switches », *in 2009 Asia Pacific Microwave Conference*, Singapore, Singapore: IEEE, Dec. 2009, pp. 2332–2335, ISBN: 978-1-4244-2801-4. DOI: 10.1109/APMC.2009.5385450.

[7] S. Yang, W. Li, M. Vaseem, and A. Shamim, « Fully Printed VO $_2$ Switch Based Flexible and Reconfigurable Filter », *in 2020 IEEE/MTT-S International Microwave Symposium (IMS)*, Los Angeles, CA, USA: IEEE, Aug. 2020, pp. 49–52, ISBN: 978-1-72816-815-9. DOI: 10.1109/IMS30576.2020.9224095.

[8] A. Hlali and H. Zairi, « Reconfigurable Filter Based on Two-dimensional Materials », *in 2021 4th International Symposium on Advanced Electrical and Communication Technologies (ISAECT)*, Alkhobar, Saudi Arabia: IEEE, Dec. 2021, pp. 1–4, ISBN: 978-1-66543-773-8. DOI: 10.1109/ISAECT53699.2021.9668338.

[9] M. Aldrigo, M. Dragoman, S. Iordanescu, *et al.*, « Tunable and Miniaturized Microwave Filters Using Carbon Nanotube-Based Variable Capacitors », *IEEE Transactions on Nanotechnology*, vol. 21, pp. 118–130, 2022, ISSN: 1941-0085. DOI: 10.1109/TNANO.2022.3153561.

[10] H.-S. Tae, K.-S. Oh, H.-L. Lee, W.-I. Son, and J.-W. Yu, « Reconfigurable 1 $\times$ 4 Power Divider With Switched Impedance Matching Circuits », *IEEE Microwave and Wireless Components Letters*, vol. 22, *2*, pp. 64–66, Feb. 2012, ISSN: 1531-1309, 1558-1764. DOI: 10.1109/LMWC.2011.2181830.

[11] B. Wu, Z. Sun, X. Wang, Z. Ma, and C.-P. Chen, « A Reconfigurable Wilkinson Power Divider With Flexible Tuning Range Configuration », *IEEE Transactions on Circuits and Systems II: Express Briefs*, vol. 67, *7*, pp. 1219–1223, Jul. 2020, ISSN: 1549-7747, 1558-3791. DOI: 10.1109/TCSII.2019.2935261.

[12] J. Kim, J.-R. Yang, and J. Oh, « Reconfigurable hybrid matrix-based power divider with variable power-dividing ratios and frequencies », *Electronics Letters*, vol. 56, *17*, pp. 889–891, Aug. 2020, ISSN: 0013-5194, 1350-911X. DOI: 10.1049/el.2020.1277.

[13] A. Alazemi, M. Kourah, and A. Al-Zayed, « A reconfigurable five-port power divider with power routing versatility », *AEU - International Journal of Electronics and Communications*, vol. 110, p. 152 832, Oct. 2019, ISSN: 14348411. DOI: 10.1016/j.aeue.2019.152832.

[14] Y.-T. Chang, K.-Y. Lin, and T.-L. Wu, « Wideband Reconfigurable Power Divider/Combiner in 40-nm CMOS for 5G mmW Beamforming System », *IEEE Transactions on Microwave Theory and Techniques*, vol. 70, *2*, pp. 1410–1422, Feb. 2022, ISSN: 0018-9480, 1557-9670. DOI: 10.1109/TMTT.2021.3135296.

[15] F. D. Wappi, B. Mnasri, A. Ghayekhloo, L. Talbi, and H. Boutayeb, « Miniaturized Compact Reconfigurable Half-Mode SIW Phase Shifter with PIN Diodes », *Technologies*, vol. 11, *3*, p. 63, Apr. 2023, ISSN: 2227-7080. DOI: 10.3390/technologies11030063.

[16] X. Ding, Y. Xue, W. Liu, *et al.*, « Design of broadband reconfigurable phase shifters », *International Journal of RF and Microwave Computer-Aided Engineering*, vol. 32, *12*, Dec. 2022, ISSN: 1096-4290, 1099-047X. DOI: 10.1002/mmce.23424.

[17] T. Lambard, O. Lafond, M. Himdi, H. Jeuland, and S. Bolioli, « A novel analog 360° phase shifter design in Ku and Ka bands », *Microwave and Optical Technology Letters*, vol. 52, *8*, pp. 1733–1736, Aug. 2010, ISSN: 08952477. DOI: 10.1002/mop.25307.

[18] T. Lambard, O. Lafond, M. Himdi, H. Jeuland, S. Bolioli, and L. Le Coq, « Ka-Band Phased Array Antenna for High-Data-Rate SATCOM », *IEEE Antennas and Wireless Propagation Letters*, vol. 11, pp. 256–259, 2012, ISSN: 1548-5757. DOI: 10.1109/LAWP.2012.2189747.

[19] P. Padilla, A. Muñoz-Acevedo, and M. Sierra-Castañer, « Low loss 360° Ku band electronically reconfigurable phase shifter », *AEU - International Journal of Electronics and Communications*, vol. 64, *11*, pp. 1100–1104, Nov. 2010, ISSN: 14348411. DOI: 10.1016/j.aeue.2009.11.007.

[20] A. Qaroot and G. Mumcu, « Microfluidically Reconfigurable Reflection Phase Shifter », *IEEE Microwave and Wireless Components Letters*, vol. 28, *8*, pp. 684–686, Aug. 2018, ISSN: 1531-1309, 1558-1764. DOI: 10.1109/LMWC.2018.2847046.

[21] H. Xu, Y. Wang, F. A. Ghaffar, and L. Roy, « Reconfigurable Microwave Filters Implemented Using Field Programmable Microwave Substrate », *IEEE Transactions on Microwave Theory and Techniques*, vol. 69, *2*, pp. 1344–1354, Feb. 2021, ISSN: 1557-9670. DOI: 10.1109/TMTT.2020.3040384.

[22] A. Adane, F. Gallée, C. Person, V. Puyal, C. Villeneuve, and D. Dragomirescu, « Implementation of broadband microstrip-U coupled patch array on Si/BCB membrane for beamforming applications at 60 GHz », *in Proceedings of the 5th European Conference on Antennas and Propagation (EUCAP)*, Apr. 2011, pp. 1263–1267.

[23] Z. R. Omam, W. M. Abdel-Wahab, A. Raeesi, *et al.*, « Ka-Band Passive Phased-Array Antenna With Substrate Integrated Waveguide Tunable Phase Shifter », *IEEE Transactions on Antennas and Propagation*, vol. 68, *8*, pp. 6039–6048, Aug. 2020, ISSN: 1558-2221. DOI: 10.1109/TAP.2020.2983838.

[24] Q. Zhang, W. Jiang, P. Liu, K. Wei, W. Hu, and S. Gong, « Metamaterial-based linear phased array antenna with improved wide-angle scanning bandwidth by parasitic metal strips », *IET Microwaves, Antennas & Propagation*, vol. 15, *13*, pp. 1699–1709, 2021, ISSN: 1751-8733. DOI: 10.1049/mia2.12187.

[25] Y. Aouial, S. Meric, O. Lafond, and M. Himdi, « Synthesis of Sparse Planar Arrays for Passive Imaging Systems Based on Switch Submatrix », *IEEE Geoscience and Remote Sensing Letters*, vol. 9, *6*, pp. 1007–1011, Nov. 2012, ISSN: 1558-0571. DOI: 10.1109/LGRS.2012.2188493.

[26] C.-J. Chen and T.-H. Chu, « Design of a 60-GHz Substrate Integrated Waveguide Butler Matrix—A Systematic Approach », *IEEE Transactions on Microwave Theory and Techniques*, vol. 58, *7*, pp. 1724–1733, Jul. 2010, ISSN: 1557-9670. DOI: 10.1109/TMTT.2010.2050097.

[27] N. Tiwari and T. R. Rao, « A switched beam antenna array with butler matrix network using substrate integrated waveguide technology for 60GHz wireless communications », *AEU - International Journal of Electronics and Communications*, vol. 70, *6*, pp. 850–856, Jun. 2016, ISSN: 1434-8411. DOI: 10.1016/j.aeue.2016.03.014.

[28] G. Tian, J.-P. Yang, and W. Wu, « A Novel Compact Butler Matrix Without Phase Shifter », *IEEE Microwave and Wireless Components Letters*, vol. 24, *5*, pp. 306–308, May 2014, ISSN: 1558-1764. DOI: 10.1109/LMWC.2014.2306898.

[29] Q. Yang, S. Gao, Q. Luo, *et al.*, « A Low Complexity $16\times16$ Butler Matrix Design Using Eight-Port Hybrids », *IEEE Access*, vol. 7, pp. 177 864–177 873, 2019, ISSN: 2169-3536. DOI: 10.1109/ACCESS.2019.2958739.

[30] W. Rotman and R. Turner, « Wide-angle microwave lens for line source applications », *IEEE Transactions on Antennas and Propagation*, vol. 11, *6*, pp. 623–632, Nov. 1963, ISSN: 1558-2221. DOI: 10.1109/TAP.1963.1138114.

[31] K. Tekkouk, M. Ettorre, and R. Sauleau, « SIW Rotman Lens Antenna With Ridged Delay Lines and Reduced Footprint », *IEEE Transactions on Microwave Theory and Techniques*, vol. 66, *6*, pp. 3136–3144, Jun. 2018, ISSN: 1557-9670. DOI: 10.1109/TMTT.2018.2825374.

[32] E. Tolin, O. Litschke, S. Bruni, and F. Vipiana, « Compact Extended Scan Range Antenna Array Based on Rotman Lens », *IEEE Transactions on Antennas and*

*Propagation*, vol. 67, *12*, pp. 7356–7367, Dec. 2019, ISSN: 1558-2221. DOI: 10.1109/TAP.2019.2935086.

[33] J. Zhu, Y. Yang, S. Liao, and Q. Xue, « Dual-Band Antenna Hybridizing Folded Transmitarray and Folded Reflectarray », *IEEE Transactions on Antennas and Propagation*, vol. 70, *4*, pp. 3070–3075, Apr. 2022, ISSN: 1558-2221. DOI: 10.1109/TAP.2021.3137165.

[34] W. Li, Y. Wang, S. Sun, and X. Shi, « An FSS-Backed Reflection/Transmission Reconfigurable Array Antenna », *IEEE Access*, vol. 8, pp. 23 904–23 911, 2020, ISSN: 2169-3536. DOI: 10.1109/ACCESS.2020.2970611.

[35] T. Cai, G.-M. Wang, X.-L. Fu, J.-G. Liang, and Y.-Q. Zhuang, « High-Efficiency Metasurface With Polarization-Dependent Transmission and Reflection Properties for Both Reflectarray and Transmitarray », *IEEE Transactions on Antennas and Propagation*, vol. 66, *6*, pp. 3219–3224, Jun. 2018, ISSN: 1558-2221. DOI: 10.1109/TAP.2018.2817285.

[36] H. Zhang, X. Chen, Z. Wang, Y. Ge, and J. Pu, « A 1-Bit Electronically Reconfigurable Reflectarray Antenna in X Band », *IEEE Access*, vol. 7, pp. 66 567–66 575, 2019, ISSN: 2169-3536. DOI: 10.1109/ACCESS.2019.2918231.

[37] H. Yang, F. Yang, S. Xu, *et al.*, « A Study of Phase Quantization Effects for Reconfigurable Reflectarray Antennas », *IEEE Antennas and Wireless Propagation Letters*, vol. 16, pp. 302–305, 2017, ISSN: 1548-5757. DOI: 10.1109/LAWP.2016.2574118.

[38] H. Yang, F. Yang, X. Cao, *et al.*, « A 1600-Element Dual-Frequency Electronically Reconfigurable Reflectarray at X/Ku-Band », *IEEE Transactions on Antennas and Propagation*, vol. 65, *6*, pp. 3024–3032, Jun. 2017, ISSN: 1558-2221. DOI: 10.1109/TAP.2017.2694703.

[39] H. Li, X. Qi, T. Zhou, and T. A. Denidni, « Wideband Reconfigurable Reflectarray Based on Reflector-Backed Second-Order Bandpass Frequency Selective Surface », *IEEE Transactions on Antennas and Propagation*, vol. 70, *12*, pp. 12 334–12 339, Dec. 2022, ISSN: 1558-2221. DOI: 10.1109/TAP.2022.3209684.

[40] W. Menzel, « A New Travelling Wave Antenna in Microstrip », *in 1978 8th European Microwave Conference*, Sep. 1978, pp. 302–306. DOI: 10.1109/EUMA.1978.332503.

[41] D. R. Jackson, C. Caloz, and T. Itoh, « Leaky-Wave Antennas », *Proceedings of the IEEE*, vol. 100, *7*, pp. 2194–2206, Jul. 2012, ISSN: 1558-2256. DOI: 10.1109/JPROC.2012.2187410.

[42] D. R. Jackson and A. A. Oliner, « Leaky-Wave Antennas », *in Modern Antenna Handbook*, John Wiley & Sons, Ltd, 2008, ch. 7, pp. 325–367, ISBN: 978-0-470-29415-4. DOI: 10.1002/9780470294154.ch7.

[43] K. Wu, D. Deslandes, and Y. Cassivi, « The substrate integrated circuits - a new concept for high-frequency electronics and optoelectronics », *in 6th International Conference on Telecommunications in Modern Satellite, Cable and Broadcasting Service, 2003. TELSIKS 2003.*, vol. 1, Oct. 2003, P–III. DOI: 10.1109/âĎąSKS.2003.1246173.

[44] J. Liu, D. R. Jackson, and Y. Long, « Substrate Integrated Waveguide (SIW) Leaky-Wave Antenna With Transverse Slots », *IEEE Transactions on Antennas and Propagation*, vol. 60, *1*, pp. 20–29, Jan. 2012, ISSN: 1558-2221. DOI: 10.1109/TAP.2011.2167910.

[45] J. Xu, W. Hong, H. Tang, Z. Kuai, and K. Wu, « Half-Mode Substrate Integrated Waveguide (HMSIW) Leaky-Wave Antenna for Millimeter-Wave Applications », *IEEE Antennas and Wireless Propagation Letters*, vol. 7, pp. 85–88, 2008, ISSN: 1548-5757. DOI: 10.1109/LAWP.2008.919353.

[46] D. K. Karmokar, K. P. Esselle, and T. S. Bird, « An Array of Half-Width Microstrip Leaky-Wave Antennas Radiating on Boresight », *IEEE Antennas and Wireless Propagation Letters*, vol. 14, pp. 112–114, 2015, ISSN: 1548-5757. DOI: 10.1109/LAWP.2014.2356234.

[47] M. Archbold, E. J. Rothwell, L. C. Kempel, and S. W. Schneider, « Beam Steering of a Half-Width Microstrip Leaky-Wave Antenna Using Edge Loading », *IEEE Antennas and Wireless Propagation Letters*, vol. 9, pp. 203–206, 2010, ISSN: 1536-1225. DOI: 10.1109/LAWP.2010.2045730.

[48] D. K. Karmokar, K. P. Esselle, and S. G. Hay, « Fixed-Frequency Beam Steering of Microstrip Leaky-Wave Antennas Using Binary Switches », *IEEE Transactions on Antennas and Propagation*, vol. 64, *6*, pp. 2146–2154, Jun. 2016, ISSN: 0018-926X. DOI: 10.1109/TAP.2016.2546949.

[49] M. K. Mohsen, M. S. M. Isa, A. A. M. Isa, M. K. Abdulhameed, and M. L. Attiah, « Achieving Fixed-Frequency Beam Scanning With a Microstrip Leaky-Wave Antenna Using Double-Gap Capacitor Technique », *IEEE Antennas and Wireless Propagation Letters*, vol. 18, *7*, pp. 1502–1506, Jul. 2019, ISSN: 1548-5757. DOI: 10.1109/LAWP.2019.2920940.

[50] Y. Geng, J. Wang, Y. Li, Z. Li, M. Chen, and Z. Zhang, « Radiation Pattern-Reconfigurable Leaky-Wave Antenna for Fixed-Frequency Beam Steering Based on Substrate-Integrated Waveguide », *IEEE Antennas and Wireless Propagation Letters*, vol. 18, *2*, pp. 387–391, Feb. 2019, ISSN: 1548-5757. DOI: 10.1109/LAWP.2019.2892057.

[51] R. K. Luneburg, *Mathematical Theory of Optics*. University of California Press, 1966.

[52] H.-T. Chou and Z.-D. Yan, « Parallel-Plate Luneburg Lens Antenna for Broadband Multibeam Radiation at Millimeter-Wave Frequencies With Design Optimization », *IEEE Transactions on Antennas and Propagation*, vol. 66, *11*, pp. 5794–5804, Nov. 2018, ISSN: 1558-2221. DOI: 10.1109/TAP.2018.2867060.

[53] B. Fuchs, O. Lafond, S. Palud, *et al.*, « Comparative Design and Analysis of Luneburg and Half Maxwell Fish-Eye Lens Antennas », *IEEE Transactions on Antennas and Propagation*, vol. 56, *9*, pp. 3058–3062, Sep. 2008, ISSN: 1558-2221. DOI: 10.1109/TAP.2008.928818.

[54] A. Mikaelian and A. Prokhorov, « V Self-Focusing Media With Variable Index Of Refraction », *in Progress in Optics*, vol. 17, Elsevier, 1980, pp. 279–345, ISBN: 978-0-444-85309-7. DOI: 10.1016/S0079-6638(08)70241-5.

[55] A. Jouade, M. Himdi, and O. Lafond, « Fresnel Lens at Millimeter-Wave: Enhancement of Efficiency and Radiation Frequency Bandwidth », *IEEE Transactions on Antennas and Propagation*, vol. 65, *11*, pp. 5776–5786, Nov. 2017, ISSN: 1558-2221. DOI: 10.1109/TAP.2017.2755120.

[56] B. Fuchs, L. L. Coq, O. Lafond, S. Rondineau, and M. Himdi, « Design Optimization of Multishell Luneburg Lenses », *IEEE Transactions on Antennas and Propagation*, vol. 55, *2*, pp. 283–289, Feb. 2007, ISSN: 1558-2221. DOI: 10.1109/TAP.2006.889849.

[57] K. Sato and H. Ujiie, « A plate Luneberg lens with the permittivity distribution controlled by hole density », *Electronics and Communications in Japan (Part I: Communications)*, vol. 85, *9*, pp. 1–12, 2002, ISSN: 1520-6424. DOI: 10.1002/ecja.1120.

[58] Y. Li, L. Ge, M. Chen, Z. Zhang, Z. Li, and J. Wang, « Multibeam 3-D-Printed Luneburg Lens Fed by Magnetoelectric Dipole Antennas for Millimeter-Wave MIMO Applications », *IEEE Transactions on Antennas and Propagation*, vol. 67, *5*, pp. 2923–2933, May 2019, ISSN: 1558-2221. DOI: 10.1109/TAP.2019.2899013.

[59] J.-M. Poyanco, F. Pizarro, and E. Rajo-Iglesias, « Cost-effective wideband dielectric planar lens antenna for millimeter wave applications », *Scientific Reports*, vol. 12, *1*, p. 4204, Mar. 2022, ISSN: 2045-2322. DOI: 10.1038/s41598-022-07911-z.

[60] T. Ao, Y. Pan, and Y. Dong, « Low-Profile Dual-Polarized Luneburg Lens Based on TE/TM Surface Wave Modes », *IEEE Antennas and Wireless Propagation Letters*, vol. 21, *9*, pp. 1862–1866, Sep. 2022, ISSN: 1548-5757. DOI: 10.1109/LAWP.2022.3183219.

[61] J. Bor, O. Lafond, H. Merlet, P. Le Bars, and M. Himdi, « Technological Process to Control the Foam Dielectric Constant Application to Microwave Components and Antennas », *IEEE Transactions on Components, Packaging and Manufacturing Technology. Part A, Manufacturing Technology*, vol. 99, in press, Jan. 2014. DOI: 10.1109/TCPMT.2013.2294871.

[62] J. Bor, O. Lafond, H. Merlet, P. Le Bars, and M. Himdi, « FOAM BASED LUNEBURG LENS ANTENNA AT 60 GHZ », *Progress In Electromagnetics Research Letters*, vol. 44, pp. 1–7, 2014, ISSN: 1937-6480. DOI: 10.2528/PIERL13092405.

[63] O. Quevedo-Teruel, J. Miao, M. Mattsson, A. Algaba-Brazalez, M. Johansson, and L. Manholm, « Glide-Symmetric Fully Metallic Luneburg Lens for 5G Communications at Ka-Band », *IEEE Antennas and Wireless Propagation Letters*, vol. 17, *9*, pp. 1588–1592, Sep. 2018, ISSN: 1548-5757. DOI: 10.1109/LAWP.2018.2856371.

[64] B. Fuchs, O. Lafond, S. Rondineau, M. Himdi, and L. L. Coq, « Off-Axis Performances of Half Maxwell Fish-Eye Lens Antennas at 77 GHz », *IEEE Transactions on Antennas and Propagation*, vol. 55, *2*, pp. 479–482, Feb. 2007, ISSN: 1558-2221. DOI: 10.1109/TAP.2006.886576.

[65] M. Imbert, J. Romeu, M. Baquero-Escudero, M.-T. Martinez-Ingles, J.-M. Molina-Garcia-Pardo, and L. Jofre, « Assessment of LTCC-Based Dielectric Flat Lens Antennas and Switched-Beam Arrays for Future 5G Millimeter-Wave Communication Systems », *IEEE Transactions on Antennas and Propagation*, vol. 65, *12*, pp. 6453–6473, Dec. 2017, ISSN: 1558-2221. DOI: 10.1109/TAP.2017.2767821.

[66] J. G. Marin and J. Hesselbarth, « Lens Antenna With Planar Focal Surface for Wide-Angle Beam-Steering Application », *IEEE Transactions on Antennas and Propagation*, vol. 67, *4*, pp. 2757–2762, Apr. 2019, ISSN: 1558-2221. DOI: 10.1109/TAP.2019.2894336.

[67] O. Lafond, M. Himdi, H. Merlet, and P. Lebars, « An Active Reconfigurable Antenna at 60 GHz Based on Plate Inhomogeneous Lens and Feeders », *IEEE Transactions on Antennas and Propagation*, vol. 61, *4*, pp. 1672–1678, Apr. 2013, ISSN: 1558-2221. DOI: 10.1109/TAP.2012.2237003.

[68] Q. Xi, C. Ma, H. Li, B. Zhang, C. Li, and L. Ran, « A Reconfigurable Planar Fresnel Lens for Millimeter-Wave 5G Frontends », *IEEE Transactions on Microwave Theory and Techniques*, vol. 68, *11*, pp. 4579–4588, Nov. 2020, ISSN: 1557-9670. DOI: 10.1109/TMTT.2020.3025337.

[69] D. M. Pozar, *Microwave Engineering, 4th Edition*. Wiley, Nov. 2011, ISBN: 978-1-118-21363-6.

[70] L. F. Chen, C. K. Ong, C. P. Neo, V. V. Varadan, and V. K. Varadan, *Microwave Electronics: Measurement and Materials Characterization*. John Wiley & Sons, Nov. 2004, ISBN: 978-0-470-02045-6.

[71] T. Lambard, O. Lafond, M. Himdi, H. Jeuland, and S. Bolioli, « Low loss reflection-type phase shifter in Ku band », *Microwave and Optical Technology Letters*, vol. 52, *2*, pp. 283–285, 2010, ISSN: 1098-2760. DOI: 10.1002/mop.24944.

[72] Z. Kordiboroujeni and J. Bornemann, « New Wideband Transition From Microstrip Line to Substrate Integrated Waveguide », *IEEE Transactions on Microwave Theory and Techniques*, vol. 62, *12*, pp. 2983–2989, Dec. 2014, ISSN: 1557-9670. DOI: 10.1109/TMTT.2014.2365794.

[73] W. Hong, B. Liu, Y. Wang, *et al.*, « Half Mode Substrate Integrated Waveguide: A New Guided Wave Structure for Microwave and Millimeter Wave Application », *in 2006 Joint 31st International Conference on Infrared Millimeter Waves and 14th*

*International Conference on Teraherz Electronics*, Sep. 2006, pp. 219–219. DOI: 10.1109/ICIMW.2006.368427.

[74] W. Shao and Q. Chen, « Performance analysis of an all-dielectric planar Mikaelian lens antenna for 1-D beam-steering application », *Optics Express*, vol. 29, *18*, pp. 29 202–29 214, Aug. 2021, ISSN: 1094-4087. DOI: 10.1364/OE.438182.

[75] J. Bor, B. Fuchs, O. Lafond, and M. Himdi, « Flat foam-based Mikaelian lens antenna for millimeter wave applications », *in 2014 44th European Microwave Conference*, Oct. 2014, pp. 1640–1643. DOI: 10.1109/EuMC.2014.6986768.

[76] J. Bor, O. Lafond, M. Himdi, H. Merlet, and P. Lebars, « Smooth plate Luneburg lens with superstrate », *in 2015 9th European Conference on Antennas and Propagation (EuCAP)*, Apr. 2015, pp. 1–4.

COLLEGE DOCTORAL BRETAGNE
MATHS, TELECOMS
INFORMATIQUE, SIGNAL
SYSTEMES, ELECTRONIQUE

Université de Rennes

**Titre :** Antennes et circuits reconfigurables à base de matériaux artificiels contrôlables

**Mot clés :** Antennes, circuits, reconfigurable, matériaux artificiels

**Résumé :** Les systèmes modernes de communication sans fil nécessitent des composants haute fréquence qui peuvent être reconfigurés dynamiquement afin de modifier leurs performances. En général, un dispositif reconfigurable est associé à une fonction unique, qui peut être modifiée ou contrôlée. Ce doctorat commence par une technologie, le "Field Programmable Microwave Substrate (FPMS)". Le FPMS est constitué de cellules unitaires qui peuvent être reconfigurées individuellement afin de contrôler localement la constante diélectrique du matériau, elle peut varier d'une valeur positive à une valeur négative. La programmation de matériaux positifs pris en sandwich entre deux matériaux négatifs permet de créer un guide d'ondes artificiel. Les travaux présentés dans cette thèse concernent l'amélioration de la technologie FPMS. Une nouvelle carte FPMS est proposée permettant d'augmenter la fréquence de travail de 1-3GHz à 10-15GHz. Des antennes reconfigurables sont également conçues à l'aide de la technologie FPMS. Dans la bande X, une antenne à ondes de fuite est proposée, dont la direction du faisceau principal peut être contrôlée, à une fréquence fixe, grâce à l'utilisation de la technologie FPMS. Le concept FPMS a été poussé jusqu'à 25-30GHz, afin de développer des antennes lentilles inhomogènes reconfigurables, l'idée est d'utiliser la capacité de la technologie FPMS à contrôler localement la constante diélectrique afin de synthétiser la loi d'indice de la lentille.

**Title:** Reconfigurable antennas and circuits based on controllable artificial materials

**Keywords:** Antennas, circuits, reconfigurable, artificial materials

**Abstract:** Modern wireless communication systems require high-frequency components that can be reconfigured dynamically to modify their performance. Usually, a reconfigurable device has a single function associated with it, but this function can be altered or controlled. This Ph.D. starts with one technology, the "Field Programmable Microwave Substrate (FPMS)." The FPMS consists of small unit cells that can be individually reconfigured to a range of positive or negative dielectric constants. Programming positive materials sandwiched between two negative materials results in a slab waveguide that behaves like a substrate-integrated waveguide. The work presented in this thesis concern the improvement of the FPMS technology: loss reduction, increasing the working frequency, and bandwidth. A new FPMS board is proposed allowing to increase the working from 1-3GHz to 10-15GHz. Using the FPMS technology, reconfigurable antennas are also designed. In the X-Band, a leaky wave antenna is proposed; thanks to the use of FPMS technology, electronic beam steering is achieved at a fixed frequency. The FPMS concept has been pushed up to 25-30GHz, to develop reconfigurable inhomogeneous lens antennas; the idea is to use the local dielectric constant reconfigurability offered by the FPMS technology to synthesize the index law of the lens.